THESE de DOCTORAT DE L'UNIVERSITE DE LYON
opérée au sein de
L'Institut National des Sciences Appliquées de Lyon

Ecole Doctorale N° EDA160
ELECTRONIQUE, ELECTROTECHNIQUE, AUTOMATIQUE (EEA)

Spécialité de doctorat : **Traitement du Signal et de l'Image**

Soutenue publiquement le 16/12/2016, par :
(Miaomiao ZHANG)

Fourier-based reconstruction of ultrafast sectorial images in ultrasound

Devant le jury composé de :

LOVSTAKKEN Lasse, Professeur des Universités, NTNU	Rapporteur
PERNOT Mathieu, Directeur de Recherche, Institut Langevin	Rapporteur
D'HOOGE Jan, Professeur des Universités, KU LEUVEN	Examinateur
BRIDAL S.Lori, Directeur de Recherche, Université Paris 06	Examinatrice
FRIBOULET Denis, Professeur des Universités, INSA-LYON	Directeur de thèse
BERNARD Olivier, Maître de Conférences, INSA-LYON	Co-directeur de thèse

Département FEDORA – INSA Lyon - Ecoles Doctorales – Quinquennal 2016-2020

SIGLE	ECOLE DOCTORALE	NOM ET COORDONNEES DU RESPONSABLE
CHIMIE	**CHIMIE DE LYON** **http://www.edchimie-lyon.fr** Sec : Renée EL MELHEM Bat Blaise Pascal 3e etage secretariat@edchimie-lyon.fr Insa : R. GOURDON	M. Stéphane DANIELE Institut de Recherches sur la Catalyse et l'Environnement de Lyon IRCELYON-UMR 5256 Équipe CDFA 2 avenue Albert Einstein 69626 Villeurbanne cedex directeur@edchimie-lyon.fr
E.E.A.	**ELECTRONIQUE, ELECTROTECHNIQUE, AUTOMATIQUE** **http://edeea.ec-lyon.fr** Sec : M.C. HAVGOUDOUKIAN Ecole-Doctorale.eea@ec-lyon.fr	M. Gérard SCORLETTI Ecole Centrale de Lyon 36 avenue Guy de Collongue 69134 ECULLY Tél : 04.72.18 60.97 Fax : 04 78 43 37 17 Gerard.scorletti@ec-lyon.fr
E2M2	**EVOLUTION, ECOSYSTEME, MICROBIOLOGIE, MODELISATION** **http://e2m2.universite-lyon.fr** Sec : Sylvie ROBERJOT Bât Atrium - UCB Lyon 1 04.72.44.83.62 Insa : H. CHARLES secretariat.e2m2@univ-lyon1.fr	M. Fabrice CORDEY CNRS UMR 5276 Lab. de géologie de Lyon Université Claude Bernard Lyon 1 Bât Géode 2 rue Raphaël Dubois 69622 VILLEURBANNE Cédex Tél : 06.07.53.89.13 cordey@ univ-lyon1.fr
EDISS	**INTERDISCIPLINAIRE SCIENCES-SANTE** **http://www.ediss-lyon.fr** Sec : Sylvie ROBERJOT Bât Atrium - UCB Lyon 1 04.72.44.83.62 Insa : M. LAGARDE secretariat.ediss@univ-lyon1.fr	Mme Emmanuelle CANET-SOULAS INSERM U1060, CarMeN lab, Univ. Lyon 1 Bâtiment IMBL 11 avenue Jean Capelle INSA de Lyon 696621 Villeurbanne Tél : 04.72.68.49.09 Fax :04 72 68 49 16 Emmanuelle.canet@univ-lyon1.fr
INFOMATHS	**INFORMATIQUE ET MATHEMATIQUES** **http://infomaths.univ-lyon1.fr** Sec :Renée EL MELHEM Bat Blaise Pascal 3e etage infomaths@univ-lyon1.fr	Mme Sylvie CALABRETTO LIRIS – INSA de Lyon Bat Blaise Pascal 7 avenue Jean Capelle 69622 VILLEURBANNE Cedex Tél : 04.72. 43. 80. 46 Fax 04 72 43 16 87 Sylvie.calabretto@insa-lyon.fr
Matériaux	**MATERIAUX DE LYON** **http://ed34.universite-lyon.fr** Sec : M. LABOUNE PM : 71.70 –Fax : 87.12 Bat. Direction Ed.materiaux@insa-lyon.fr	M. Jean-Yves BUFFIERE INSA de Lyon MATEIS Bâtiment Saint Exupéry 7 avenue Jean Capelle 69621 VILLEURBANNE Cedex Tél : 04.72.43 71.70 Fax 04 72 43 85 28 jean-yves.buffiere@insa-lyon.fr
MEGA	**MECANIQUE, ENERGETIQUE, GENIE CIVIL, ACOUSTIQUE** **http://mega.universite-lyon.fr** Sec : M. LABOUNE PM : 71.70 –Fax : 87.12 Bat. Direction mega@insa-lyon.fr	M. Philippe BOISSE INSA de Lyon Laboratoire LAMCOS Bâtiment Jacquard 25 bis avenue Jean Capelle 69621 VILLEURBANNE Cedex Tél : 04.72 .43.71.70 Fax : 04 72 43 72 37 Philippe.boisse@insa-lyon.fr
ScSo	**ScSo*** **http://recherche.univ-lyon2.fr/scso/** Sec : Viviane POLSINELLI Brigitte DUBOIS Insa : J.Y. TOUSSAINT Tél : 04 78 69 72 76 viviane.polsinelli@univ-lyon2.fr	M. Christian MONTES Université Lyon 2 86 rue Pasteur 69365 LYON Cedex 07 Christian.montes@univ-lyon2.fr

*ScSo : Histoire, Géographie, Aménagement, Urbanisme, Archéologie, Science politique, Sociologie, Anthropologie

Abstract

Echocardiography is one of the most widely used modality in real time heart imaging thanks to its noninvasive nature and low cost. By providing dense image volumes in real time, three-dimensional echocardiography can improve the accuracy of the echocardiographic evaluation of cardiac chamber volumes and be used to assess cardiovascular function and anatomy in various clinical settings. However, the real-time property of three-dimensional echocardiography is still limited in terms of frame rate due to the limited speed of sound. To increase the frame rate, plane wave and diverging wave in transmission have been proposed to drastically reduce the number of transmissions to reconstruct one image. In this thesis, starting with the 2D plane wave imaging methods, the reconstruction of 2D/3D echocardiographic sequences in Fourier domain using diverging waves is addressed. The main contributions are described below.

The first contribution of this thesis is to study the influence of the transmission scheme in the context of 2D plane wave imaging. Based on an analytical study, the influence of the transmitted angle sequences and the number of plane waves on the compounded image quality is investigated. A dichotomous transmission scheme is proposed. The efficiency of the different transmission schemes is assessed by evaluating the quality of images reconstructed from the current state-of-the-art plane wave imaging methods. Numerical and experimental results show that the proposed transmission scheme significantly improves the quality of the reconstructed B-mode images at a constant frame rate.

The second contribution concerns the development of an alternative Fourier-based plane wave imaging method (*i.e.* Ultrasound Fourier Slice Beamforming) by using the concept of steered plane waves both in transmission and in reception. We build a theoretical model to describe the relationship between the echoes and object function based on the Fourier slice theorem. The proposed method is assessed using numerical simulations and experiments, including *in vitro* and *in vivo* experiments. Results revealed that the proposed method produces very competitive image quality compared to the state-of-the-art Fourier-based and spatial-based methods.

The third contribution concerns the extension of Fourier-based imaging methods from linear to sectorial imaging in 2D by studying the difference between plane wave and diverging wave transmission in terms of travel time for a given scatterer in the medium and a given transducer element. We derive an explicit spatial transformation which allows deforming the referential Cartesian space insonified by a diverging wave into a dedicated one where the modified medium can be considered as being excited by a plane wave. The performance of the derived approach is evaluated in terms of resolution and contrast from both simulations and *in vitro* experiments. Comparisons with the current state-of-the-art method illustrate the potential of the derived methods in producing competitive results with lower computational complexity when compared to the conventional delay and sum (DAS) technique.

Finally, the 2D Fourier-based diverging wave imaging methods are extended to 3D by deriving the equivalence between 3D diverging wave and plane wave. Numerical simulations are performed to validate and evaluate the proposed method. Results show that the proposed approach provides competitive scores in terms of image quality compared to the DAS technique, but with a much lower computational complexity.

Résumé

L'échocardiographie est une modalité d'imagerie sûre, non-invasive, qui est utilisée pour évaluer la fonction et l'anatomie cardiaque en routine clinique. En fournissant des images volumiques complètes en temps réel, l'échocardiographie en trois dimensions (3D) possède le potentiel afin d'améliorer la précision de l'évaluation des volumes des cavités cardiaques par rapport à l'imagerie 2D et fournit une vue réaliste des valves cardiaques et des anomalies congénitales. En imagerie échocardiographique 3D classique, l'acquisition d'un seul volume avec une qualité raisonnable exige des milliers de faisceaux pour imager le cœur avec suffisamment de détails, ce qui conduit à un fréquence d'imagerie de quelques Hz, ce qui se révèle insuffisant en pratique clinique quotidienne. Afin d'augmenter la fréquence d'image, l'utilisation d'ondes planes ou d'ondes divergentes en transmissinon a été proposée afin de réduire le nombre de tirs nécessaires à la reconstruction d'une image. L'objectif de cette thèse consiste à développer un procédé d'imagerie par ultrasons ultra-rapide en échocardiographie 2/3D basé sur une insonification par ondes divergentes et réalisant une reconstruction dans le domaine de Fourier. Le point de départ était une méthode classique d'imagerie 2D en ondes planes. Les contributions principales obtenues au cours de la thèse sont décrites ci-dessous.

La première contribution de cette thèse concerne l'étude de l'influence du régime de transmission sur la qualité d'image au travers de l'utilisation d'ondes planes en transmission. Nous avons présenté un schéma de transmission dichotomique pour l'acquisition linéaire en analysant mathématiquement la pression générée. Nous avons ensuite montré que ce système de transmission peut améliorer la qualité des images reconstruites pour une cadence constante en utilisant les algorithmes de reconstruction conventionnels. La qualité des images reconstruites a été évaluée en termes de résolution et de contraste au moyen de simulations et acquisitions expérimentales réalisées sur des fantômes.

La deuxième contribution concerne le développement d'une nouvelle méthode d'imagerie 2D en ondes plane opérant dans le domaine de Fourier et basée sur le théorème de la coupe centrale. Cet algorithme permet de reconstruire le spectre de l'objet à imager radialement dans le domaine de Fourier. La méthode proposée a été évaluée et comparée avec les méthodes pour ondes planes existantes au moyen des simulations, d'acquisitions expérimentales réalisées sur des fantômes et *in vivo*. Les résultats que nous avons obtenus montrent que l'approche proposée fournit des résultats très proches de ceux fournit par les méthodes classiques en termes de résolution latérale et contraste de l'image.

La troisième contribution concerne le développement d'une transformation spatiale explicite permettant d'étendre les méthodes 2D opérant dans le domaine de Fourier d'une acquisition en géométrie linéaire avec des ondes planes à la géométrie sectorielle avec des ondes divergente en transmission. Cette transformation a été obtenue en établissant un isomorphisme en termes de temps de vol lorsque soit une onde divergente soit une onde plane est utilisée en transmission. Les résultats que nous avons obtenus à partir de simulations et d'acquisitions expérimentales *in vivo* montrent que l'application de cette extension à la méthode de Lu permet d'obtenir la même qualité d'image que la méthode spatiale de Papadacci basée sur des ondes divergentes, mais avec une complexité de calcul plus faible.

Finalement, la formulation proposée en 2D pour les méthodes ultra-rapides opérant dans le domaine de Fourier ont été étendues en 3D. Cela a été réalisé en tenant compte de la coordonnée y dans l'équation du temps vol de l'onde plane et de l'onde divergente. En étudiant la pression obtenue lors de la sommation cohérente des ondes divergentes 3D, un schéma de transmission dichotomique a été proposé dans le but d'améliorer la

qualité d'image, et ce d'une manière suffisamment rapide pour être peu influencée par l'augmentation du nombre d'ondes divergentes. L'approche proposée donne des résultats compétitifs associés à une complexité de calcul beaucoup plus faible par rapport à la technique de retard et somme conventionnelle.

Acknowledgment

I would like to thank everyone who gave me their help and support during the past four years of my Master and Ph.D. study in France.

First and foremost, I would like to thank my supervisors Prof. Denis Friboulet, Dr. Olivier Bernard and Prof. Hervé Liebgott. Thanks for giving me this excellent opportunity to work on this exciting project. Your insightful and inspiring guidance, continuous support and encouragement are indispensable to the accomplishment of this thesis, which i cannot express in words. Denis, you are the most enthusiastic person I have ever met. Your patience, enthusiasm and kindness always inspire me to think positive and help me pass through the difficult time. Life seems more colorful with your big smile and laughter. Olivier, your patience and attention to details is unmatched. Thank you so much for all the support and hard work that you have done for me, especially in a time of need. It felt amazing to know that you always had my back. Hervé, your broad knowledge of ultrasound and insight into problems are indispensable to the success of this project. It is really a great experience working with you.

I specially express my thanks to Prof. Lasse Lovstakken and Dr. Mathieu Pernot for reviewing this manuscript and Prof. Jan D'hooge and Dr. S.Lori Bridal for accepting as the jury of my thesis.

I want to acknowledge Olivier Beuf, the director of the lab, for providing us an amazing working environment, surrounded by knowledge and fantastic colleagues. The lab has done and is doing so much amazing research, that i am very happy and proud to be part of it.

I would like to thank all my colleagues in the laboratory for their help during my stay in France. Especially, I want to thank Yuemin Zhu, who is responsible for the application program, for his help on all the administrative affairs during my application. I also want to thank François Varray and Lorena Petrusca for the experiment preparation and data acquisition. Emmanuel Roux, thanks for your help on many things during the past four years in France. It was a pleasure being classmates, colleagues and friends with you. Feng Yang, you gave me a lot of useful suggestions both for work and the life. My thanks also go to all the secretaries in the lab for helping me to do all the administrative affairs.

I thank Damien Garcia for providing me his code and *in vivo* cardiac data.

I would also show my gratitude to China Scholarship Council (CSC) for the financement during my Ph.D. study.

Last but not least, my sincere thanks go to my family for their unconditional love and support in everything I do. Thanks my parents and my parents-in-law for taking care of me and my daughter during this very hard time. No matter where i am and when i need, you are always there to support me. I also would like to express my deepest gratitude to my beloved husband Ge. Thank you for your love, your support and encouragement during our life. To my daughter, Yucheng, thanks for always making me feel like the happiest mom in the world.

Contents

x

I Introduction

Chapter 1

Introduction

In this chapter, the motivation of the dissertation work is introduced first. Then the research objectives of this work are outlined. Finally, the organization of the dissertation is presented.

1.1   Motivation

Three-dimensional echocardiography (3DE) is a safe, non-invasive imaging modality, which is used to assess cardiovascular function and anatomy in various clinical settings. This technique improves the accuracy of the echocardiographic evaluation of cardiac chamber volumes and gives a realistic view of cardiac valves and congenital abnormalities, which has been conceived as one of the most promising methods for the diagnosis of valvular heart disease [Lang *et al.* (2006),Monaghan (2006),Shiota (2014)]. However, the current limited frame rate represents a bottleneck for the use of 3DE in daily clinical practice. Indeed, in conventional ultrasound imaging, volumes are constructed by sequentially transmitting beams that are steered in different directions to cover a desired image sector. Assuming that the only limitation to the frame rate is the ultrasound wave propagation, the time needed to construct an image is thus proportional to the number of lines, the image depth and the speed of sound. For soft human tissue, the wave propagation speed is approximately 1540 m/s. With a depth of 200 mm, it takes about 260 μs for a single beam to propagate into the human body and come back. This allows for 3850 transmissions in one second. For cardiac imaging, acquiring a single volume with reasonable quality requires thousands of beams to picture the heart with sufficient details, thus leading to a frame rate around 1 volume per second (Figure 1.1a), which is not sufficient in practice. Therefore,

with conventional ultrasound imaging method, although it became readily apparent that 3DE is better suited than two-dimensional echocardiography (2DE) for the assessment of 3D dynamic phenomena, the limited speed of sound still prevents the acquisition of large fields of view at frame rates sufficient to assess the complex dynamics of a beating heart.

There are several ways to reach the trade-off between the frame rate and the image quality. One way is to use the technique referred to as parallel receive beamforming to generate several imaging beams in parallel by transmitting broader beams [Shattuck *et al.* (1984)], which can be achieved by reducing the transmit aperture [Von Ramm *et al.* (1991), Pavy (1993), Hergum *et al.* (2007)] and transmitting unfocused or defocused beams [von Ramm *et al.* (1984), Hasegawa and Kanai (2011)]. In this way, the frame rate can be increased with a factor equals to the number of parallel received beams (Figure 1.1b). However, when increasing the number of parallel received beams, the width of the transmitted beams must be increased accordingly, which results in a lower pressure when the wave propagates at larger imaging depth and, therefore it decreases the image quality (*i.e.* signal-to-noise ratio and contrast resolution). The image resolution is also degraded due to the increase of the transmitted beam width. In order to maintain high resolution while using fewer broad beams to illuminate the desired field of view, Synthetic Transmit Aperture (STA) imaging has been proposed [Jensen *et al.* (2006)a]. A single element is used to transmit a spherical wave covering the full image view and all of the elements are used in reception to form a low resolution image. By coherently combining the images from successive transmissions, one may produce transmit dynamic focusing along each line of the final image.

Another way to increase the frame rate is to use multiple transmit beams, called Multi-Line Transmission (MLT). With this technique, several focused ultrasound pulses steered in different lateral directions are transmitted and the same number of image lines are beamformed simultaneously [Shirasaka (1989), Mallart and Fink (1992)]. Using MLT, the frame rate can be M times faster, where M is the number of parallel pulses in each transmission. However, the interferences, also known as cross-talk between the simultaneous beams may create artifacts in the resulting image, for instance bright targets can appear in several locations in the image. Various methods have been proposed to reduce the cross-talks by separating the beams either spatially or spectrally [Dubberstein and Von Ramm (2000), Demi *et al.* (2012), Demi *et al.* (2015), Denarie *et al.* (2013)a], using beam transformation techniques [Drukarev *et al.* (1993)], using second harmonic signal [Prieur *et al.* (2013)] or various apodization schemes [Tong *et al.* (2013)a, Tong *et al.* (2014), Tong *et al.* (2013)b].

The third technique corresponds to the use of ECG gated stitching [Brekke *et al.* (2007)] to acquire sub-volumes from different cardiac cycles. This is possible because the cardiac activity is a cyclic process. With this method, the sub-volumes acquired from consecutive heartbeats are stitched together to form a full volume and thus it allows to increase the volume size while maintaining the frame rate (Figure 1.1c). Since the sub-volumes come from different heartbeat cycles, the ECG gated stitching is prone to motion

artifacts caused by transducer movement, respiration and varying heart rate [Rabben (2010)].

(a)   (b)   (c)
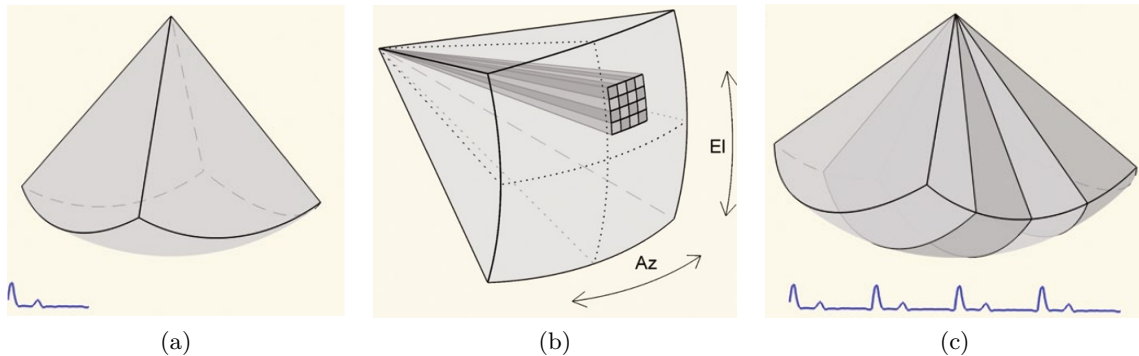
Figure 1.1: (Figure 2.1 and 2.3 in [Rabben (2010)]) (a) Real-time 3D imaging: a 60 by 60 degrees volume is acquired in real-time. (b) In 3D beamforming, the beams are steered in both azimuthal (Az) and elevation (El) directions by utilizing all elements of the 2D matrix array. In addition to electronic steering in 3D, current 3D systems are able to perform parallel receive beamforming where the system transmits one wide transmit beam and receives on multiple receive beams (in this case 16 receive beams). (c) ECG gated stitched 3D imaging: sub-volumes from four consecutive heartbeats are stitched together to a 80 by 80 degrees volume.

Several approaches are also proposed to perform high volume rate 3D ultrasound imaging [Perrin *et al.* (2012)b, Skaug *et al.* (2014)] by reducing the number of transmissions. However, the frame rate reached using the above-mentioned methods is still limited and not sufficient to perform motion and blood flow measurement on the entire volume. In order to significantly reduce the number of transmissions, the concept of ultrafast ultrasound imaging has been proposed. This approach uses a smaller number of defocused ultrasound waves in transmission to insonify the entire medium [Tanter and Fink (2014)]. Coherent compounding of the ultrasound image acquired from each transmission allows for a synthetic focusing in the full image, as in Synthetic Transmit Aperture imaging [Jensen *et al.* (2006)a]. Several approaches were proposed and validated in 2D based on this concept with plane waves (PW) [Lu (1997), Cheng and Lu (2006), Montaldo *et al.* (2009), Garcia *et al.* (2013)] and diverging waves (DW) insonifications [Hasegawa and Kanai (2011), Papadacci *et al.* (2014)] for different applications, such as transient elastography [Montaldo *et al.* (2009)] and cardiac imaging [Hasegawa and Kanai (2011), Papadacci *et al.* (2014)]. Very recently, Provost *et al.* demonstrated the feasibility of compounding DW using a sparse virtual array located behind the probe to achieve high frame rates for 3D cardiac imaging [Provost *et al.* (2014)]. These approaches use PW or DW to insonify the whole medium for each emission. The backscattered echoes are then measured and processed to reconstruct simultaneously all lines of the image of interest either in the Fourier domain [Lu (1997), Cheng and Lu (2006), Garcia *et al.* (2013)] or in the space domain [Montaldo *et al.* (2009), Hasegawa and Kanai (2011), Papadacci *et al.* (2014)]. It has been shown in [Garcia

et al. (2013)] that the computational complexity of the reconstruction process with PW insonifications performed in the space domain is higher than in the Fourier domain.

As far as cardiac imaging is concerned, all the existing ultrafast methods rely on a sectorial configuration associated to DW, due to the limited anatomical access to the heart. Moreover, it is worth to be noted that all the DW-based proposed methods [Hasegawa and Kanai (2011), Papadacci *et al.* (2014), Provost *et al.* (2014)] perform reconstruction in the spatial domain, resulting in a higher computational complexity. In order to reduce the computational load in high frame rate echocardiography, therefore, an interesting approach would be to develop a high frame rate imaging method based on Fourier domain with DW insonifications for cardiac imaging both in 2D and 3D.

1.2 Objectives

In the above-described context, the objective of this work is thus to develop a methodology allowing for 3D ultrafast echocardiographic imaging, based on DW insonification and Fourier domain reconstruction, as well as the careful evaluation of the proposed approach. Starting from 2D PW imaging, the present work proposes to progressively achieve that end by successively addressing the following methodological aspects:

- A new Fourier-based 2D PW imaging method based on the Fourier slice theorem. This algorithm allows the reconstruction of the object spectrum radially and provides an alternative of the current PW imaging techniques in Fourier domain.

- An extension of the 2D Fourier-based PW imaging methods for sectorial imaging with DW in transmission. We propose an explicit transformation by establishing an isomorphism in terms of travel time when either a DW or a PW is used in transmission. This formulation allows the reconstruction of wide angle images in Fourier domain with lower computational complexity compared to the current techniques.

- A 3D DW imaging method in Fourier domain. The proposed 2D formulation is extended to 3D. The derived method produces competitive results with much lower computational complexity when compared to conventional delay-and-sum technique.

1.3 Thesis organization

The dissertation is organized as follows:

In Chapter 1, the motivation and objectives of this work are introduced. The motivation behind this work is to develop an efficient 3D echocardiography imaging method to increase the frame rates with lower computational complexity. The research objectives of this work are also outlined.

In Chapter 2, the principle of echocardiography is reviewed, including the image formation process and the main ultrasound imaging modes used in practice.

In Chapter 3, the state-of-the-art ultrafast imaging methods based on PW and DW insonifications are first introduced. To acquire an image of comparable quality as the one obtained using conventional focusing, the principle of coherent compounding is then presented. Finally, the motion compensation methods for ultrafast imaging of moving targets are also presented.

In Chapter 4, the influence of the transmission scheme on image quality is investigated. Based on an analytical study of the synthetic pressure, we studied the efficiency of using dichotomous transmission scheme for linear acquisition which allows improving the quality of the reconstructed images at a constant frame rate. The efficiency of the dichotomous transmission scheme is assessed through the use of the current state-of-the-art reconstruction algorithms (introduced in Chapter3) for high frame rate imaging. The quality of the reconstructed images is evaluated in terms of resolution and contrast from both simulations and phantom experiments.

In Chapter 5, an alternative ultrafast PW imaging method (Ultrasound Fourier Slice Beamforming) is proposed based on the Fourier slice theorem, which allows to sample the object spectrum radially in the Fourier domain. With this method, steered PW transmissions are used with coherent compounding to improve the image quality (both resolution and contrast) at the expense of image frame rate, like in other previous PW imaging methods. The proposed method is evaluated and compared with the existing PW imaging methods by computer simulations as well as phantom and *in vivo* experiments.

In Chapter 6, we present the framework that we proposed to extend existing Fourier-based techniques (initially developed for PW imaging) to sectorial imaging using diverging beams in transmission. By studying the difference between PW and DW transmission in terms of travel time for a given scatterer in the medium and a given transducer element, we derived an explicit spatial transformation which allows deforming the referential Cartesian space insonified by a DW into a dedicated one where the modified medium can be considered as being excited by a PW. The corresponding extended methods are assessed by computer simulations and experiments, including phantom and *in vivo* experiments of the human heart.

In Chapter 7, the 2D Fourier-based ultrafast sectorial imaging methods are extended in 3D. By studying the synthetic pressure field of the 3D DW compounding, the virtual sources positions are determined to improve the image quality in a fast way. Finally, the extended 3D Fourier-based DW imaging methods are evaluated by numerical simulations and phantom experiments.

In Chapter 8, the whole work is summarized, and future studies are suggested.

Miaomiao ZHANG

II   Background

Chapter 2

Echocardiography

In this chapter, we first introduce the conventional ultrasound cardiac image formation process, *i.e.* the generation and reception of ultrasound waves, the wave propagation in the tissue and the conventional beamforming method. Then the different imaging modes of echocardiography are described.

2.1 Ultrasound image formation

Echocardiography is a diagnostic imaging modality used to visualize the interior of the human heart. It is based on transmitting focused ultrasound pulses from a transducer into the tissue, and then processing the backscattered echoes returning from structures within to form an image of the tissue. This part gives some details on the formation process of such image.

2.1.1 Transducers

Cardiac ultrasound images are usually acquired by using phased array transducers, which consist of a 1D array (or 2D matrix for 3D imaging) of piezoelectric elements that convert electric energy to acoustic pressure, and vice versa. Figure 2.1 shows the principle of the transducer element transmitting and receiving signals. When transmitting pulses, a voltage of the appropriate frequency is applied to the transducer elements, causing the piezoelectric structures to vibrate and generate ultrasound waves (Figure 2.1a). Upon receival, when the reflected portion of the ultrasound pulse reaches the transducer, the acoustical vibrations induce an electrical signal, which is referred to as the *echo* signal

(Figure 2.1b) and is used for image formation.

(a)   (b)
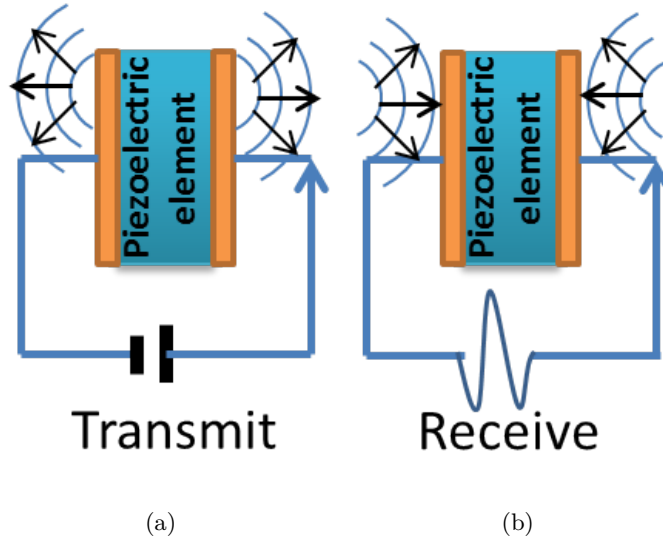
Figure 2.1: Principle of transducer element transmitting and receiving signals. (a) In transmission, the piezoelectric element vibrates to generate a sound wave when a voltage is applied. (b) In reception, the piezoelectric element generates a voltage when a vibration (an ultrasound wave) applied.

2.1.2 Wave propagation and interaction with tissue

The ultrasound waves used for medical diagnostic are mainly mechanical waves in a longitudinal direction with a frequency above 20 kHz that is not audible to a human ear. The wave is propagating through a continuous interchange between the kinetic energy and the potential energy of medium particles, which is related to the density and the elastic properties of the medium [Insana and Brown (1993), Angelsen (2000)]. Assuming that the transmitted ultrasound wave propagates in a homogeneous medium without attenuation, it follows the wave equation [Angelsen (2000), Schmerr Jr (2014)]:

$$\frac{\partial^2 p(\mathbf{x}, t)}{\partial t^2} = c^2 \nabla^2 p(\mathbf{x}, t) \tag{2.1}$$

where $p(\mathbf{x}, t)$ is the acoustic pressure at spatial position $\mathbf{x}$ on time t, c is the sound velocity, which depends on the density ρ and the compressibility κ of the tissue and can be expressed as:

$$c = \frac{1}{\sqrt{\rho \, \kappa}} \tag{2.2}$$

In echography, for soft human tissue, c is approximately 1540 m/s. When c is constant, a pulse from a point source yields a spherical wave propagating without generating any reflected echoes. However, this not the case in biological tissues. When an ultrasound beam is transmitted into the body, the wave is primarily scattered and reflected because

of the inhomogeneities in tissue density and compressibility. Specular reflections appear when the tissue structures within the body feature boundaries that are much larger than the wavelength. In this case, the amount of reflected echoes depends on the wave incident angle. Whereas a scatterer with size much smaller than the wavelength, the wave is reflected in the form of a spherical wave that does not depend on the incident angle (*i.e.* diffuse reflection or scattering), which provides much of the diagnostic information in medical ultrasound. The ultrasound wave is also attenuated while propagating in the tissue. This phenomenon is caused by absorption and can be characterized by the attenuation coefficient. This coefficient is different for each tissue and increases with frequency and propagation distance. Table 2.1 lists the attenuation coefficients of common biological materials at a frequency of 1 MHz.

Table 2.1: The Impact of Body Tissues on Attenuation (table from http://usra.ca/tissue.php)

Body Tissue	Attenuation Coefficient (dB/cm at 1MHz)
Water	0.002
Blood	0.18
Fat	0.63
Liver	0.5-0.94
Kidney	1.0
Muscle	1.3-3.3
Bone	5.0

2.1.3 Beamforming

Classically, the 2D cardiac images (or 3D image volumes) are constructed by successively emitting focused beams that are steered in different directions to cover the desired image sector. The process of steering and focusing the pulses from each transducer element is known as *beamforming*. In echocardiography, the most commonly used beamformer is delay and sum (DAS), which is shown schematically in Figure 2.2. The idea of DAS is to apply different delays on each piezoelectric element to reach focusing at a given point both in transmission (Figure 2.2a) and reception (Figure 2.2b).

In transmission, all the piezoelectric elements are excited at different instants (*i.e.* applying delay τ_E in Figure 2.2a) which enables the waves coming from all the elements to reach a desired point at the same time. The distance from each element (x_E, y_E, z_E) to the focal point (x_f, y_f, z_f) is:

$$r_E = \sqrt{(x_E - x_f)^2 + (y_E - y_f)^2 + (z_E - z_f)^2} \qquad (2.3)$$

Then the delay τ_E that is used on each element of the array can be easily calculated

as:

$$\tau_E = \frac{1}{c}\Delta\, r_E = \frac{1}{c}(\max\{r_E\} - r_E) \qquad (2.4)$$

where c is the speed of sound. Using such delays on the elements enables to generate an ultrasound beam steered and focused at any point in the medium.

In reception, all the signals received on each element are delayed first in the same way as in transmission (*i.e.* different delays τ_E are applied on each element to compensate the difference of wave propagation distances). All the delayed signals are then summed in order to get the final signal that contains all the contributions coming from the same point scatterer in the medium.
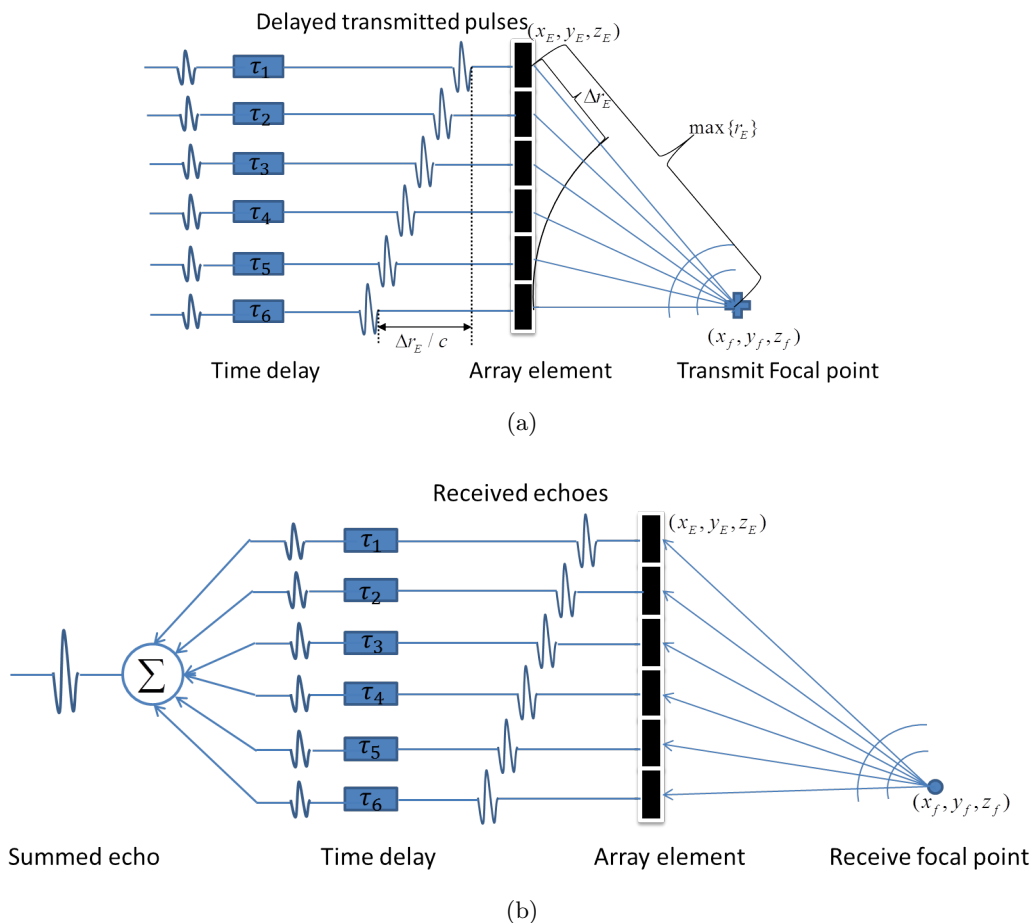
Figure 2.2: Illustration of delay and sum beamforming process. (a) In transmission, pulses from an array of piezoelectric elements are appropriately delayed (*i.e.* applying different τ_E on each element) to achieve steering and focusing at a desired focal point (x_f, y_f, z_f). (b) In reception, the echoes received from a point (x_f, y_f, z_f) at each piezoelectric element are likewise delayed first, and then summed together to form the echo signal.

2.1.4 Image quality

The quality of an ultrasound image mainly depends on the spatial resolution (*i.e.* the axial and lateral resolution) and the contrast resolution (*e.g.* contrast ratio) of the acquisition system.

Axial resolution

This resolution refers to the minimum distance that can be differentiated between two reflectors located parallel to the direction of ultrasound beam, which is mathematically equal to half the spatial pulse length (*i.e.* the product of the number of cycles in a pulse of ultrasound and the wavelength λ) [Ng and Swanevelder (2011)]. The wavelength of a pulse is determined by the ultrasound frequency f with the relation $\lambda = c/f$, c is the speed of sound. A higher frequency, therefore, corresponds to a shorter wavelength, thus gives a better axial resolution. Diagnostic medical ultrasonography usually uses transducers with frequencies of 1-20 MHz. However, the attenuation of the wave is greater when the frequency increases, leading to a shorter distance of penetration. Therefore, in echocardiography, in order to penetrate a depth as far as 8-12 cm, a lower frequency (*e.g.* 2.5 MHz is used for 2D cardiac imaging in this manuscript) is used.

Lateral resolution

This resolution is defined as the minimum distance that can be distinguished between two reflectors located perpendicular to the direction of the ultrasound beam and mainly depends on the width of beam [Ng and Swanevelder (2011)]. However, the width of the beam and hence lateral resolution varies with distance from the transducer. As explained in Section 2.1.3, by adjusting the focusing position in the beamforming process, the lateral resolution can be optimal in the region of interest.

Contrast resolution

This resolution is the ability to distinguish between objects with different amplitudes from the background, which is also a critical component in determining the imaging system's performance. Although it is determined by the inherent properties of the object, it may be enhanced at various stages in the imaging process, including compression, image memory, and the use of contrast agents [Ng and Swanevelder (2011)]. One definition of the image contrast is the contrast ratio (CR), which can be calculated using the following equation [Wijk and Thijssen (2002)]:

$$CR = 20 \log_{10} \frac{|\mu_t - \mu_b|}{\sqrt{(\sigma_t^2 + \sigma_b^2)/2}}, \tag{2.5}$$

where μ_t and μ_b (σ_t^2 and σ_b^2) are the means (variances) of gray levels in the targets and the surrounding background, respectively.

2.2   Imaging modes

During the clinical application of echocardiography, three main imaging modes are employed: M-mode (or motion mode) imaging, two-dimensional (2D or B-mode) imaging and Doppler imaging.

2.2.1   M-mode imaging

The M-mode (or motion mode) is used to represent the movements of cardiac structures over time (*i.e.* valve motion, chamber sizes, aortic root size, wall thickness, and ventricular function). It consists in continuously pulsing a single beam through the heart and receiving the echoes from the moving tissue during the cardiac cycle. A M-mode image is obtained by displaying the variation of echoes in position and along time. Since only one beam is used, the M-mode image has a very high temporal resolution, which allows to observe the tissues with very fast movements. To obtain accurate measurements, however, the M-mode beam must be placed at the appropriate locations within the heart. Nowadays, by integrating the 2D and M-mode images, one can send the M-mode beams at the appropriate direction with the guidance of 2D images. Figure 2.3 is an example of the integration of 2D and M-mode images. Firstly, a 2D image is acquired (the top image of Figure 2.3) and a single scan line (dotted line) is placed along the area of interest (*i.e.* the mitral valve). The M-mode will then show the movements of the mitral leaflets over time along the axis of the dotted line (the bottom image of Figure 2.3).
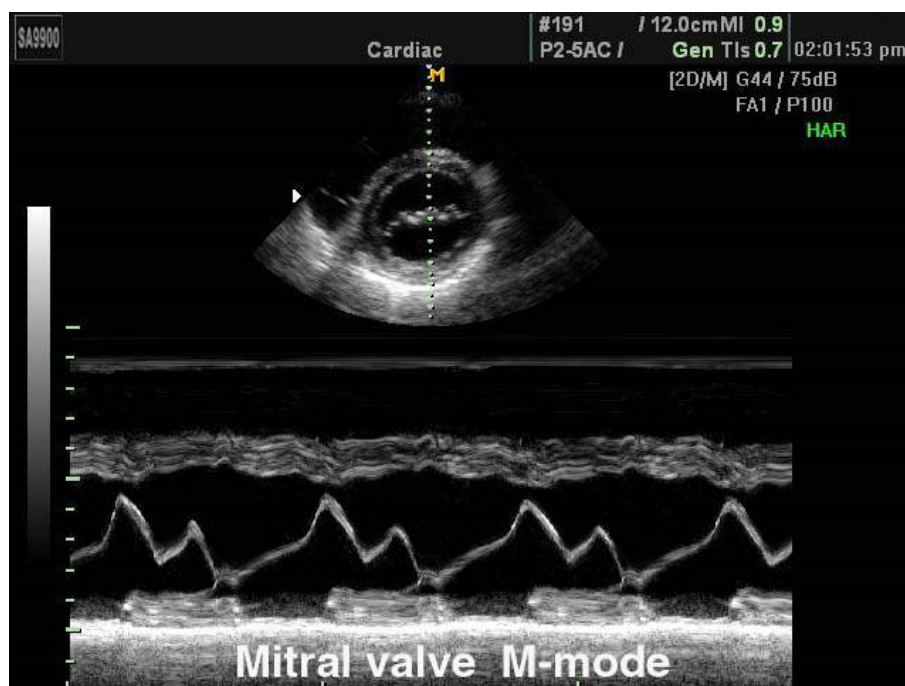
Figure 2.3:   M-mode and B-mode images.   (top) B-mode image representing a heart section.   (bottom) M-mode representation of the dotted line.   Image from http://www.medison.ru/uzi/eho177.htm

2.2.2 Two-dimensional imaging

Two-dimensional echocardiography (or B-mode) is the most widespread imaging mode in clinical routine. It consists in scanning a cross-section of the heart using ultrasound beams with different orientations and displaying the received echoes in a two-dimensional image. The position of an echo on the image is determined by its travel time (the depth) and the corresponding beam orientation (the lateral position). Because of the limited access due to the ribs, the shape of an echocardiographic image is a sector (see the top image in Figure 2.3), which allows to scan a wide region from a small access. The final image is displayed on a gray-scale: structures reflecting the ultrasound signal (*e.g.* valves) are white and non-reflecting (fluids) are black.

2.2.3 Doppler imaging

Doppler echocardiography uses the Doppler principle to determine the flow velocity, direction and characteristics in the heart as well as the velocity of myocardial tissue. A frequency shift occurs when an ultrasound beam interact with a moving targets, such as the red blood cells in the blood. This frequency shift is also related to the transmitted frequency of the transducer and the angle between the ultrasound beams and the direction of the moving targets. All these parameters are used to determine the velocity of the moving target. Then by determination of blood flow velocities, Doppler echocardiography allows various hemodynamic evaluations of the heart: transvalvular gradients and intracardiac pressures and shunts; measures of systolic cardiac performance by stroke volume and cardiac output; severity of valvular lesions; measures of diastolic cardiac performance; and differentiation between myocardial and pericardial diseases [Anavekar and Oh (2009)].

There are two types of Doppler echocardiography: the continuous wave and pulsed wave Doppler. Continuous wave Doppler can detect the frequency shift of very high velocities, but does not indicate where this shift occurs along the transmission depth. Pulsed wave Doppler uses short bursts or pulses of ultrasound alternating with pauses to detect frequency shift. This technique allows to select Doppler information from a particular location within the heart, but the maximum velocity that can be measured is limited by the pulse repetition frequency.

Color flow Doppler echocardiography is based on pulsed wave Doppler principles and displays the velocity of blood flows using a color map. With this technique, multiple sample volumes are analyzed along multiple scan lines. The mean frequency shift obtained from these many sample volumes is color coded for velocity and displayed as color flow superimposed on the 2D image. Conventionally, blood flowing away from the probe is color coded in blue and blood flowing toward the probe in red. A third color, usually yellow or green, shows areas of accelerated or turbulent flow, which is useful for determining valvular regurgitation, visualization of intra-cardiac shunting, or assessment of arterial connections. Figure 2.4 gives an example of color Doppler imaging of a mitral regurgitation.
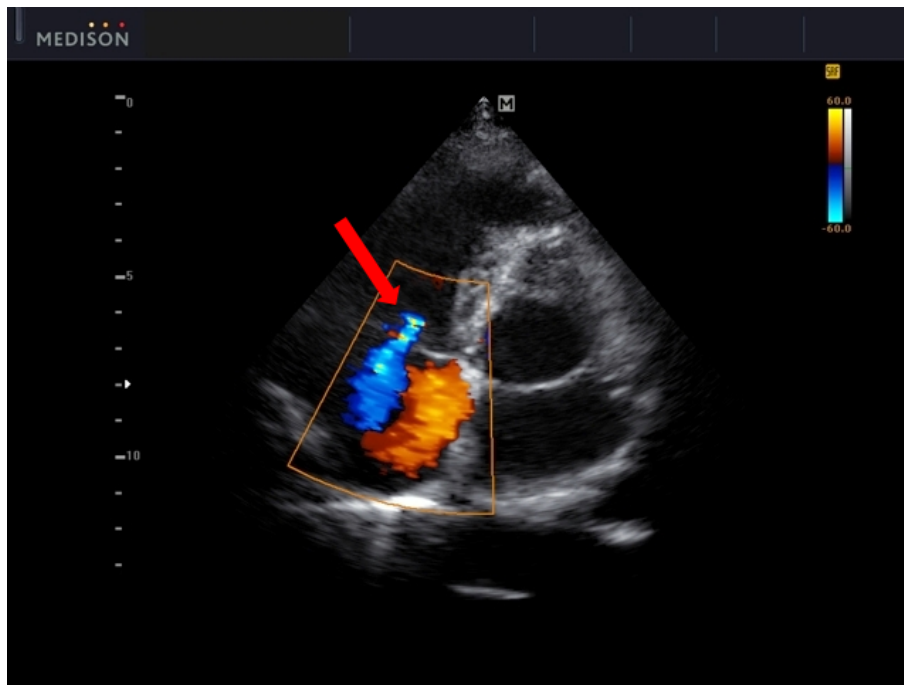
Figure 2.4: An example of color flow Doppler imaging of a mitral regurgitation. Image from http://www.medison.ru/uzi/eho562.htm

2.3 Summary

We described in this chapter the basic concepts involved in the ultrasound image formation process, including the way how transducers transmit and receive ultrasound signals, how the ultrasound wave propagates and interacts with the tissue, the beamforming method and the image quality. The three main imaging modes used in clinical are also introduced, *i.e.* M-mode, B-mode and Doppler mode.

Chapter 3

State of the art: ultrafast ultrasound imaging methods

In this chapter, we first present the various existing ultrafast ultrasound imaging methods with both PW and DW in transmission. Since the image quality is significantly reduced with a single wave, the principle of coherent compounding is then introduced. Finally, the motion compensation methods for ultrafast imaging of moving targets are also presented.

3.1 Ultrafast ultrasound imaging methods

As described in Section 1.1 and summarized in [Cikes *et al.* (2014)], the current state-of-the-art ultrafast cardiac imaging methods include the parallel receive beamforming (also called multiline acquisition (MLA) in [Cikes *et al.* (2014)]), the ECG gating, the multiline transmit imaging (MLT) and the PW/DW imaging. With the first two techniques, the maximum frame rate reached is still limited (*i.e.* 2, 4-fold increase in frame rate) because of the degradation of image quality (*i.e.* lower resolution, stitching artifacts). It was demonstrated in [Cikes *et al.* (2014), Tong *et al.* (2014)] that the MLT can gain 12 or 16-fold increase in frame rate without significant loss in image quality when set up adequately. PW/DW imaging are very promising techniques for reaching very high frame rate with controlled image quality. These techniques use PW or DW to insonify the whole medium with one single emission. The backscattered echoes are then measured and post-processed to reconstruct simultaneously all lines of the image of interest. In the following subsections, the existing PW and DW imaging methods will be briefly summarized. An overview of these methods is given in table 3.1.

Table 3.1: Overview of existing ultrafast imaging methods based on plane/diverging wave insonifications

Wave Type	First Author (References)	Performing dimensions/domain
Plane wave	Lu *et al.* [Lu (1997), Cheng and Lu (2006)]	2D and 3D/ Fourier domain
	Montaldo *et al.* [Montaldo *et al.* (2009)]	2D/ Spatial domain
	Garcia *et al.* [Garcia *et al.* (2013)]	2D/ Fourier domain
	Provost *et al.* [Provost *et al.* (2014)]	3D/ Spatial domain
Diverging wave	Hasegawa *et al.* [Hasegawa and Kanai (2011)]	2D/ Spatial domain
	Papadacci *et al.* [Papadacci *et al.* (2014)]	2D/ Spatial domain
	Provost *et al.* [Provost *et al.* (2014)]	3D/ Spatial domain

3.1.1 Plane wave imaging

Lu's method

Lu *et al.* developed a 2D and 3D high frame rate imaging method in the late 90s based on the X wave theory [Lu (1997), Lu (1998)], which has been recently extended to include various transmission schemes, such as multiple limited-diffraction beams and steered PW [Cheng and Lu (2006)]. The following is a brief summary of Lu's method with steered PW in transmission.

Let us assume that there is a 2D array transducer (a 1D array being a special case) located at $z = 0$ plane and excited to generate steered PW. The received signal for echoes returned from all the scatterers in the medium can be expressed as (see Eq. (7) and (8) in [Cheng and Lu (2006)]):

$$R_{k_x+k_{xT}, k_y+k_{yT}, k_z+k_{zT}}(t) = \int_V f(\vec{r}_0) \left[\Phi^T_{Array}(\vec{r}_0, t) * \Phi^R_{Array}(\vec{r}_0, t) \right] d\vec{r}_0$$

$$= \frac{1}{2\pi} \int_{-\infty}^{\infty} \frac{A(k)T(k)H(k)}{c} F(k_x + k_{xT}, k_y + k_{yT}, k_z + k_{zT}) e^{-iwt} dk \qquad (3.1)$$

Where $f(\vec{r}_0)$ is the object function (*i.e.* the spatial distribution of the reflection coefficient), t is the time, V is the volume of the object and $\vec{r}_0 = (x_0, y_0, z_0)$ represents the coordinates of any spatial point in the object. $*$ represents the convolution, $F(\cdot)$ is the Fourier transform of the object function $f(\vec{r}_0)$. $\vec{K}^T = (k_{xT}, k_{yT}, k_{zT})$ and $\vec{K}^R = (k_x, k_y, k_z)$ are the wave vectors of the beams in transmission and in reception, with the relation $k_{zT} = \sqrt{k^2 - k_{xT}^2 - k_{yT}^2} \geq 0$ and $k_z = \sqrt{k^2 - k_x^2 - k_y^2} \geq 0$, where $k = w/c$ is the wave

number, $w = 2\pi f$ is the angular frequency, f is the temporal frequency and c is the speed of the sound in the medium. $\Phi_{Array}^T(\vec{r}_0, t)$ and $\Phi_{Array}^R(\vec{r}_0, t)$ are the PW in transmission and reception, where (see Eq.(1) and (5) in [Cheng and Lu (2006)]):

$$\Phi_{Array}^T(\vec{r}_0, t) = \frac{1}{2\pi} \int_{-\infty}^{\infty} A(k)H(k)e^{ik_{xT}x_0 + ik_{yT}y_0 + ik_{zT}z_0}\, e^{-iwt}\, \mathrm{d}\,k \qquad (3.2)$$

and

$$\Phi_{Array}^R(\vec{r}_0, t) = \frac{1}{2\pi} \int_{-\infty}^{\infty} T(k)H(k)e^{ik_x x_0 + ik_y y_0 + ik_z z_0}\, e^{-iwt}\, \mathrm{d}\,k \qquad (3.3)$$

The Fourier transform of $\Phi_{Array}^T(\vec{r}_0, t)$ and $\Phi_{Array}^R(\vec{r}_0, t)$ are (see Eq.(2) and (5) in [Cheng and Lu (2006)]):

$$\widetilde{\Phi}_{Array}^T(\vec{r}_0, w) = \frac{A(k)H(k)}{c} e^{ik_{xT}x_0 + ik_{yT}y_0 + ik_{zT}z_0} \qquad (3.4)$$

and

$$\widetilde{\Phi}_{Array}^R(\vec{r}_0, w) = \frac{T(k)H(k)}{c} e^{ik_x x_0 + ik_y y_0 + ik_z z_0} \qquad (3.5)$$

Where $A(k)$ and $T(k)$ are the transfer function of the transducer for transmission and reception, $H(k)$ is the Heaviside step function.

By taking the temporal Fourier transform of the received signal $R_{k_x+k_{xT}, k_y+k_{yT}, k_z+k_{zT}}(t)$ in Eq.(3.1), one can obtain the relationship between the Fourier transform of the object function $F(k_x', k_y', k_z')$ and the Fourier transform of the received echo signals $\widetilde{R}_{k_x', k_y', k_z'}(w)$ (see Eq.(10) and (11) in [Cheng and Lu (2006)]):

$$\widetilde{R}_{k_x', k_y', k_z'}(w) = \frac{A(k)T(k)H(k)}{c^2} F(k_x', k_y', k_z') \qquad (3.6)$$

with:

$$\begin{cases} k_x' = k_x + k_{xT} \\[2mm] k_y' = k_y + k_{yT} \\[2mm] k_z' = k_z + k_{zT} = \sqrt{k^2 - k_x^2 - k_y^2} + \sqrt{k^2 - k_{xT}^2 - k_{yT}^2} \geq 0 \end{cases} \qquad (3.7)$$

The Eq.(3.6) and (3.7) give a general 3D image reconstruction formula. By setting $k_y = k_{yT} = 0$, one can easily obtain the 2D imaging formula (see Eq.(35) and (36) in [Cheng and Lu (2006)]):

$$\widetilde{R}_{k_x', k_z'}(w) = \frac{A(k)T(k)H(k)}{c^2} F(k_x', k_z') \qquad (3.8)$$

with:

$$\begin{cases} k'_x = k_x + k_{xT} \\ k'_z = k_z + k_{zT} = \sqrt{k^2 - k_x^2} + \sqrt{k^2 - k_{xT}^2} \geq 0 \end{cases} \tag{3.9}$$

For 2D steered PW with angle θ, $k_{xT} = k\sin\theta$, from Eq.(3.9), one can obtain the inverse function (see Eq.(43) in [Cheng and Lu (2006)]):

$$\begin{cases} k_x = k'_x - k\sin\theta \\ k = \frac{k'^2_x + k'^2_z}{2k'_x \sin\theta + 2k'_z \cos\theta} \end{cases} \tag{3.10}$$

From the above Eq.(3.10), the mapping between the Fourier transform of the echo signals in (k_x, k) space and the Fourier transform of the object function in (k'_x, k'_z) space can be done with interpolation. After getting the spectrum of object, by simply taking a 2D inverse Fourier transform, one can obtain the beamformed image.

Garcia's method

More recently, Garcia *et al.* proposed a f-k migration method in [Garcia *et al.* (2013)] for 2D PW imaging based on the exploding reflector model (ERM), which assumes that all the reflectors in the medium explode simultaneously and become upward-emitting acoustic sources [Gazdag and Sguazzero (1984)]. By using the virtual exploding sources, the ERM can reflect the actual two-way propagation of the acoustic wave accurately. Then by applying the Stolt's method to find these virtual sources and applying a spatial transformation, the actual scatterers' positions can be recovered. The following is a brief summary of Garcia's method with steered PW in transmission.

To make the ERM compatible with the steered PW acquisition, one must fit the hyperbolas of the travel time given by ERM and PW insonifications. For a steered PW with angle θ (see Figure 3.1a), the travel time of such a PW to reach a scatterer positioned at (x_s, z_s) and back to the transducer position x can be characterized by the following equation (see Eq.(6) in [Garcia *et al.* (2013)]):

$$\tau_s(x) = \frac{1}{c}(\sin(\theta)(x_s - x) + \cos(\theta)z_s + \sqrt{(x_s - x)^2 + z_s^2}) \tag{3.11}$$

where c is the wave propagation speed and is assumed constant in the insonified tissues, the $(x_s - x)$ operator is used to eliminate the leading zero signals caused by the emission delays.

For an exploding source at $(\hat{x}_s, \hat{z}_s)$ with a constant propagation speed $\hat{c}$, the ERM
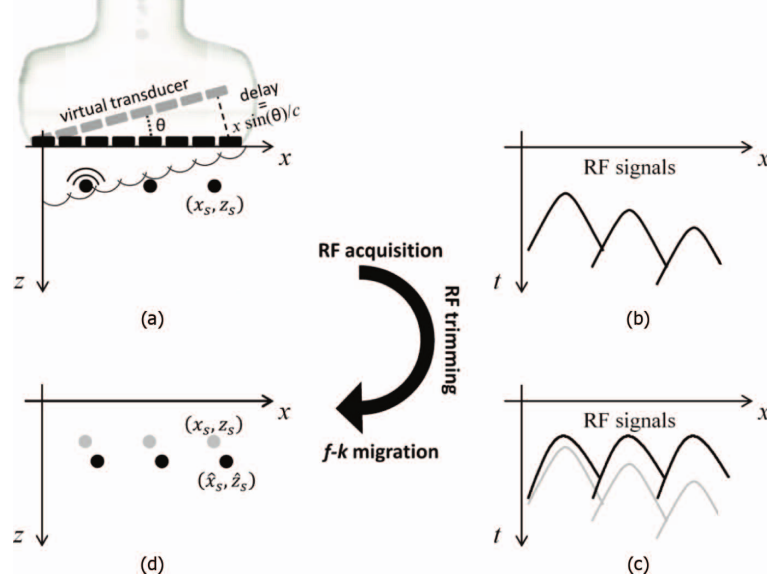
Figure 3.1: (Figure 4 in [Garcia *et al.* (2013)]) Adapting the f-k migration to steered PW imaging. (a) A slant PW is emitted. In this example, the leftmost scatterer is the first to perceive the planar wavefield. (b) The resulting diffraction hyperbolas in the RF echoes are not aligned. (c) Trimming the RF signals realigns the hyperbolas horizontally (from gray to black). (d) A scatterer originally located at (x_s, z_s) will be moved to $(\hat{x}_s, \hat{z}_s)$ after the f-k migration.

travel time is (see Eq.(2) in [Garcia *et al.* (2013)]):

$$\hat{\tau}_s(x) = \frac{1}{\hat{c}}\sqrt{(\hat{x}_s - x)^2 + \hat{z}_s^2} \tag{3.12}$$

By equating τ_s and $\hat{\tau}_s$ as well as their first and second derivatives (with respect to x) at $x = x_s$, provides the following relations (see Eq.(7) and Eq.(9) in [Garcia *et al.* (2013)]):

$$\begin{cases} \hat{c} = \frac{1}{\sqrt{1+\cos\theta+\sin^2\theta}}c \\[2ex] \hat{z}_s = \frac{(1+\cos\theta)^{3/2}}{1+\cos\theta+\sin^2\theta}z_s \\[2ex] \hat{x}_s = x_s + \frac{\sin\theta}{2-\cos\theta}z_s \end{cases} \tag{3.13}$$

Thus the ERM can be generalized to model the PW acquisition adequately. The whole process is described in Figure 3.1 (see Figure 4 in [Garcia *et al.* (2013)]).

For a constant ERM propagation speed $\hat{c}$, the Stolt's migration solution can be obtained (see Eq.(14) and (15) in [Garcia *et al.* (2013)]):

$$\Psi(x, z, 0) = \iint_{-\infty}^{\infty} \frac{\hat{c}\hat{k}_z}{\sqrt{k_x^2 + \hat{k}_z^2}}\phi(k_x, 0, f(\hat{k}_z))e^{2i\pi(k_x x - \hat{k}_z z)}\mathrm{d}k_x \mathrm{d}\hat{k}_z \tag{3.14}$$

with

$$f(\hat{k}_z) = \hat{c}\,\text{sign}(\hat{k}_z)\sqrt{{k_x}^2 + \hat{k}_z^2} \tag{3.15}$$

where $\Psi(x, z, t = 0)$ is the wavefield at the time of explosion. $\phi(k_x, 0, f)$ is the Fourier transform of $\Psi(x, z = 0, t)$ over (x, t). $\Psi(x, z = 0, t)$ represents the ERM wavefield on the surface. k_x and $\hat{k}_z$ are the spatial wavenumber related to x and z and f is the temporal frequency.

As shown by Eq.(3.14), the migrated solution is basically the inverse Fourier transform of (see Eq.(16) in [Garcia *et al.* (2013)]):

$$\frac{\hat{c}\hat{k}_z}{\sqrt{{k_x}^2 + \hat{k}_z^2}}\phi(k_x, 0, f(\hat{k}_z)) \tag{3.16}$$

Montaldo's methods
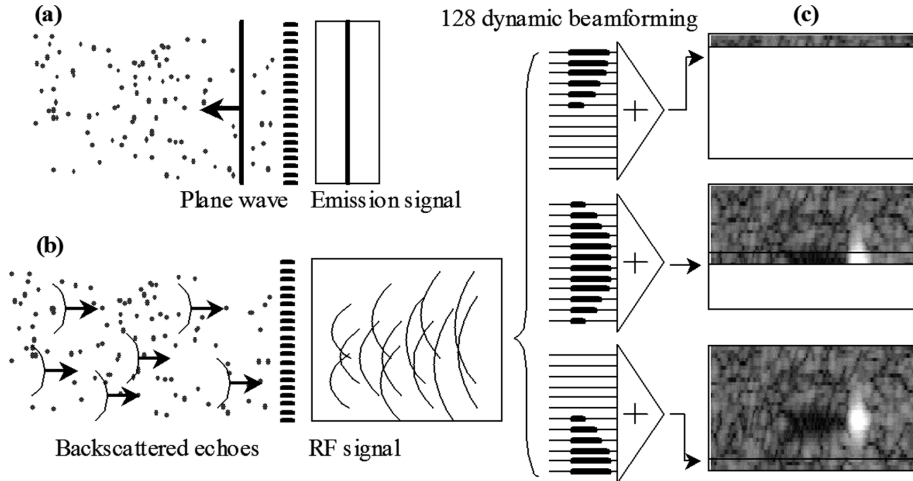
Figure 3.2: (Figure 2 in [Montaldo *et al.* (2009)]) Schematic representation of the single transmit PW method. (a) The ultrasonic array insonifies the medium using a PW transmission. (b) The backscattered RF signals are recorded by the transducer array. (c) The beamforming procedure consists in applying time delays laws and summations to the raw RF signals to focus in the receive mode. Contrary to standard ultrasonography, each line of the image is calculated using the same RF data set but a different set of time delays.

Unlike the methods of Lu and Garcia, Montaldo *et al.* introduced a 2D time domain PW imaging method which is based on the principle of delay-and-sum (DAS) beamforming [Montaldo *et al.* (2009)]. Contrary to the conventional ultrasonography, this method allows to reconstruct the entire image simultaneously from only one transmission. The whole process of this method for a single PW is presented in Figure 3.2 (see Figure 2 in [Montaldo *et al.* (2009)]). A PW is transmitted into the medium by exciting the transducer elements simultaneously (see Figure 3.2a) and the backscattered echoes $RF(x, t)$ are acquired by each element with the position x (see Figure 3.2b). Then by applying time delays on the raw RF signals and adding coherently, the whole image is obtained (see Figure 3.2c).

For a steered PW with angle θ (see Figure 3.1a), the travel time to the point (x_s, z_s) and back to a transducer element placed in x can be expressed as (see Eq.(4) to (6) in [Montaldo *et al.* (2009)]):

$$\tau(x, x_s, z_s) = \frac{1}{c}(\sin(\theta)x_s + \cos(\theta)z_s + \sqrt{(x_s - x)^2 + z_s^2}) \tag{3.17}$$

Each pixel of the image (x_s, z_s) is obtained by delaying the $RF(x, t)$ signals with $\tau(x, x_s, z_s)$ and adding coherently in the transducer direction x (see Eq.(2) in [Montaldo *et al.* (2009)]):

$$s(x_s, z_s) = \int_{x_s - a}^{x_s + a} RF(x, \tau(x, x_s, z_s)) \mathrm{d}x \tag{3.18}$$

The aperture $2a$ represents the elements that contribute to the signal and can be expressed by the F-number (see Eq.(3) in [Montaldo *et al.* (2009)]):

$$F = \frac{z}{2a} \tag{3.19}$$

where z represents the depth of the image. Ideally, the F-number is constant in the entire image.

3.1.2 Diverging wave imaging

Very recently, Papadacci *et al.* and Provost *et al.* proposed to adapt Montaldo's method to ultrafast imaging with DW in transmission for imaging the heart in 2D [Papadacci *et al.* (2014)] and 3D [Provost *et al.* (2014)], respectively. Each transmitted DW is defined by the position of a virtual source located behind the probe and used to insonify the entire field of view. Hasegawa *et al.* have also proposed a similar approach to perform high frame rate imaging in 2D echocardiography, but using several diverging beams with different directions to cover the entire medium (15 transmits in [Hasegawa and Kanai (2011)]). The beamforming process of the above three methods is also based on the DAS principle, which can be summarized as follows.

If we send a 2D DW with virtual source positioned at (x_v, z_v), the time to travel to a point (x_s, z_s) in the medium and come back to a transducer placed in x is:

$$\tau(x, x_s, z_s, x_v, z_v) = \frac{1}{c}(\sqrt{(x_s - x_v)^2 + (z_s - z_v)^2} + \sqrt{(x_s - x)^2 + z_s^2}) \tag{3.20}$$

Then a 2D sectorial image can be obtained in the same way as shown in the previous subsection, but with the new delays from Eq.(3.20) in Eq.(3.18).

The above framework can be easily extended to 3D by using a 2D matrix array instead of a 1D probe. In this case, one has to take into account the y-coordinate in Eq.(3.20), and the travel time τ of a 3D DW becomes:

$$\tau(x, y, x_s, y_s, z_s, x_v, y_v, z_v) = \frac{1}{c} \Big(\sqrt{(x_s - x_v)^2 + (y_s - y_v)^2 + (z_s - z_v)^2}$$
$$+ \sqrt{(x_s - x)^2 + (y_s - y)^2 + z_s^2} \, \Big) \quad (3.21)$$

Then each pixel of the volume (x_s, y_s, z_s) can be obtained by delaying the $RF(x, y, t)$ signals with $\tau(x, y, x_s, y_s, z_s, x_v, y_v, z_v)$ and adding coherently in the two transducer directions x and y, thus Eq.(3.18) becomes:

$$s(x_s, y_s, z_s) = \int_{x_s-a}^{x_s+a} \int_{y_s-b}^{y_s+b} RF(x, y, \tau(x, y, x_s, y_s, z_s, x_v, y_v, z_v)) \mathrm{d}x \mathrm{d}y \quad (3.22)$$

Where aperture $2a$ and $2b$ represent the elements that contribute to the signals in x and y direction, respectively.

Note that a 3D PW can be obtained by a virtual source positioned at infinity behind the probe. Thus the 3D PW imaging can be implemented in the same framework as DW imaging.

3.2 Principle of coherent compounding

The insonification with a single wave (PW or DW) provides the highest frame rate, but comes up with an image quality (defined in terms of resolution and contrast) intrinsically lower than the one obtained with classical multi-line focused beamforming. To overcome this limitation, spatial coherent compounding has been used in all the studies mentioned above to improve image quality. By using several PW of different angles (or DW of different virtual source positions), synthetic focus is achieved in the whole image, as it is done in synthetic transmit aperture (STA) [Jensen *et al.* (2006)a].

Figure 3.3 shows the principle of coherent PW compounding. Steered PW are sent by the transducer and insonify the whole region of interest. An ultrasound image is computed from each single insonification. The individual image obtained from each PW is a low quality image. The coherent summation of these images creates synthetic focus throughout the image and allows to recover a high quality image. It has been shown in [Montaldo *et al.* (2009)] that the synthetic focusing reached by coherent compounding is the same as in the standard focusing method for an adequate number of PW (*i.e.* 71 PW in transmission corresponding to a frame rate of 176 Hz in [Montaldo *et al.* (2009)]), which allows to have the same image quality in both methods.

Figure 3.4 (Figure 1 in [Papadacci *et al.* (2014)]) shows the principle of coherent compounding with DW in transmission. Each wave is transmitted individually into the medium (Figure 3.4a). By applying adequate delays on each wave, the coherent summation of these waves enables to focus at different depths and lateral positions ((b),(c),(d) in Figure 3.4).
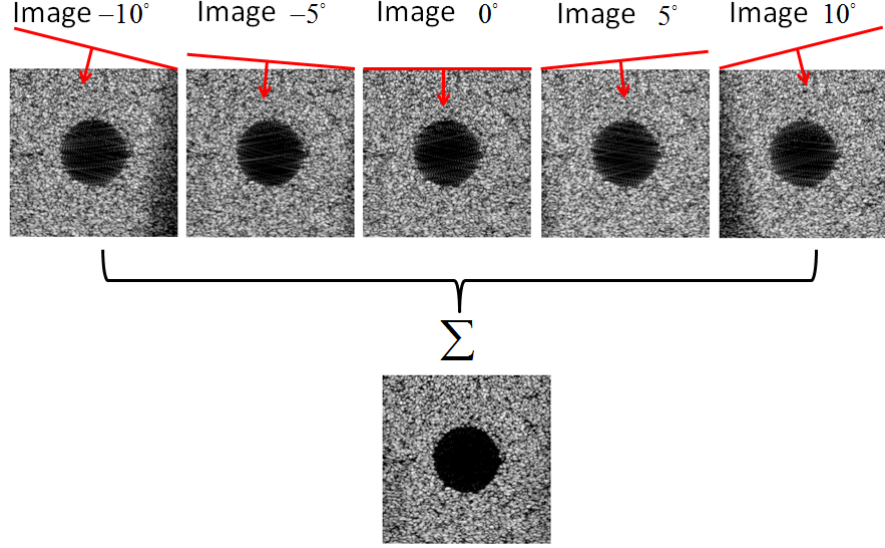
Figure 3.3: Principle of coherent PW compounding. The medium is insonified with steered PW, and the images are reconstructed individually for each PW. The individual images obtained from each PW are low quality images. The coherent summation of these images creates synthetic focusing throughout the complete image and allows to recover a high quality image.
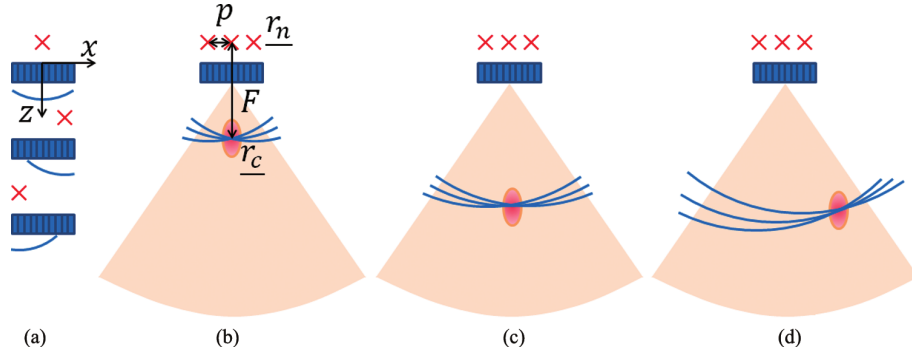
Figure 3.4: (Figure 1 in [Papadacci *et al.* (2014)]) Principle of coherent compounding with DW. (a) Three DW defined by their virtual source (red crosses at r_n) spaced by a virtual pitch p, are sent independently with a phased array probe directly in contact with the region of interest. Each DW is backscattered by heterogeneities and the array receives the corresponding echo. beamforming is performed, applying delays corresponding to a constructive interference of these DW at the focal point r_c. (b) by changing the delay applied to each of the backscattered echoes from (a), the resulting waves can interfere and virtually focus at different depths, as in (c), and lateral positions, as in (d).

3.3 Motion compensation methods for ultrafast imaging

As described above, the final image produced by ultrafast imaging techniques (based on PW and DW insonifications) are dependent on the coherent summation of images obtained from several emissions, thus synthetic focus is achieved in the full image. However, when the scatterers move rapidly between two transmits, a time shift appears in the two

successive received beamformed signals, resulting in a degradation of the image quality during coherent compounding [Wang and Lu (2007)]. When the motion is less than $\lambda/4$ (λ representing the wavelength), this time shift can be approximated by a phase shift in the received quadrature-demodulated (IQ) signals [Denarie *et al.* (2013)b]. For moving tissues, this phase shift must be taken into account during the compounding process to decrease the image artifacts caused by motion.

Several approaches have thus been proposed to tackle this problem in synthetic transmit aperture imaging (STAI) [Trahey and Nock (1992), Kim *et al.* (2002), Oddershede and Jensen (2007), Yiu *et al.* (2008), Gammelmark and Jensen (2014)]. Very recently, the motion compensation methods adapted to coherent compounding with PW and DW insonifications were investigated in [Denarie *et al.* (2013)b] and [Poree *et al.* (2016)], respectively. For both methods, only radial motion (*i.e.* motion perpendicular to the transducer surface) is considered since lateral motion (*i.e.* motion parallel to the transducer surface) is expected to have a smaller influence on the image [Wang and Lu (2007)]. The following is a brief summary of the two methods. For more details, the reader is referred to the original papers [Denarie *et al.* (2013)b, Poree *et al.* (2016)].

3.3.1 Cross-correlation based motion compensation method for plane wave imaging

In order to reduce the motion artifacts on PW compounded images, Denarie *et al.* proposed a transmit sequence with angles alternatively negative and positive (*i.e.* transmit angle sequences $[-\alpha_N, \alpha_N, -\alpha_{N-1}, \alpha_{N-1}, \ldots, -\alpha_1, \alpha_1, 0]$), which allows reducing the influence of motion while keeping the same contrast as the classical linear sequences (*i.e.* $[-\alpha_N, -\alpha_{N-1}, \ldots, -\alpha_1, 0, \alpha_1, \ldots, \alpha_{N-1}, \alpha_N]$) [Denarie *et al.* (2013)b]. However, the proposed transmit sequence cannot fully cancel the motion artifacts, so Denarie *et al.* [Denarie *et al.* (2013)b] proposed to adapt the cross-correlation method to estimate the motion between each PW acquisition and correct it before coherent compounding. When the motion is sufficiently small, the phase shift between two successive received IQ signals can be approximated to (see Eq.(9) in [Denarie *et al.* (2013)b]):

$$\angle x_{\alpha_{n+1}, m} - \angle x_{\alpha_n, m} \approx \frac{4\pi \cdot f_0}{\text{PRF}} \cdot \frac{v_{rad}}{c} \tag{3.23}$$

where $x_{\alpha_n, m}$ is the IQ signal received for the PW transmitted at an angle α_n and beamformed for the lateral line m, f_0 is the demodulation frequency, v_{rad} is the radial velocity of the scatterers which is assumed to be constant, c is the sound velocity, and PRF is the pulse repetition frequency of the system.

This phase shift can also be estimated by computing the phase angle of the cross-correlation $R_{n,m}^1$ between two received beams (see Eq.(10) in [Denarie *et al.* (2013)b]):

$$\angle R_{n,m}^1 = \angle \langle x_{\alpha_n, m}^{\star} \cdot x_{\alpha_{n+1}, m} \rangle \approx \angle x_{\alpha_{n+1}, m} - \angle x_{\alpha_n, m} \tag{3.24}$$

where $x^{\star}_{\alpha_n,m}$ is the complex conjugate of $x_{\alpha_n,m}$.

Using the combination of Eq.(3.23) and Eq.(3.24), the radial velocity v_{rad} can be easily estimated. Once the velocities are estimated, the low-resolution images can be corrected using a local phase rotation on the IQ data. This is valid only for the radial displacement lower than a quarter of a wavelength of the demodulation frequency. For rapidly moving tissues like myocardium, however, the correction process must consist of both a phase rotation and a delay (see Eq.(11) and (12) in [Denarie *et al.* (2013)b]):

$$\tau_{n_0,m}(t) = \sum_{n=n_0}^{n=N/2} \frac{\angle R_{n,m}^1(t)}{2\pi \cdot f_0} \tag{3.25}$$

$$\hat{x}_{\alpha_n,m} = x_{\alpha_{n+1},m}(t + \tau_{n,m}(t)) \cdot e^{i \cdot 2\pi \cdot f_0 \cdot \tau_{n,m}(t)} \tag{3.26}$$

In order to improve the motion estimation, it was chosen to take the average of the cross-correlation functions $R_{m,n}^1$ for all pairs of successive transmit PW ($n \in [1, N-1]$). Since the difference in the diffraction patterns may also result in a phase shift of their cross-correlation, the authors proposed to reject the false velocities by applying the following two thresholds before averaging (see Eq.(13) and (14) in [Denarie *et al.* (2013)b]):

$$\angle R_{n,m}^1 < T = \frac{4\pi \cdot f_0}{\text{PRF}} \cdot \frac{v_T}{c} \tag{3.27}$$

$$\left(\frac{\sum_{n=1}^{N-1} \angle R_{n,m}^1 - \overline{\angle R_m^1}}{N-2} \right)^{\frac{1}{2}} < T_{std} = p \cdot T \cdot \sqrt{D} \tag{3.28}$$

where v_T represents the maximum velocity that can be observed in the tissue, D is the decimation factor in the transmitted sequences, and $p \in (0,1)$.

3.3.2 Doppler-based motion compensation for diverging wave imaging

In a recent paper, Poree *et al.* proposed a motion compensation (MoCo) strategy for high frame rate echocardiography, *i.e.* using a sequence of DW in transmission [Poree *et al.* (2016)]. To eliminate the artifacts due to the sidelobes, the authors proposed to use a triangle sequence (Figure 3.5). Two lag-one autocorrelations corresponding to the ascending and descending slopes of the triangle sequence were calculated by (see Eq.(3) in [Poree *et al.* (2016)]) :

$$\Re_1(\theta, r) = \sum_{m=1}^{\frac{M}{2}-1} \frac{\widetilde{s_m}\overline{\widetilde{s_{m+1}}}}{\left| \widetilde{s_m}\overline{\widetilde{s_{m+1}}} \right|} \tag{3.29}$$

and

$$\Re_2(\theta, r) = \sum_{m=\frac{M}{2}}^{M-1} \frac{\widetilde{s_m}\overline{\widetilde{s_{m+1}}}}{\left| \widetilde{s_m}\overline{\widetilde{s_{m+1}}} \right|} \tag{3.30}$$
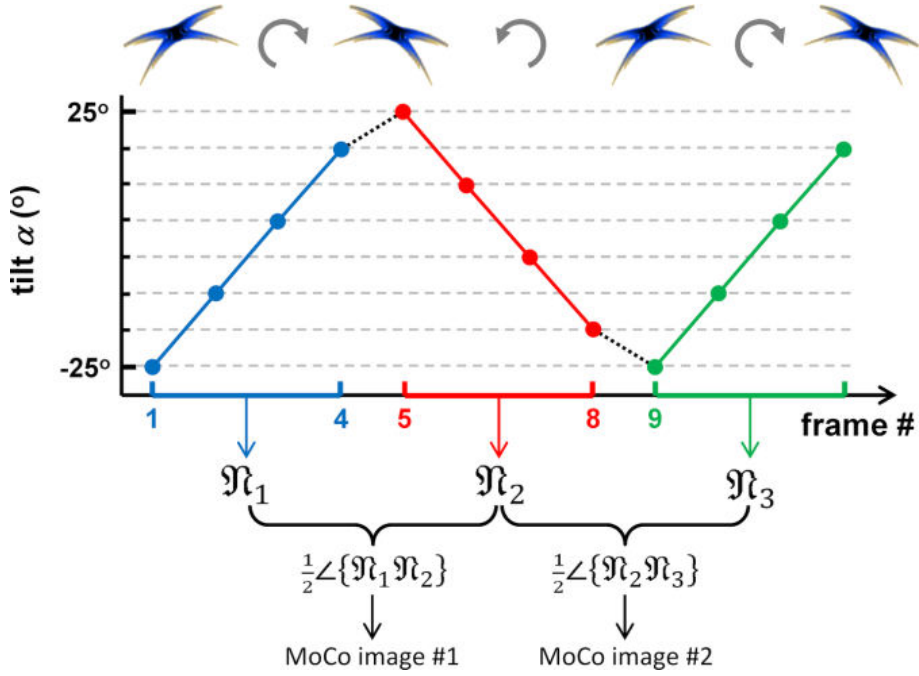
Figure 3.5: (Figure 3 in [Poree *et al.* (2016)]) Triangle transmit sequences & motion estimation. To reduce the side effects due to sidelobes, a triangle sequence composed of 32 successive transmits is used. This figure shows an 8-transmit sequence for clarity. Slow-time autocorrelations were calculated in the ascending and descending stages, and their product was used to estimate the phase delays due to motion. The insets on the top represent the PSFs (point spread functions) with the apparent sidelobes. They rotate in clockwise then counter-clockwise directions.

where $\widetilde{s_m}$ represents the mth slow-time IQ sample (in a total packet of M samples) determined at (θ, r). Thus the phase delays due to motion can be estimated by (see Eq.(4) in [Poree *et al.* (2016)]):

$$\phi_{MoCo}(\theta, r) = \frac{1}{2} \angle \{\Re_1 \, \Re_2\} \tag{3.31}$$

Then by compensating the displacements and phase rotations on each lower-resolution image (Figure 3.6) and doing coherent summation, the final compounded image can be obtained (see Eq.(5) in [Poree *et al.* (2016)]):

$$\widetilde{s}_C(\theta, r) = \sum_{m=1}^{M} \left\{ \widetilde{s_m} \left(\theta, r + (m - \frac{M}{2}) \frac{\phi_{MoCo}}{4\pi} \frac{c}{f_0} \right) e^{im\phi_{MoCo}} \right\} \tag{3.32}$$

Tissue Doppler velocity is (see Eq.(6) in [Poree *et al.* (2016)]):

$$V_D = \frac{\text{PRF} c}{4\pi \, f_0} \phi_{MoCo} \tag{3.33}$$
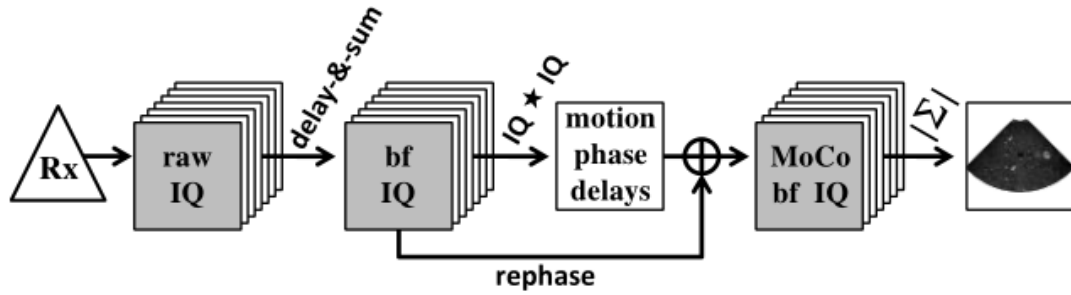
Figure 3.6: (Figure 5 in [Poree *et al.* (2016)]) Coherent compounding with integrated MoCo. Rx = receive, bf = beamformed, MoCo = motion compensation. The five-point star represents the autocorrelation. 1) A series of M tilted beams arranged in a triangle sequence is transmitted. 2) M raw complex envelope (IQ, in-phase and quadrature) images are obtained. 3) These M complex envelopes are migrated to get beamformed complex images (bf IQ). 4) Slow-time autocorrelations return the phase delays due to tissue motion. 5) These phase delays are used to rephase the beamformed complex images and get motion-compensated beamformed complex images (MoCo bf IQ). 6) The motion-compensated beamformed complex images are summed; the modulus of the resulting image is log-compressed to give a B-mode image.

3.4 Summary

In this chapter, we introduced the current existing ultrafast imaging methods that are based on PW and DW insonifications. To acquire an image of comparable quality as conventional focusing, the principle of coherent compounding is then presented. In particular, synthetic focus is achieved in the whole image after spatial coherent compounding over several images. However, when the tissue is moving between two successive transmits, perfect synthetic focus is no longer achieved, resulting in image artifacts. Therefore, the motion compensation methods for ultrafast imaging of moving targets are also presented in this chapter.

III   Contributions

Chapter 4

Revisiting the influence of transmission scheme involved in ultrafast imaging with plane waves

In this chapter, a complete study is given to revisit the influence of the transmission scheme on the PW imaging system. Based on an analytical study of the problem, we consider a so-called efficient dichotomous transmission scheme for linear acquisition which allows improving the quality of the reconstructed images at a constant frame rate. The efficiency of the transmission dichotomous scheme is assessed through the use of the current state-of-the-art reconstruction algorithms for high frame rate imaging. The quality of the reconstructed images is evaluated in terms of resolution and contrast from both simulations and *in vitro* experiments. Comparison with the regular transmission scheme demonstrates the potential of the dichotomous approach which allows to divide by a factor of four the number of steered PW while maintaining the same image quality.

4.1 Introduction

As discussed in Chapter 3, PW imaging in ultrasound [Tanter and Fink (2014)] is an intense area of research because of its capacity of reaching frame rate higher than a thousand of frames per second, leading to applications with strong potential in medical ultrasound [Udesen *et al.* (2008), Montaldo *et al.* (2009), Gennisson *et al.* (2010), Bercoff *et al.* (2011), Provost *et al.* (2011), Lenge *et al.* (2014), Ricci *et al.* (2014), Ekroll *et al.*

(2014), Ekroll *et al.* (2015), Salles *et al.* (2015), Muller *et al.* (2015), Provost *et al.* (2015)]. Contrary to the historical line-by-line focused beams approach, this technique is based on the reconstruction of a conventional B-mode image from the transmission of one or several steered PW.

Although PW imaging appears to be attractive, the images obtained using a single PW suffer from an intrinsic lower quality (defined in terms of resolution and contrast) as compared to the conventional multi-lines focused beamforming technique, especially for large depths. Coherent compounding based on the transmission of N steered PW with different angles corresponds to the best-established approach to overcome this limitation [Montaldo *et al.* (2009)]. The interest of such technique resides in its ability to reproduce a synthetic focus on the full image in transmission, as it is done in synthetic transmit aperture [Jensen *et al.* (2006)a].

The quality of the coherent summation was first assessed from static targets on numerical simulation and/or in vitro physical phantoms [Cheng and Lu (2006), Garcia *et al.* (2013), Montaldo *et al.* (2009)]. The conventional scheme proposed in the corresponding papers involved a set of steered PW transmitted with an increment angle $d\alpha$ of 1°. For instance, conventional PW imaging techniques based on the transmission of 5 steered PW classically involves angles of values (-2°,-1°,0°,1°,2°). From this framework, it has been observed in most of the studies that the image quality monotonically increases with the number of transmitted steered PW up to a convergence state [Garcia *et al.* (2013), Montaldo *et al.* (2009)].

One of the main interest of PW imaging is its capacity in imaging dynamic phenomena at high frame rates. In the case of moving targets, the perfect coherent summation is no longer achieved [Wang and Lu (2007)]. The influence of the maximum transmitted angle α_{max} and the number of steered PW on the image quality were analytically investigated in [Denarie *et al.* (2013)b]. An alternated polarity transmit scheme with motion compensation was then proposed to reduce the influence of motion on PW compounded image.

In this chapter, we propose to revisit the influence of the transmission scheme in the case of PW imaging. Since most of the new concepts introduced in this thesis are validated from static phantoms (both in simulation and from *in vitro* experiments), we focused our attention on the optimization of the transmission scheme in the particular case of non-moving object.

4.2 Methodology

In this section, we revisit the coherent summation of multiple steered PW from an analytical point of view with the aim of investigating the influence of the chosen steered angles on the synthetic acoustic field achieved in transmit.

4.2.1 Principles

We start from the explicit expression of a monochromatic PW $p_c^i(x, z, t)$ with a steering angle α_i (as the angle θ in Figure 3.1a) [Montaldo *et al.* (2009)]:

$$p_c^i(x, z, t) = p_0 \exp\left(j\left(xk_x^i + zk_z^i - \omega t\right)\right) \tag{4.1}$$

where $k_x^i = k_0 \sin\alpha_i$, $k_z^i = k_0 \cos\alpha_i$, $k_0 = 2\pi/\lambda$ (λ corresponding to the conventional wavelength) and $\omega = 2\pi f_0$. In the particular case of a set of N PW steered in a symmetric manner with a constant increment angle $d\alpha$, α_i can be reformulated as $\alpha_i = i\,d\alpha$ with $i \in [-(N-1)/2, (N-1)/2]$, leading to the following relation for small values of α_i:

$$k_x^i = \frac{2\pi}{\lambda}\sin(i\,d\alpha) \approx \frac{2\pi}{\lambda}i\,d\alpha. \tag{4.2}$$

As demonstrated in [Montaldo *et al.* (2009)], the image of a point (x_f, z_f) from compounding scheme is the same as the one obtained by illuminating the medium with a unique wave:

$$p_c(x', z', t) = \sum_{i=-(N-1)/2}^{(N-1)/2} p_0 \exp\left(j\left(x'k_x^i + z'k_z^i - \omega t\right)\right), \tag{4.3}$$

where $x' = x - x_f$ and $z' = z - z_f$ are the coordinates centered at the focal point (x_f, z_f). At the focal depth $z = z_f$, the evolution of the synthetic pressure field along the x-axis is then given by:

$$p_c(x', t) = \sum_{i=-(N-1)/2}^{(N-1)/2} p_0 \exp\left(j\left(x'k_x^i - \omega t\right)\right). \tag{4.4}$$

By using the relation given in Eq. (4.2) and the standard geometrical series relations, the above equation can be simplified as:

$$|p_c(x', t)| = |p_0| \left|\frac{\sin(k_0\,d\alpha\,x'N/2)}{\sin(k_0\,d\alpha\,x'/2)}\right| \tag{4.5}$$

The above expression allows investigating the dimension of the main lobe and the positions of the side lobes in the monochromatic case at the center frequency and at the focal depth. Indeed, Eq. (4.5) vanishes for

$$x' = \frac{\lambda}{N\,d\alpha}l, \quad l \in Z^* \tag{4.6}$$

The main lobe width is proportional to the distance between the first zeros of the transverse pressure function (*i.e.* the distance between $l = -1$ and 1 in Eq.(4.6)), thus the width W of the main lobe corresponding to a coherent summation of N steered PW

$(N > 1)$ is in the order of:

$$W = 2\,\frac{\lambda}{Nd\alpha} = \frac{N-1}{N}\,\frac{\lambda}{\alpha_{max}} \approx \frac{\lambda}{\alpha_{max}} \tag{4.7}$$

where $\alpha_{max} = \frac{N-1}{2}d\alpha$, represents the maximum transmitted angle. Thus the increment
angle $d\alpha$ can be expressed as :

$$d\alpha = \frac{2\alpha_{max}}{N-1} \tag{4.8}$$

Eq.(4.7) shows that the width of the main lobe, which is directly linked to the lateral
resolution of the system, is uniquely fixed by two parameters: the wavelength of the
probe and the maximum transmitted angle α_{max}. Thus, by maintaining the maximum
angle α_{max} for varying number of steered PW involved in transmission, the corresponding
reconstructed images will share the same resolution.

4.2.2 The dichotomous transmission scheme

For conventional imaging, the focused beam profile can be expressed as [Denarie *et al.*
(2013)b]:

$$|p(x', z_f, t)| = |p_0|\,\left|\frac{\sin\left(k_0\,x'\,L/(2z_f)\right)}{\sin\left(k_0\,x'\,\Delta\,x/(2z_f)\right)}\right| \tag{4.9}$$

where L is the size of the aperture, $\Delta\,x$ is the pitch of the linear array. To achieve the
equality of Eq. (4.5) and Eq. (4.9), the number of steered PW N and the angle increment
$d\alpha$ have to satisfy the following relation:

$$Nd\,\alpha = \frac{L}{z_f} \tag{4.10}$$

By replacing $d\alpha$ in the above expression using Eq.(4.8), the maximum transmitted
angle α_{max} can be reformulated as

$$\alpha_{max} = \frac{N-1}{N}\,\frac{L}{2z_f} \approx \frac{L}{2z_f} \tag{4.11}$$

This last expression shows that the maximum transmitted angle α_{max} can be deter-
mined by the aperture size L and a chosen focused depth z_f. Based on Eq. (4.7) and (4.11),
there can be several options to choose the angles in between, but the most straightforward
is to distribute them equally in between the extreme values. We named this approach the
dichotomous scheme thereafter and the corresponding algorithm is described below.

1. We first fix the maximum depth z_f that we want to image.

2. Thanks to Eq. (4.11), we then compute the optimal maximum angle α_{max} that we
   use whatever the number of steered PW involved in compounding.

3. The values of the angles of the steered PW used in transmission are then equally distributed from $-\alpha_{max}$ to α_{max}.

4.3 Experiments

4.3.1 Simulation

Based on the previous analytical study, we proposed to quantify from simulation the influence of the increment angle $d\alpha$ together with the number of steered PW used in compounding on the resolution of the transmitted field. To this aim, simulations of the synthetic acoustic field (acoustic field from each transmit summed with spatial coherent compounding) were performed to assess the system quality in transmission. A standard linear-array probe of 128 elements with 0.19-mm pitch, 13-mm height, a center frequency of 5-MHz (100% bandwidth), and a 23-mm elevation focus was implemented using Field II [Jensen and Svendsen (1992)]. The sampling frequency was set to 100 MHz. The acoustic field transmitted by each steered PW was also calculated using Field II. Because this part of the study only focuses on the transmission side, it is worth noting that its conclusions should benefit to any reconstruction methods based on PW imaging. This point will be investigated in the next section.

Influence of the increment angle $d\alpha$

Figure 4.1 shows the transmitted synthetic pressure field obtained in the particular case of 3 steered PW with values of steered angles equal to $(-\alpha_s, 0, \alpha_s)$, α_s varying from 1° to 21°. In the particular case of 3 steered PW, α_s corresponds both to the increment angle $d\alpha$ and the maximum transmitted angle α_{max}. $\alpha_s = 1°$ corresponds to the conventional scheme used in [Cheng and Lu (2006), Garcia *et al.* (2013), Montaldo *et al.* (2009)]. Coherent summation was performed at 30-mm depth and for two different lateral positions of the field of view: at the center (left-hand side of Figure 4.1) and close to the edge of the probe (right-hand side of Figure 4.1). The first row of Figure 4.1 displays the lateral resolution, measured as the width of the main lobe at -6 dB, at 30-mm depth and for increasing values of α_s. The second row of Figure 4.1 shows the normalized synthetic pressure distribution along the lateral position at 30-mm for α_s equals to 1°, 5°, 10° and 15°, while the last row displays these pressure distributions in the entire space.

From Figure 4.1a and 4.1b, it can be seen that the lateral resolution improves with the increase of the value of the steered angle, which is in accordance with Eq. (4.7). For a steered angle greater or equal to 10°, a lateral resolution smaller than 1-mm is obtained. However, large values of α_s increase the magnitude of the grating lobes near the probe edges (Figure 4.1d) because of the large $d\alpha$, which results in a poor resolution after 12° (Figure 4.1b) and thus produced undesirable border effects in terms of imaging system. Therefore, an optimal steered angle α_{opt} around 10° appears to be a good trade-off between a good resolution (lateral resolution around 0.8-mm) and a small magnitude of the grating

lobe. This value, fixed thanks to the above analytical study from a given probe settings, was used in the rest of the experiments.

(a) (b) (c) (d) (e) (f)
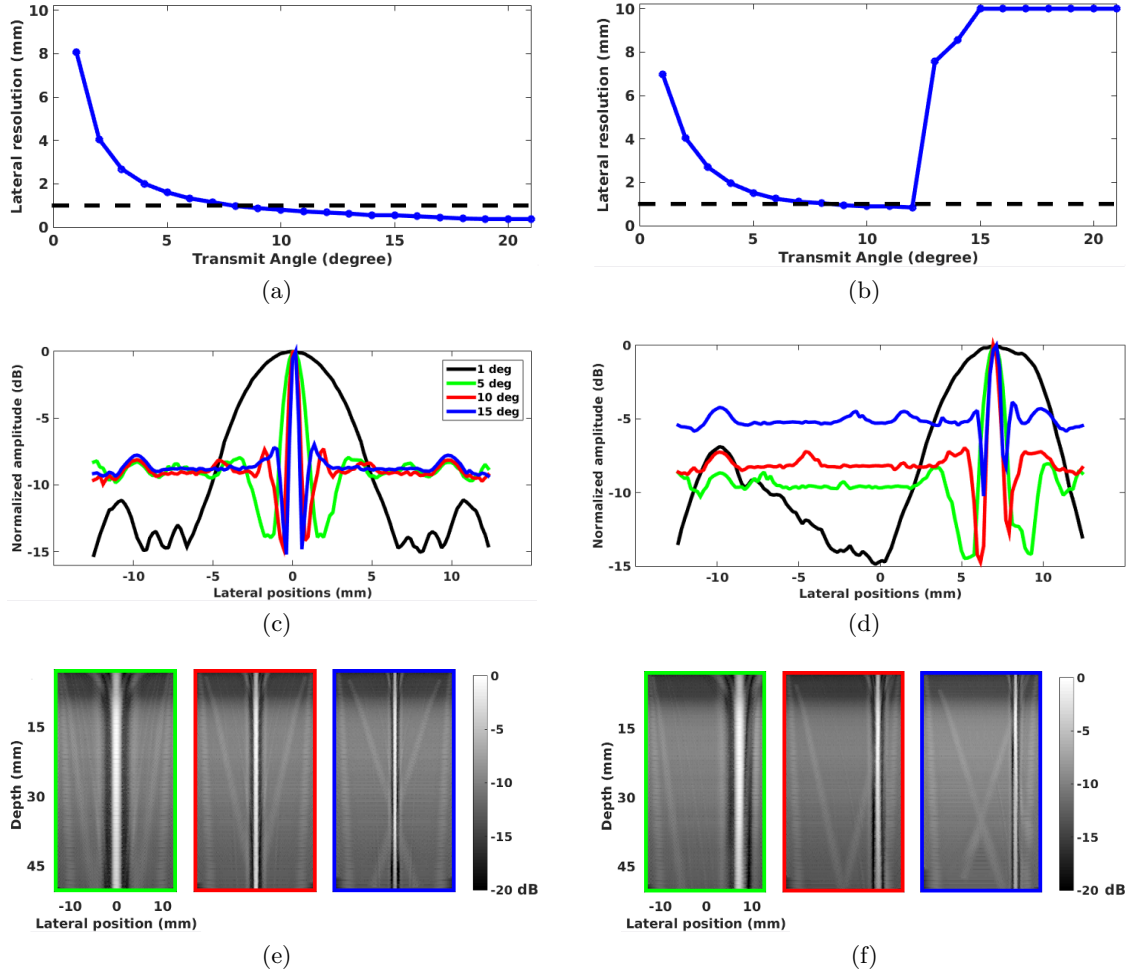
Figure 4.1: Effect of the value of the steered angle α_s on the lateral resolution using synthetic acoustic field. Each pressure is compounded with 3 steered PW $(-\alpha_s, 0, \alpha_s)$ at 30-mm depth on the central axis (left column) and on the edge of the probe (right column). (a)-(b) Lateral resolution as a function of α_s. The black dashed line represents the limit of lateral resolution at 1 mm. (c)-(d) Normalized synthetic pressure computed along lateral positions for different values of α_s (1°, 5°, 10°, 15°). (e)-(f) 2-D normalized synthetic pressure distribution obtained for the different configurations of α_s with 5°, 10° and 15°.

Influence of the number of steered PW

Figure 4.2 displays the evolution of the resolution with respect to the number of steered PW used in transmission computed from simulation of the synthetic acoustic field. The lateral resolution was measured at 30-mm depth in the center of the image. In this experiment, the conventional and the dichotomous scheme were compared. For the regular scheme, the angle increment is fixed to 1°, implying thus that the maximum angle increases
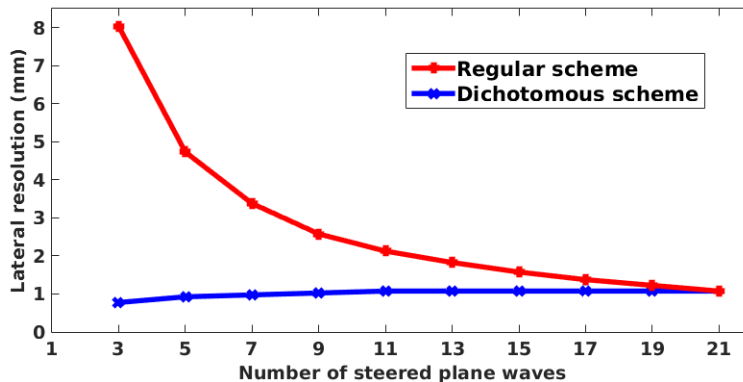
Figure 4.2: Influence of the number of transmitted steered PW on the lateral resolution for the conventional and the dichotomous scheme.

with the number of steered PW. For the second approach, we used the optimal value $\alpha_s = 10°$ derived in the particular case of 3 steered PW and then increased the number of steered PW uniformly from $-\alpha_s$ to α_s. For instance, in the particular case of 5 steered PW, the values of the involved steered angles are thus equal to $(-\alpha_s, -\alpha_s/2, 0, \alpha_s/2, \alpha_s)$, *i.e.* $(-10°, -5°, 0°, 5°, 10°)$.

From Figure 4.2, it can be observed that the lateral resolution improves with the increase of the number of steered PW in the case of the conventional approach (from 8-mm to 1-mm), which is in accordance with Eq. (4.7). Indeed, for a constant value of $d\alpha$, the width of the main lobe decreases for increasing values of the number of steered PW, which results in an improvement of the lateral resolution. On the opposite, the dichotomous transmission scheme yields a quasi constant resolution around 1-mm whatever the number of the involved steered PW, which illustrates the strong interest of such approach. Moreover, the small decrease of the lateral resolution after the compounding of 3 steered PW can also be explained from Eq. (4.7). Indeed, it can be analytically observed that the width of the main lobe slightly increases with the number of steered PW up to a convergence value equals to λ/α_s, which is in accordance with the results observed in Figure 4.2.

Figure 4.3 gives the normalized synthetic pressures computed along the lateral position at 30-mm depth using the two transmission schemes with increasing number of steered PW. For both methods, it can be seen that the grating lobes decrease with the number of steered PW, which should have an impact on the contrast. For the dichotomous scheme, this figure also reveals the stable behavior of the main lobe (lateral resolution), the increase of the transmitted steered PW having mostly an impact on the reduction of the grating lobes effects.

4.3.2 *In vitro* experiments

In this section, we evaluated the performance of the dichotomous and the conventional transmission schemes associated with the current state-of-the-art reconstructed methods
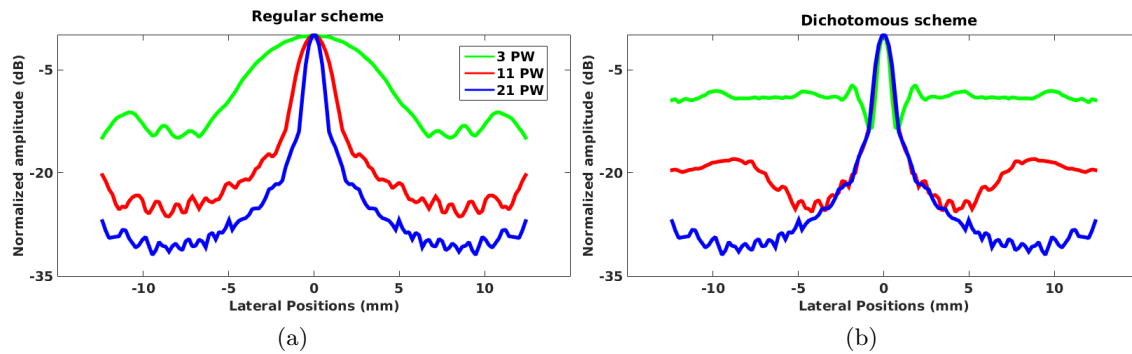
Figure 4.3: Normalized synthetic pressure computed along the lateral position at 30-mm depth in the center of the image with varying numbers of steered PW (3, 11 and 21) using (a) the regular approach (*e.g.* 3 steered PW: $\{-1°, 0°,1°\}$) and (b) the proposed dichotomous scheme (*e.g.* 3 steered PW: $\{-10°, 0°, 10°\}$).

for PW imaging, *i.e.* the methods of Lu [Lu (1997)], Garcia [Garcia *et al.* (2013)] and Montaldo [Montaldo *et al.* (2009)]. The image quality was assessed experimentally using an ultrasound phantom (CIRS model: 054GS) [CIR (2013)]. Figure 4.4 displays the schematic diagram of the corresponding phantom along with the two imaging planes involved in this experiment. A standard linear array probe (128 elements, center frequency of 7.8 MHz, transmitted frequency of 5 MHz, Verasonics - L12-5-50 mm) with the same characteristics as the one used in Section 4.3.1 was interfaced with a Verasonics system to image the phantom. The imaging depth was set to 50 mm. The number of transmitted steered PW varied from 1 to 21, providing a frame rate between 15400 and 733 fps, respectively. No apodization in transmission and reception was used for the entire acquisitions. The received raw-data were processed using the three state-of-the-art techniques for PW imaging described in Section 3.1.1. The two different transmission schemes presented in Section 4.3.1 were investigated. For the regular scheme, the angle increment is fixed to 1° while for the dichotomous scheme, the optimal steered angle α_s was set to 10°. The beamformed RF data were Hilbert transformed and normalized to get the envelope images. The corresponding images were then gamma-compressed using $\gamma = 0.3$ as in [Garcia *et al.* (2013)] and finally converted to 8-bit grayscale to get the B-mode images.

Lateral resolution

Lateral resolution was first investigated from the imaging plane n°2 given in Figure 4.4 (acquisition centered on the 0.1-mm nylon monofilament targets). The corresponding values were measured as the width at -6 dB of the Point Spread Function (PSF) corresponding to the two points present at 20 mm and 40 mm in the image. Figure 4.5 investigates the improvement of the lateral resolution with the number of steered PW for the different reconstruction techniques and for different depths. First, it can be seen that the three methods produce similar image quality both for a single PW (Figure 4.5a) or using 21 steered PW with coherent compounding (Figure 4.5b). These observations are
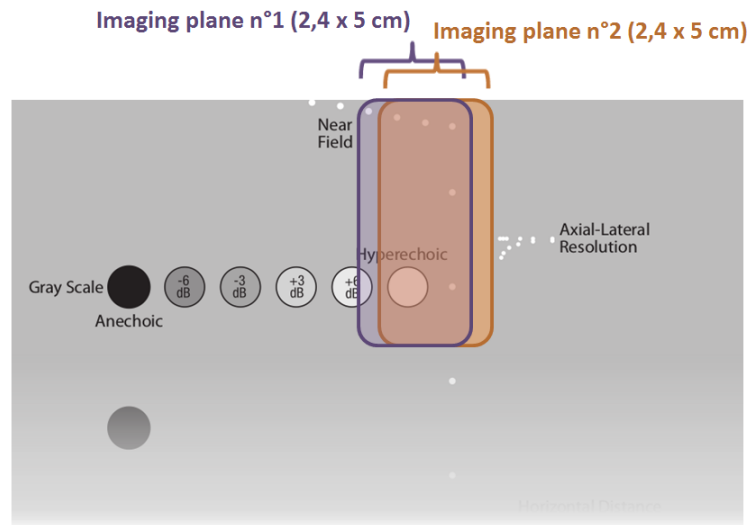
Figure 4.4: Schematic diagram of the CIRS tissue-mimicking phantom (model: 054GS) with the corresponding imaging planes used in the experiments

confirmed by the two graphs provided in Figure 4.5c which display the evolution of the lateral resolutions measured at 20 and 40 mm with respect to the number of steered PW. Indeed, the lateral resolution derived from the dichotomous scheme improves quickly for 3 steered PW and then tends to stabilize to the optimal value whatever the reconstructed method, *i.e.* around 0.9-mm at 20-mm depth and between 0.6 and 0.8-mm at 40-mm depth, which is in coherence with what has been previously observed from simulations. The dichotomous scheme reaches the optimal lateral resolution values for the transmission of only 3 steered PW (frame rate of 5133 fps), while the conventional scheme (dashed lines) reaches the same values after the transmission of 21 steered PW (frame rate of 733 fps).

Image contrast

The image contrast was then investigated from the imaging plane n°1 given in Figure 4.4 (acquisition centered on the hyperechoic target). Figure 4.6 shows the improvement of the image contrast with respect to the number of steered PW for the three reconstruction methods. As for the lateral resolution case, the use of the dichotomous scheme in transmission (solid lines) allows a significant improvement of the image quality compared to the conventional approach (dashed lines) at a constant frame rate. Indeed, the dichotomous scheme reaches the optimal CR values for the transmission of only 5 steered PW (frame rate of 3080 fps), while the conventional approach reaches the same values after the transmission of 21 steered PW (frame rate of 733 fps). Moreover, it is also interesting to note that the reached optimal CR scores are close whatever the method, varying from 6 to 6.7-dB.
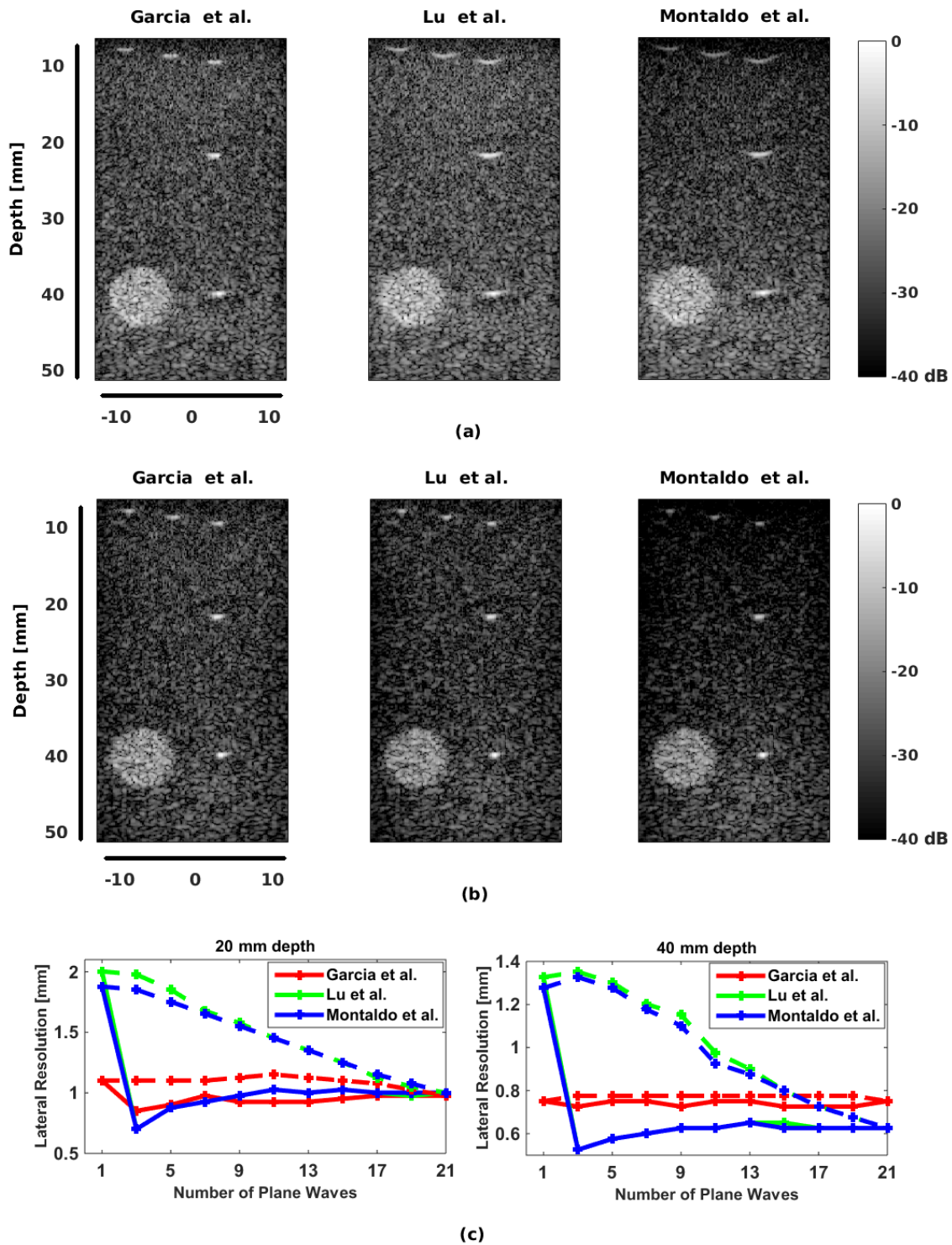
Figure 4.5: B-mode images of a CIRS phantom (model: 054GS) reconstructed from the three reconstructed methods using (a) 1-PW and (b) 21 steered PW with coherent compounding. (c) Lateral resolution measurements as a function of the number of steered PW. The solid lines correspond the proposed dichotomous transmission scheme while the dashed lines correspond to the regular scheme.
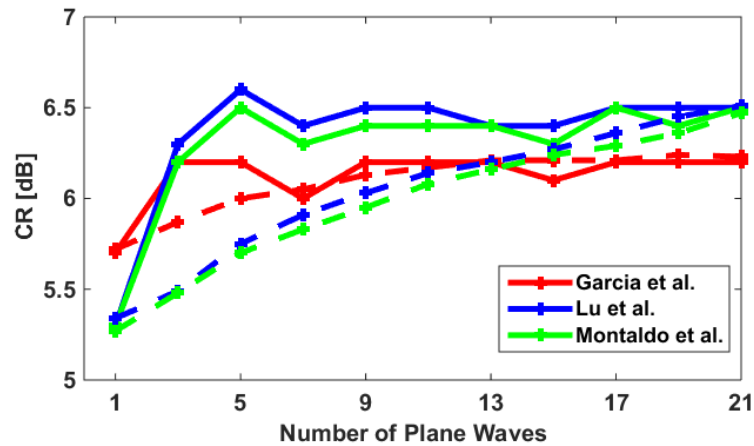
Figure 4.6: Contrast ratio CR as a function of the number of steered PW for the three reconstructed methods. The solid lines correspond the proposed dichotomous transmission scheme while the dashed lines correspond to the regular scheme.

4.4 Summary

In this chapter, we revisited the influence of the transmission scheme involved in PW imaging with coherent compounding. In particular, we investigated the importance of the choice of the steered angles on the quality of the reconstructed image in terms of resolution and contrast. Based on the analytical analysis of the synthetic pressure, we showed that the use of a dichotomous transmission scheme improves significantly the quality of the reconstructed B-mode images at constant frame rates. Experimental comparisons with the conventional transmission scheme reveal the potential of the dichotomous scheme in dividing by a factor of four the number of steered PW needed to reconstruct same quality of images, the optimal number of transmitted waves varying from 21 steered PW using the conventional approach (frame rate of 733 fps) to 5 steered PW with the dichotomous solution (frame rate of 3080 fps).

Chapter 5

Ultrasound Fourier Slice Beamforming

In this chapter, an alternative Fourier-based method: Ultrasound Fourier Slice Beamforming (UFSB) is proposed. UFSB is based on the Fourier slice theorem. As in other standard image modalities (*e.g.* Computed Tomography), the principle is to sample the object spectrum radially. Here, this is done using steered PW in reception.

5.1 Introduction

The principle of the existing ultrafast Fourier-based methods introduced in Section 3.1.1 can be summarized as follows. One PW is first emitted. Backscattered echoes are then measured (Figure 5.1a). 2D-Fourier transform is applied on the received RF raw-data (Figure 5.1b). Finally, a remapping function is used to project the Fourier transform of the received echoes to the k-space corresponding to the Fourier transform of the object function (Figure 5.1c). By taking the inverse 2D Fourier transform, the final ultrasound image is then reconstructed (Figure 5.1d). One important shared property of the previous Fourier-based techniques is that the Fourier spectrum of the object is sampled along the k_z axis direction with a lateral step proportional to the inverse of the pitch (distance between two consecutive active elements).

The Fourier slice theorem, which is based on the collection of projections of the object function from many different directions, has been widely used in Computed Tomography (CT) [Hsieh and (Society) (2009)]. The theorem states that the one dimensional Fourier transform of a projection of an image provides a slice of the 2D Fourier transform of the image. Performing projections along different angles thus allows to radially sample the full spectrum of the image. By doing the inverse Fourier transform of the image spectrum, the
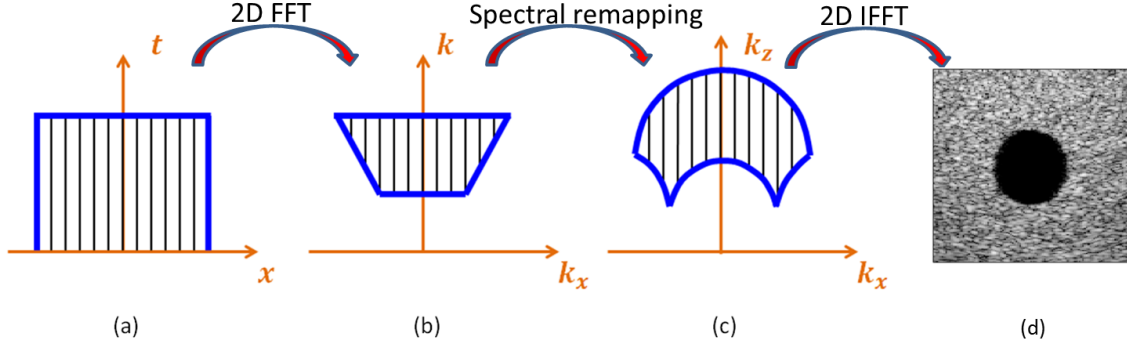
Figure 5.1: Reconstruction procedure for conventional Fourier-based method. (a) the received raw-data in (x, t) space; (b) the 2D Fourier transform of the raw-data; (c) the remapped object spectrum; (d) the reconstructed image.

image is reconstructed. In CT systems, a beam of X-ray is created to pass through the tissue. A detector placed on the opposite side measures the corresponding projection along one direction. By rotating the emitter and detector for several angles, the full k-space of the image can be recovered. Unlike CT, ultrasound systems use the same transducer array to both transmit and receive the ultrasound wave. The use of the Fourier slice imaging technique in ultrasound is thus not straightforward and an adaptation of the projection reconstruction scheme to the specificity of ultrasound image formation is thus required.

The main results in this chapter were presented at the IEEE International Ultrasonic Symposium in 2014 [Bernard *et al.* (2014)].

5.2   Theory

In this section, an alternative Fourier-based imaging method (UFSB) is developed based on the Fourier Slice Theorem. We start from the steered PW modeling and combine the Fourier slice theorem with the ultrasound image formation process.

5.2.1   UFSB: single plane wave imaging

Steered plane wave modeling

Ultrasound Fourier slice imaging is based on the use of steered PW both in emission and in reception. Let $\phi_{\mathbf{n}}(\mathbf{x}, t)$ be a plane-wave steered in the direction defined by $\mathbf{n}$. The scalar pressure field of this plane-wave can be defined as:

$$\phi_{\mathbf{n}}(\mathbf{x}, t) = \phi(ct - \mathbf{n} \cdot \mathbf{x}) \tag{5.1}$$

where $\mathbf{x} = (x, z)$ is a point in the medium with x is the lateral axis and z is the axial axis and ϕ represents the wave shape, which can thus be rewritten as:

$$\phi_{\mathbf{n}}(\mathbf{x}, t) = \phi(ct) * \delta(ct - \mathbf{n} \cdot \mathbf{x}) = \phi * \delta(ct - \mathbf{n} \cdot \mathbf{x}) \tag{5.2}$$

The wave front of a propagating field corresponds to the location, at a particular time instant t_0 , where the field value is the same, *i.e.* $\mathbf{x}$ verifying $\phi_{\mathbf{n}}(\mathbf{x}, t_0) = cst$. In the particular case of steered plane-wave, thanks to Eq. (5.2), the corresponding wave front can be easily defined as the location where $\delta(ct_0 - \mathbf{n} \cdot \mathbf{x}) = 0$, *i.e.* $\mathbf{n} \cdot \mathbf{x} = ct_0$ which corresponds to a line perpendicular to the direction given by $\mathbf{n}$ and passing through the point $ct_0\mathbf{n}$, as illustrated in Figure 5.2.
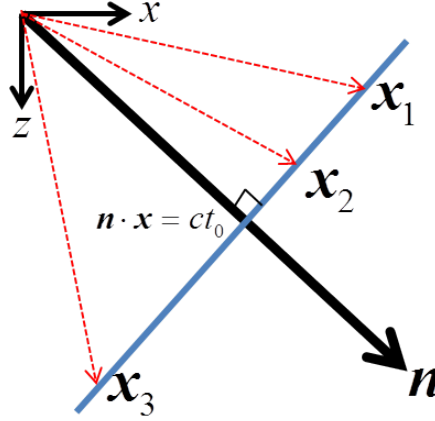
Figure 5.2: Illustration of a wavefront of a steered PW with direction $\mathbf{n}$. All the $\mathbf{x}$ in the blue line has the same wavefront.

Ultrasound image formation

Here we focus on finding a relationship between the object spectrum and the received raw-data using a horizontal PW in transmission and steered PW in reception, as illustrated in Figure 5.3. In particular, a linear array is excited to generate a single PW with direction $\mathbf{n_e}$ to insonify the medium and is also used to receive the backscattered echoes coherently as a steered PW in the direction $\mathbf{n_r}$. The summation of the output signal of all the elements in such a system can be modeled as follows:

$$
\begin{aligned}
s(t) &= \sum_{Z^*} s(x_i, t) \\
&\approx \int_D m(\mathbf{x}) \cdot \phi_{\mathbf{n_e}}(\mathbf{x}) * \phi_{\mathbf{n_r}}(\mathbf{x}) \mathrm{d}\, x \\
&\approx \int_D m(\mathbf{x}) \cdot \phi_{er} * \delta\left(ct - \mathbf{n_{er}} \cdot \mathbf{x}\right) \mathrm{d}\, x
\end{aligned}
\tag{5.3}
$$

where Z^* corresponds to the restriction of element positions of the probe. $*$ represents the temporal convolution product and $\mathbf{n_{er}} = \mathbf{n_e} + \mathbf{n_r}$. ϕ_{er} corresponds to the convolution between the impulse responses of the emitted field ϕ_e and the received field ϕ_r. D corresponds to the transducer width and $m(\cdot)$ is a function that characterizes both the spatial distribution and the backscattered amplitude of the different scatterers present in
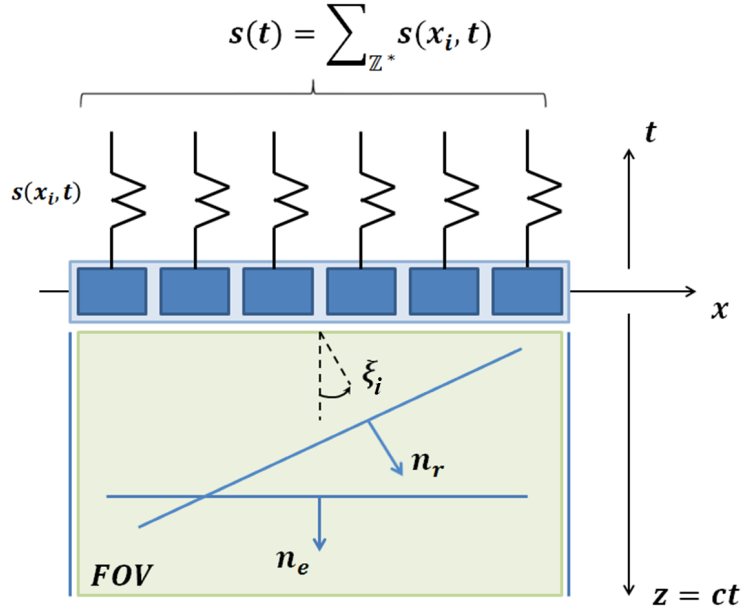
Figure 5.3: Illustration of the image formation introduced in UFSB theory

the insonified medium. Typically, $m(\cdot)$ can be defined as:

$$m(\mathbf{x}) = \sum_{\{i,j\}\in FOV} a(i,j)\delta(x-i)\delta(z-j) \tag{5.4}$$

where $a(i,j)$ is the reflection coefficient of the scatterer positioned at (i,j), FOV corresponds to the area insonified by the transmitted wave.

Ultrasound Fourier Slice Beamforming

The temporal Fourier transform $\mathcal{F}_t(\cdot)$ of signal $s(t)$ leads to the following relation:

$$F_t\left(s(t)\right) = \int_{-\infty}^{+\infty}\left[\int_D m(\mathbf{x})\cdot\phi_{er} \ *\delta\left(ct-\mathbf{n_{er}}\cdot\mathbf{x}\right)\mathrm{d}\,x\right]e^{-j2\pi ft}\,\mathrm{d}t \tag{5.5}$$

Given the fundamental relations $z = ct$ and $k = \frac{2\pi f}{c}$, where z and k corresponds to the spatial distance and the wavenumber defined in the direction given by $\mathbf{n_{er}}$, respectively, Eq. (5.5) can be rewritten as:

$$F_t\left(s(t)\right) = \frac{1}{c} \int_{-\infty}^{+\infty} \left[\int_D m(\mathbf{x}) \cdot \phi_{er} \; * \delta\left(z - \mathbf{n_{er}} \cdot \mathbf{x}\right) \mathrm{d}\,x \right] e^{-jkz} \,\mathrm{d}z$$

$$= \frac{1}{c} \int_D \left[\int_{-\infty}^{+\infty} m(\mathbf{x}) \cdot \phi_{er} \; * \delta\left(z - \mathbf{n_{er}} \cdot \mathbf{x}\right) e^{-jkz} \,\mathrm{d}z \right] \mathrm{d}\,x$$

$$= \frac{1}{c} \int_D \left[\int_{-\infty}^{+\infty} m(\mathbf{x}) \cdot \phi_{er} \; e^{-jk(\mathbf{n_{er}}\cdot\mathbf{x})} \,\mathrm{d}z \right] \mathrm{d}\,x$$

$$= \frac{1}{c} \iint_{FOV} m(\mathbf{x}) \cdot \phi_{er} \; e^{-jk(\mathbf{n_{er}}\cdot\mathbf{x})} \,\mathrm{d}\,x \; \mathrm{d}z \tag{5.6}$$

Since $m(\mathbf{x})$ is zero out of the field of view (FOV), we use FOV to represent the limit of integration in the last step of Eq. (5.6). In the special case where $\mathbf{n_e} = (0,1)^T$ and $\mathbf{n_r} = (\sin(\xi_i), \cos(\xi_i))^T$, Eq. (5.6) can be rewritten as:

$$F_t\left(s(t)\right) = \frac{1}{c} \iint_{FOV} m(\mathbf{x}) \cdot \phi_{er} \; e^{-jk(\sin(\xi_i)x + (1+\cos(\xi_i)z))} \,\mathrm{d}\,x \,\mathrm{d}z,$$

$$= \frac{1}{c} \iint_{FOV} m(\mathbf{x}) \cdot \phi_{er} \; e^{-j(k_x x + k_z z)} \,\mathrm{d}\,x \,\mathrm{d}z,$$

$$= \frac{1}{c} \, F_{2D}\left[m(\mathbf{x}) \cdot \phi_{er} \right](k_x, k_z) \tag{5.7}$$

where F_{2D} is the 2D Fourier transform operator. According to the Fourier slice theorem, Eq. (5.7) can be interpreted as the $2D$ spatial Fourier transform of the image $(m \cdot \phi_{er})(\cdot)$ restricted to the line of direction $\mathbf{n_{er}}$, with the following fundamental relations:

$$\begin{cases} k_x = k\,\sin(\xi_i) \\ k_z = k\,(1+\cos(\xi_i)) \end{cases} \tag{5.8}$$

and

$$\begin{cases} k = \frac{k_x^2 + k_z^2}{2\,k_z} \\ \xi_i = \arctan\left(\frac{k_x}{k_z - k}\right) = \arctan\left(\frac{2\,k_x\,k_z}{k_z^2 - k_x^2}\right) \end{cases} \tag{5.9}$$

As a consequence, in the particular case where the emitted field is a PW perpendicular to the probe and the received field is supposed to be a steered PW with angle ξ_i, Eq. (5.6)-(5.9) show that the temporal Fourier transform of the received signal is equal to a radial line of angle $\theta_i = f(\xi_i)$ (with $f(\cdot) = \arctan(\sin(\cdot)/(1+\cos(\cdot)))$) in the corresponding k-space domain. By simply playing with different delay strategies applied on the received signals, we are thus able, for only one emitted PW, to radially and densely recover the Fourier space of the object and thus reconstruct an ultrasound image with high frame rate.

The acquisition scheme corresponding to the proposed approach is summarized in Figure 5.4.
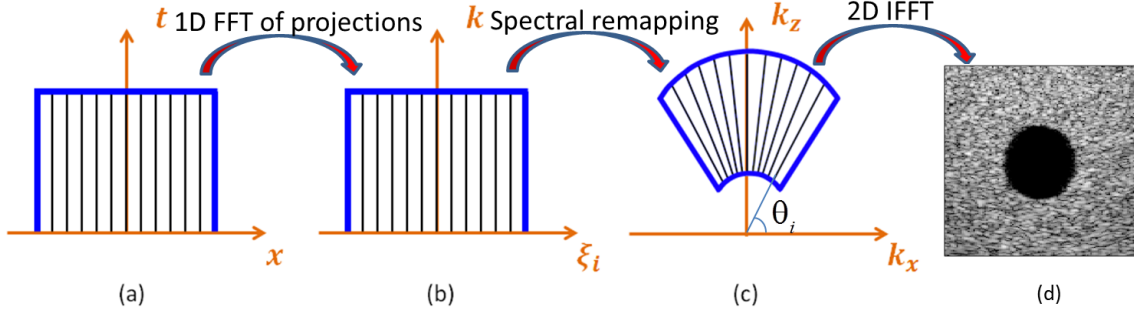
Figure 5.4: Reconstruction procedure with the proposed method. (a) the received raw-data in (x, t) space; (b) the 1D Fourier transform of all the projections of the raw-data at different angles ξ_i; (c) the remapped object spectrum; (d) the reconstructed image.

5.2.2 UFSB: steered plane wave with compounding scheme

It has been shown in [Lu (1997), Montaldo *et al.* (2009), Garcia *et al.* (2013)] that the image quality can be improved by coherently compounding the images obtained from several steered PW. To be able to perform coherent PW compounding with our method, it must be ensured that the UFSB technique can be adapted to a steered PW in transmission as well. For a steered PW with angle φ_j in transmission, which means the corresponding direction $\mathbf{n_e} = (\sin(\varphi_j), \cos(\varphi_j))^T$, the following relations can be easily derived:

$$\begin{cases} k_x = k\,(\sin(\varphi_j) + \sin(\xi_i)) \\ k_z = k\,(\cos(\varphi_j) + \cos(\xi_i)) \end{cases} \tag{5.10}$$

and

$$\begin{cases} k = \dfrac{k_x^2 + k_z^2}{2\,(k_x \sin(\varphi_j) + k_z \cos(\varphi_j))} \\[2ex] \xi_i = \arctan\left(\dfrac{2\,k_x\,k_z\cos(\varphi_j) + (k_x^2 - k_z^2)\sin(\varphi_j)}{2\,k_x\,k_z\sin(\varphi_j) + (k_z^2 - k_x^2)\cos(\varphi_j)}\right) \end{cases} \tag{5.11}$$

As a consequence, in the general case where the emitted field is a steered PW with angle φ_j and the received field is supposed to be a steered PW with angle ξ_i, Eq. (5.10)-(5.11) show that the temporal Fourier transform of the received signal still corresponds to a radial line of angle $\theta_i = f_{\varphi_j}(\xi_i)$ of the object spectrum (with $f_{\varphi_j}(\cdot) = \arctan((\sin(\varphi_j) + \sin(\cdot))/(\cos(\varphi_j) + \cos(\cdot)))$. Figure 5.5 illustrates the k-space sampling derived from the proposed UFSB method according to the angle of the transmitted steered PW ($\varphi_j = 0$ and $\varphi_j \neq 0$), the boundary of the different spectra being discussed in Section 5.5. Such relations not only allow the reconstruction of one image from the emission of a single steered PW but also allow the application of compounding scheme directly in the k-space

domain. Finally, the spectrum of the object function is averaged from a set of reconstructed spectra obtained from steered PW with different angles in transmission.
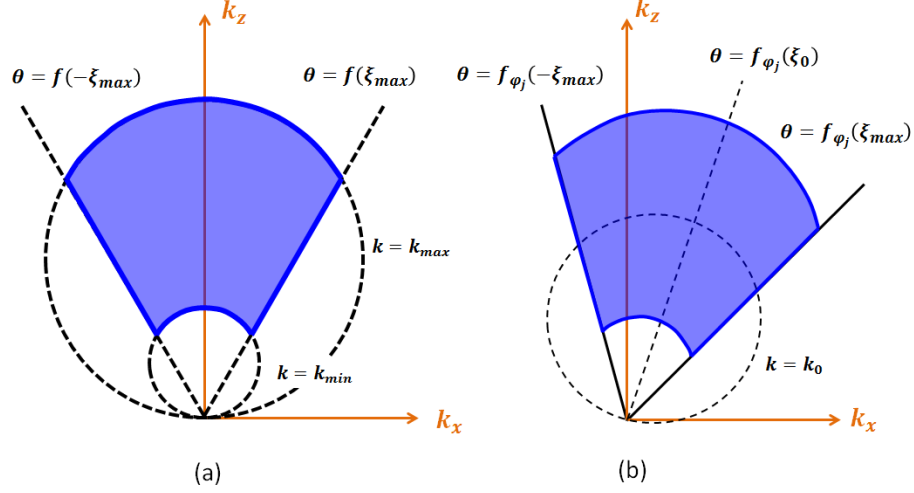
Figure 5.5: Illustration of k-space sampling derived from the UFSB method using in emission either (a) a PW perpendicular to the probe or (b) a steered PW with direction φ_j.

5.2.3 UFSB: summary and pratical implementation

The generic implementation of the procedure for the proposed UFSB scheme (based on steered PW insonifications) can be summarized as follows:

1. Transmit a PW with angle φ_j. The steering angle φ_j is obtained by delaying the firing time of each element of the array. The delay d is given by $d(x_i) = x_i \sin(\varphi_j)/c, x_i \in (-D/2, D/2)$, where x_i is the position of the array element, c is the speed of sound, and D is the aperture size. To make the system causal, an additional constant delay $dt = \left| \frac{D \sin(\varphi_j)}{2c} \right|$ is added to the delay function.

2. Receive the back-scattered echoes on each transducer element simultaneously. The 2D data set $s(x_i, t)$ is collected. Each column $s(x_i, t)$ corresponds to the received data for the transducer element at position x_i.

3. Do the 1D Fourier transform of the received data $s(x_i, t)$ over t to get the echoes in the frequency domain $S(x_i, f)$.

4. Apply delays in reception to receive steered PW with angle ξ_i. In time domain, the delays applied on the $s(x_i, t)$ should be $\tau(x_i) = x_i \sin(\xi_i)/c, x_i \in (-D/2, D/2)$ to receive a steered PW with angle ξ_i. Since there is a constant delay dt that has been added in transmission, it should be compensated in reception. The delay applied in reception is then $\tau - dt$. According to the shift property of the Fourier transform, a multiplication of complex exponential $\exp(-j2\pi f(\tau - dt))$ is applied on $S(x_i, f)$.

One radial line of the 2D Fourier spectrum of the object is obtained by performing the summation of the corresponding signals $S(x, f) \exp(-j2\pi f(\tau - dt))$ along x_i.

5. Repeat step 4 with different angle ξ_i to fully sample the object spectrum, then interpolate the radial sampled spectrum on a regular grid.

6. Apply the 2D inverse Fourier transform to reconstruct the corresponding RF image.

7. If successive steered PW are used to perform coherent compounding, repeat steps 3 to 6 for each firing and average all the reconstructed RF images to get the final compounded image.

Note: The compounding step can also be done in the Fourier domain by averaging the obtained spectrums. Which means, repeat step 3 to 5 to get the spectrums of each firing and average all the spectrums from each steered PW. Then do the 2D inverse Fourier transform on the compounded spectrum to reconstruct the final image.

5.3 Numerical simulations

In this section, numerical simulations are performed to verify and evaluate the performances (in terms of lateral resolution and image contrast) of the proposed UFSB PW imaging method. For all the tests, we use the dichotomous transmission scheme described in Section 4.2.2, the optimal steered angle α_s is set to 10°. The proposed UFSB method is compared with the current state-of-the-art ultrafast PW imaging algorithms, *i.e.* the methods of Lu *et al.* [Lu (1997)], Garcia *et al.* [Garcia *et al.* (2013)] and Montaldo *et al.* [Montaldo *et al.* (2009)]. A standard linear-array probe of 128 elements with 0.19-mm pitch, 13-mm height, a center frequency of 5-MHz (100% bandwidth), and a 23-mm elevation focus is implemented using Field II [Jensen and Svendsen (1992)]. The sampling frequency is set to 100 MHz. No apodization was used in both transmission and reception. Each reconstructed image was obtained from the following protocol: i) raw-data signals were acquired using steered PW with different transmit angles; ii) those signals were processed independently and then averaged to get the compounded RF image; iii) the corresponding envelope image was derived through a Hilbert transform and normalized; iv) the envelope image was then gamma-compressed using $\gamma = 0.3$ and finally converted to 8-bit grayscale to get the B-mode image (except for the lateral resolution study).

5.3.1 Validation of the UFSB method

We first used a numerical phantom composed of a discrete set of point scatterers to verify the proposed UFSB method with PW in transmission steered at different angles and for the compounding scheme. Figure 5.6 displays the corresponding images reconstructed from the proposed UFSB method with different transmission angles of $-10°$ (Figure 5.6a), 0° (Figure 5.6b), 10° (Figure 5.6c) and the compounded image of the 3 PW ($-10°$,0°,10°)

in transmission(Figure 5.6d), respectively. The red circles correspond to the real position of the scatterers. From the first 3 figures, it can be seen that the angle of transmitted PW has obviously a direct influence on the direction of the side lobes of the point spread function. After coherent compounding of the images from different steered PW (Figure 5.6d), the side lobe artifacts can be reduced significantly, resulting in a better contrast and resolution quality, which will be evaluated in the following section.
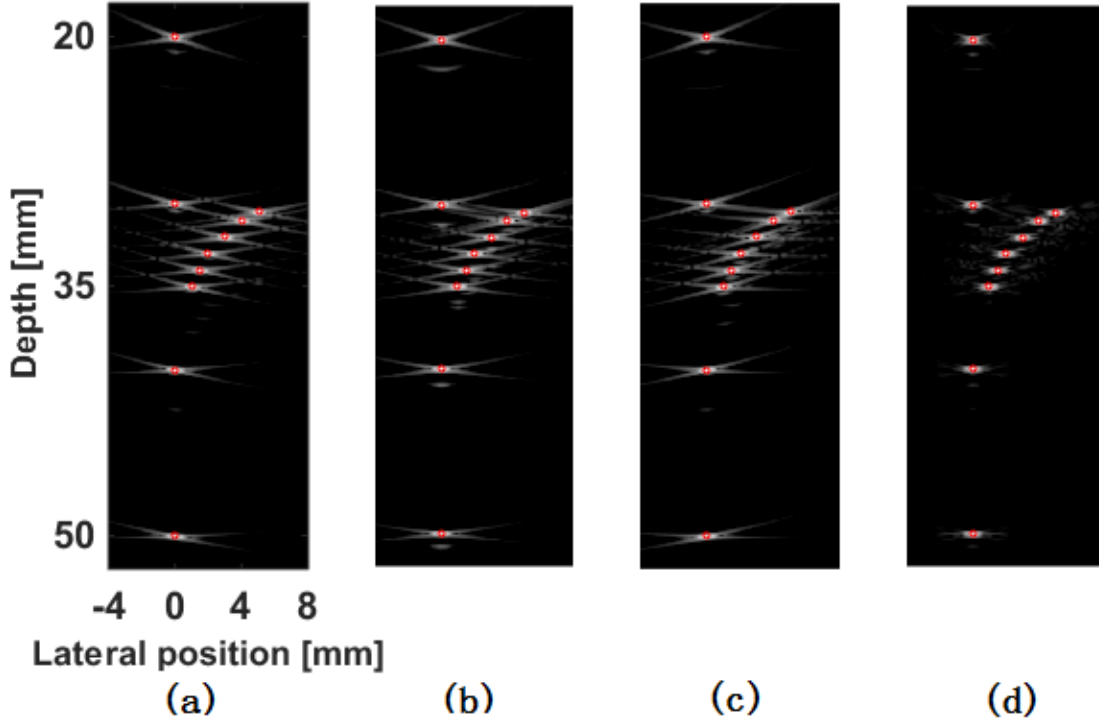
Figure 5.6: Point scatterer images reconstructed from the UFSB method using 1 PW in transmission with steered angles of (a) $-10°$ (b) $0°$ and (c) $10°$. (d) The compounded image of the previous 3 steered PW. The red circles correspond to the true position of the involved scatterers.

5.3.2 Image quality evaluation

Lateral resolution

The lateral resolution of the reconstructed images was then evaluated using the numerical phantom displayed in Figure 5.6. The corresponding values were measured as the width at -6 dB of the point spread function associated to the points located at 40-mm in the image. Figure 5.7 investigates the influence of the number of PW on the lateral resolution using the different reconstruction techniques. First, it can be seen that the 4 methods produce similar lateral resolution whatever the number of involved steered PW. In particular, it can be observed that the lateral resolution improves quickly for 3 PW and then tends to stabilize to the optimal value, *i.e.* around 0.65-mm at 40-mm depth.

It is also important to note that the lateral resolution tends to increase a little bit after the compounding of 3 PW. This behavior can be explained by the chosen dichotomous transmission scheme described in Section 4.2.2. From this figure, one can see that the lateral resolution measured in simulations for increasing number of PW is coherent with the theoretical evolution (Figure 4.2).
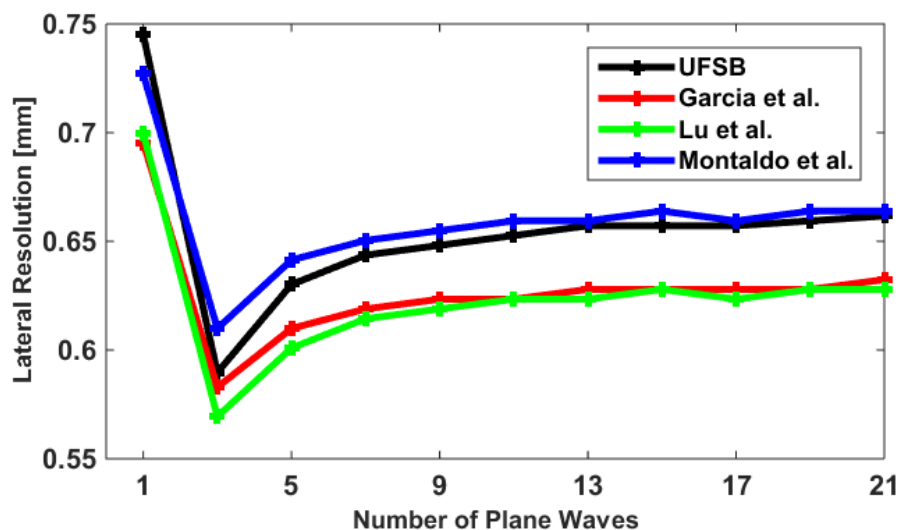
Figure 5.7: Lateral resolution as a function of the number of PW computed at 40-mm depth.

Image contrast

The quality of the reconstructed image was then investigated from the contrast ratio (CR) measurements performed through simulated phantoms (*i.e.* a homogeneous medium with high density of scatterers (20 per resolution cell) with an anechoic cyst of diameter 8-mm lying at 30-mm depth). Figure 5.8 investigates the improvement of the image contrast (CR) with the number of steered PW. First, it can be seen that the 4 methods produce similar image quality both for a single PW (Figure 5.8a) or using 21 steered PW with coherent compounding (Figure 5.8b). These observations are confirmed by the graph provided in Figure 5.8c which displays the evolution of the CR as a function of the number of steered PW. Interestingly, this result shows that among all the reconstructed methods, the proposed UFSB method provides almost the same CR value as the method of Lu, which further reveals that the UFSB technique provides very competitive contrast measurements compared to the state-of-the-art methods.

(a)

(b)

(c)
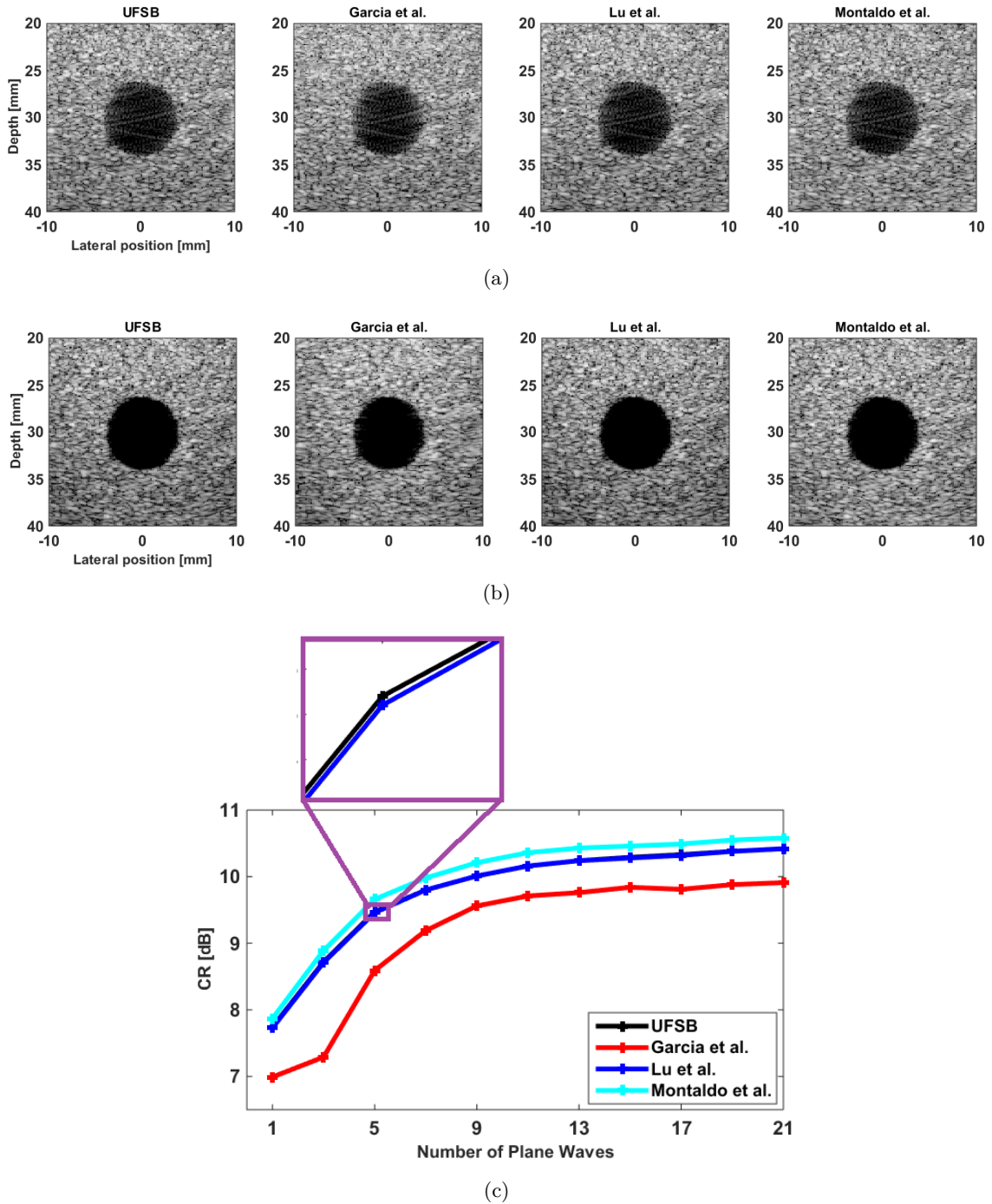
Figure 5.8: B-mode images of an anechoic cyst phantom reconstructed from the four PW imaging methods using (a) 1-PW and (b) 21-PW with coherent compounding. (c) Contrast ratio CR as a function of the number of steered PW for the 4 reconstruction methods.

5.4 *In vitro* and *in vivo* experiments

5.4.1 *In vitro* experiments

The imaging quality was also assessed experimentally using an ultrasound phantom (CIRS model: 054GS) [CIR (2013)]. Figure 5.9 displays the schematic diagram of the corresponding phantom along with the two imaging planes obtained in this experiment. A standard linear array probe (128 elements, center frequency of 7.8-MHz, transmitted frequency of 5-MHz, Verasonics - L12-5-50mm) with the same characteristics as the ones used in simulations was interfaced with a Verasonics system to image the phantom. The imaging depth was set to 50-mm. The number of transmitted PW varied from 1 to 21, providing a frame rate between 15400 and 733 fps, respectively. No apodization in transmission and reception was used for the entire acquisitions. The received raw-data were processed using the proposed UFSB technique for PW, the Fourier-based methods of Lu *et al.* [Lu (1997)] and Garcia *et al.* [Garcia *et al.* (2013)] and the spatial approach of Montaldo *et al.* [Montaldo *et al.* (2009)]. For all the tests, we use the dichotomous transmission scheme described in Section 4.2.2, the optimal steered angle α_s is set to 10°.
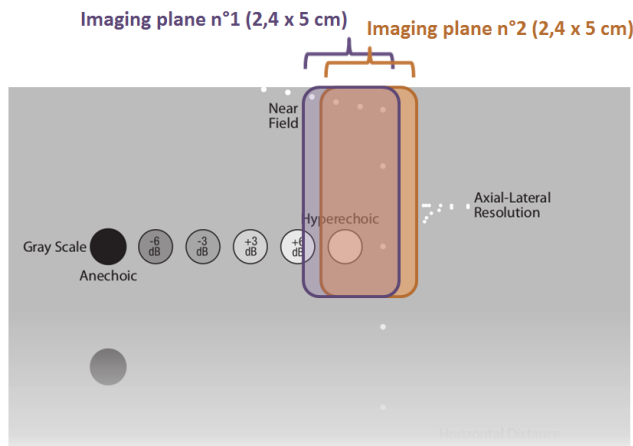
Figure 5.9: Schematic diagram of the CIRS tissue-mimicking phantom with the corresponding imaging planes used in the experiments

Lateral resolution

The lateral resolution was first investigated experimentally from the imaging plane n°2 given in Figure 5.9 (acquisition centered on the 0.1-mm nylon monofilament targets). The corresponding values were measured as the width at -6 dB of the Point Spread Function (PSF) corresponding to the two points present at 20-mm and 40-mm in the image. Figure 5.10 investigates the improvement of the lateral resolution with the number of steered PW for the different reconstructed techniques and for different depths. First, it can be seen that the 4 methods produce similar image quality both for a single PW (Figure 5.10a) or using 21 steered PW with coherent compounding (Figure 5.10b). These observations are

confirmed by the two graphs provided in Figure 5.10c which display the evolution of the lateral resolutions measured at 20 and 40-mm with respect to the number of steered PW. Using the dichotomous transmission scheme described in Section 4.2.2, it can be observed that the lateral resolution improves quickly for 3 steered PW and then tends to stabilize to the optimal value whatever the reconstructed method, *i.e.* around 0.9-mm at 20-mm depth and between 0.6 and 0.8-mm at 40-mm depth, which is in good agreement with what has been observed previously from simulations.

Image contrast

The image contrast was then investigated from the imaging plane n°1 given in Figure 5.9 (acquisition centered on the hyperechoic target). Figure 5.11 shows the improvement of the image contrast with respect to the number of steered PW for the four reconstruction methods. It can be observed that the four methods yield very close contrast ratio whatever the number of steered PW. In particular, the image contrast improves significantly for a small number of steered PW and tends to stabilize for more than 9 steered PW, which is consistent with the simulation results.

5.4.2 *In vivo* experiments of a carotid

An *in vivo* experiment was finally carried out on the carotid artery of a healthy volunteer. The transducer used in this experiment is a standard linear array probe (128 elements, center frequency of 7.8-MHz, transmitted frequency 7.8-MHz, Verasonics - L12-5-50mm) with the same characteristics as the ones used in Section 5.4.1. The imaging depth was set to 50-mm. The number of transmitted steered PW varied from 1 to 21, providing a frame rate between 15400 and 733 fps, respectively. No apodization in transmission and reception is used for the entire acquisitions. The received raw-data are processed using the three state-of-the-art techniques for PW imaging described in Section 3.1.1 (*i.e.* the methods of Lu, Montaldo and Garcia). The optimal steered angle α_s is set to 10°. The beamformed RF data are Hilbert transformed and normalized to get the envelope images. The corresponding images are then log-compressed to get the B-mode images with a 40-dB dynamic range.

Figure 5.12a and 5.12b shows the carotid images obtained with the proposed UFSB method and the state-of-the-art PW imaging methods using 1 PW in transmission and 21 steered PW in transmission with coherent compounding, respectively. As in simulations and *in vitro* experiments, these results illustrate visually the closeness of the images produced by the different methods in terms of image quality and speckle definition. In order to further investigate the influence of the four reconstruction methods, we display in Figure 5.12c the normalized absolute differences of the carotid images in Figure 5.12b. From this figure, it can be seen that the differences between UFSB and the other three methods are quite small. Particularly, the difference between UFSB and Lu is almost null for the imaging region (*i.e.* from 5-mm to 40-mm depth), which reinforces the observations
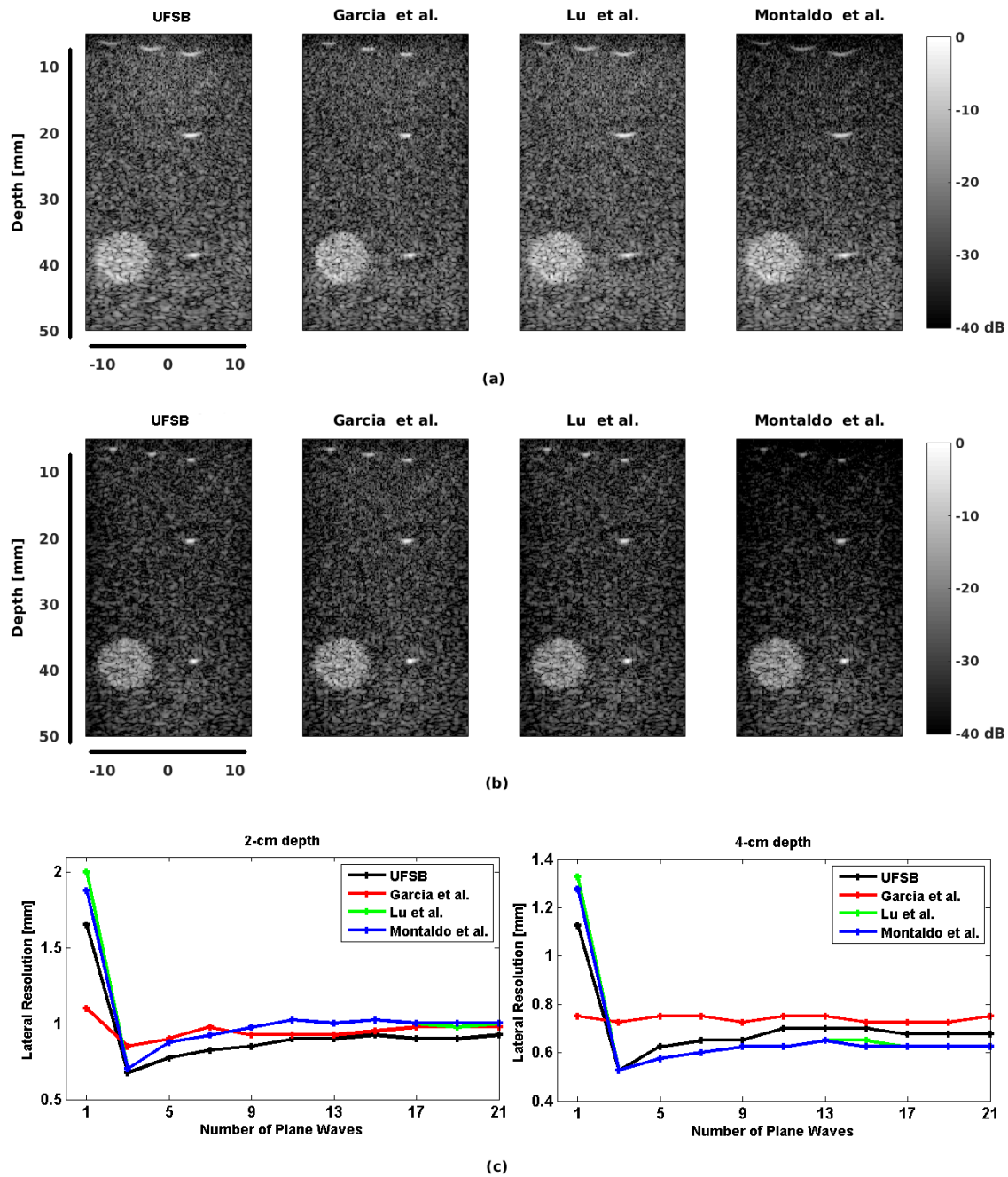
Figure 5.10: B-mode images of a CIRS phantom reconstructed from the four reconstructed methods using (a) 1 PW and (b) 21 steered PW with coherent compounding. (c) Lateral resolution measurements as a function of the number of steered PW.
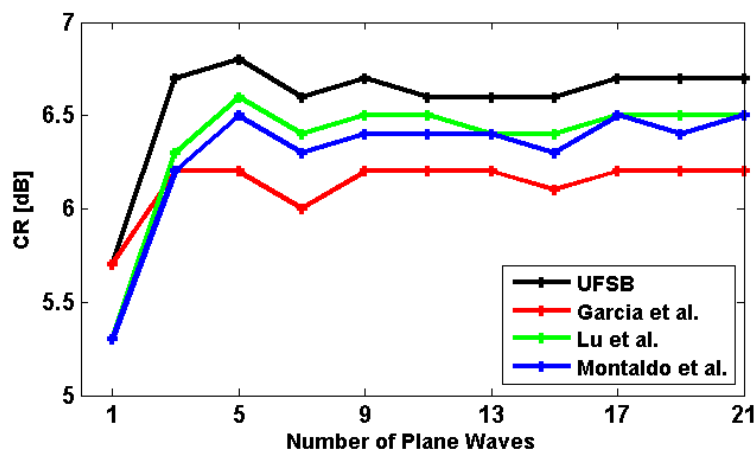
Figure 5.11: Contrast ratio CR as a function of the number of steered PW for the four PW imaging methods.

of contrast ratio (CR) for anechoic cyst in Figure 5.8 provided by the two methods that performs the closest value.

5.5 Discussion

We proposed in this chapter a new reconstruction scheme based on the Fourier slice theorem (*i.e.* UFSB). Starting from the same ultrasound modeling system as in [Lu (1997)], we showed that ultrafast imaging in ultrasound can be represented as a problem of spectrum reconstruction based on the Fourier slice theorem. As illustrated in Figure 5.4, this new technique allows recovering the Fourier spectrum of the object function radially. From the simulation and experimental results provided in Section 5.3 and Section 5.4, it can be observed that the UFSB technique produces very competitive results compared to the other existing approaches, the closest method in terms of image quality being the one proposed by Lu *et al.* It is thus of interest to evaluate the proposed UFSB framework and the two others Fourier-based approaches through the comparison of the properties of the Fourier spectrum reconstructed from each method.

The spectral content of the object function is determined by the physical limits of the ultrasound system. In our experiments, the probe consisted of transducer elements with 100% bandwith. This means that the spectral content along the k_z axis ($k_z = 2f/c$) is defined between $\{f_0/c, 3f_0/c\}$, where f_0 is the center frequency of the transducer. The lateral sampling frequency of the object function is conditioned by the pitch p of the probe, limiting the spectral content along the k_x axis to the range $\{-1/(2\,p), 1/(2\,p)\}$. As detailed in Section 5.2.1, the UFSB technique allows sampling the Fourier spectrum of the object function radially with angle $\theta_i = f_{\varphi_j}(\xi_i)$, where φ_j and ξ_i correspond to the angle of the steered PW in emission and reception, respectively. By playing with different delay strategies applied on the received signals, it is thus possible, for only one emitted PW with angle φ_j, to receive steered PW with different angles and thus radially recover the Fourier

(a)

(b)

(c)
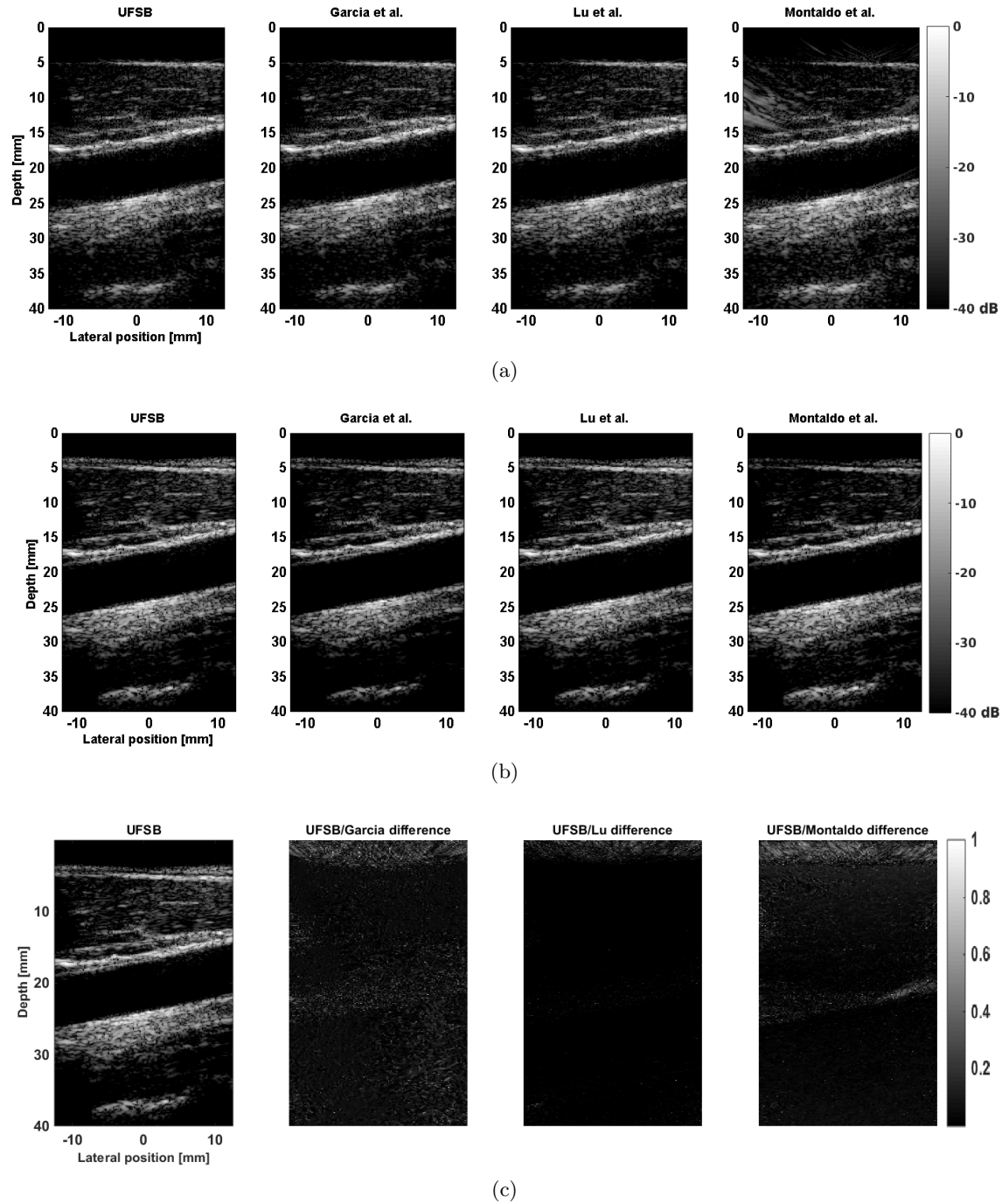
Figure 5.12: *In vivo* experiments - Carotid image reconstructed from the four PW imaging methods using (a) 1 PW and (b) 21 steered PW with coherent compounding. (c) Absolute differences of the UFSB and the other 3 reconstructed methods from the figures in (b).

space of the object. Because of the physical limits described above, we constrained for each experiment the value of θ_i in the interval $-\theta_{max} \leq \theta_i \leq \theta_{max}$, where θ_{max} is defined as

$$\theta_{max} = \arctan\left(\frac{k_{x,max}}{k_{z,min}}\right) = \arctan\left(\frac{c}{2\,p\,f_0}\right) \tag{5.12}$$

From equation (5.8) given in Section 5.2.1, it can be observed that for a fixed value of ξ_i, the UFSB k-space sampling corresponds to a line passing through the origin with an angle $\theta_i = f(\xi_i)$. Therefore the accessible range for θ_i corresponds to a cone of apex $2\,\theta_{max}$. In the same way, for a fixed value of k, the UFSB k-space sampling corresponds to a circle centered at $(k_x, k_z) = (0, k)$, with a diameter of $2\,k$. Since the two conditions must be verified simultaneously, the generic k-space sampling derived from the proposed UFSB technique corresponds to the diagrams provided in Figure 5.5

Contrary to the proposed UFSB scheme, the two others Fourier-based techniques proposed by Lu *et al.* [Lu (1997)] and Garcia *et al.* [Garcia *et al.* (2013)] sample the Fourier spectrum of the object function along the k_z axis direction with a lateral step proportional to the inverse of the pitch. In order to investigate the influence of the different Fourier sampling schemes, we display in Figure 5.13 the normalized absolute differences of the Fourier spectrum of the experimental images provided at the top row of Figure 5.10 reconstructed from the three different Fourier techniques. From this figure, it may be first seen that the difference of spectrum between Lu and Garcia methods is null for the central part of the spectrum, as it has been already observed in [Garcia *et al.* (2013)]. Moreover, this figure also reveals that the Fourier spectrum of the proposed UFSB technique is close to the one obtained from Lu *et al.*, the difference being uniformly distributed over the Fourier space with a relative difference of the order of 15% of the normalized values. Even if the Fourier sampling scheme is different, the proposed UFSB technique and the one of Lu *et al.* reconstruct close Fourier spectrum, the differences arising from the interpolation between the samples which are not distributed in the same manner. This result reinforces the experimental observations that reconstructions provided by the two methods are close and the differences between z-axis sampling and radial sampling are marginal.

Another strong interest of performing PW image reconstruction in Fourier domain concerns its lower computational complexity. As introduced in [Garcia *et al.* (2013)], the computational complexity decreases from $O(n_e n_e n_s)$ for the DAS technique to $O(n_e n_s \log(n_e n_s))$ for the method of Lu and Garcia thanks to Fourier formulation, where n_e denotes the number of elements in the transducer and n_s denotes the number of time samples. The reconstruction of one image using the UFSB method requires n_e 1-D FFTs (complexity of $O(n_e\,n_s\,log(n_s))$), one 2D FFT (complexity of $O(n_x\,n_s\,log(n_x\,n_s))$), the computation of $(n_\xi\,n_e\,n_s/2)$ multiplications for the delays applied in reception (the ratio of 2 being explained by the use of half of the spectrum) and two times the computation of $(n_x\,n_s)$ interpolated values (one for the regridding step performed in the Fourier space and one for the spatial transformation introduced in this work), where n_ξ represents the number
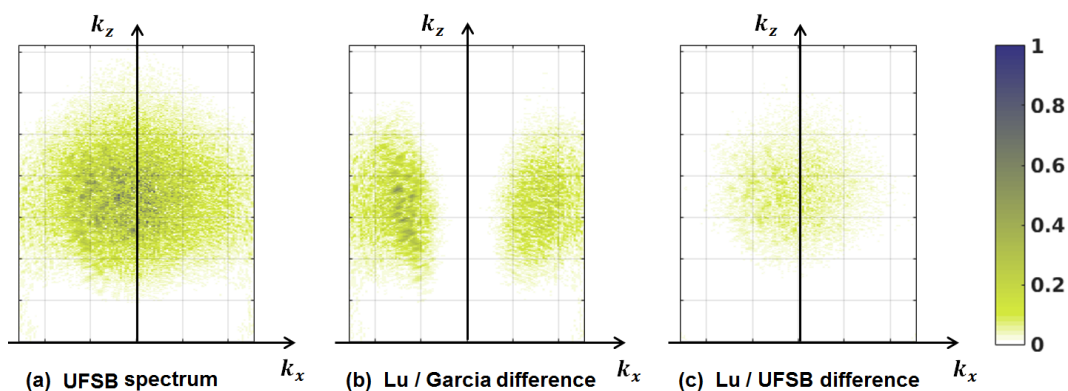
Figure 5.13: Spectrum mapping obtained from the experimental images given at the top row of Fig. 4.5. (a) Magnitude of the spectrum reconstructed using the proposed UFSB technique. (b) Absolute differences of Lu's and Garcia's spectrum. (c) Absolute differences of Lu's and UFSB's spectrum.

of angles used in reception. The computational complexity of the proposed UFSB method thus corresponds to $O(n_\xi\, n_e\, n_s)$, making this method less attractive than the other two Fourier-based methods. Even if the proposed UFSB method is not as attractive as Lu and Garcia in terms of complexity, it provides conceptual interesting link between ultrasound image formation and other imaging modalities such as computer tomography.

5.6 Summary

In this chapter, an alternative Fourier-based ultrafast imaging method (UFSB) was proposed. The theoretical aspect of the UFSB framework is based on the exploitation of the standard Fourier slice theorem for ultrasound image reconstruction. The reconstructive procedure, the spectrum boundary and the spectrum comparison with the other two Fourier-based methods for 1 PW (*i.e.* method of Lu and Garcia) are also given in details. Simulations and experiments are carried out to assess the UFSB imaging performances. Results obtained from simulations and experiments revealed that the UFSB technique produces very competitive results in terms of image quality compared to the state-of-the-art methods.

Chapter 6

Extension of Fourier-based methods to sectorial imaging in 2D

In this chapter, a general approach will be developed to extend Fourier-based ultrasound PW imaging methods to sectorial imaging with DW in transmission. Using this approach, most of the Fourier-based methods allow reconstructing a sectorial image from a DW using the same formalism as the one derived for PW. The extension of Lu's method allows the same image quality as spatial-based methods for DW, but with lower computational complexity.

6.1 Introduction

As mentioned in Chapter 3, many ultrafast imaging methods based on PW [Lu (1997), Montaldo *et al.* (2009), Garcia *et al.* (2013)] and DW [Hasegawa and Kanai (2011), Papadacci *et al.* (2014), Provost *et al.* (2014)] in transmission were proposed to reach high frame rates. As an alternative, we recently proposed in [Bernard *et al.* (2014)] a new technique (UFSB in Chapter 5) based on the Fourier slice theorem which allows sampling the Fourier space radially. The above mentioned ultrafast imaging methods perform the image reconstruction either in the Fourier domain [Lu (1997), Garcia *et al.* (2013), Bernard *et al.* (2014)] or in the space domain [Montaldo *et al.* (2009), Hasegawa and Kanai (2011), Papadacci *et al.* (2014), Provost *et al.* (2014)].

The main advantage of the Fourier-based approaches with respect to their spatial counterpart concerns the computational complexity, this aspect having been investigated in several studies in the context of linear acquisition from steered PW [Kruizinga *et al.*

(2012), Garcia *et al.* (2013)]. In particular, the computational complexity of the DAS method proposed in [Montaldo *et al.* (2009)] is equal to $O(n_e\, n_e\, n_s)$ and decreases to $O(n_e\, n_s \log(n_e\, n_s))$ for Fourier-based techniques [Garcia *et al.* (2013), Lu (1997)] (n_e representing the number of transducer elements and n_s the number of samples of the beamformed signal). It is worth noting that all the existing DW imaging methods work in space domain.

Based on these observations, an explicit transformation which allows a direct extension of existing Fourier-based techniques derived for linear acquisition to the reconstruction of sectorial images with wide angle (90°) is developed. The key idea is to express the problem of sectorial image reconstruction in a formalism which is equivalent to the formalism used for PW transmission. The method in this chapter is developed in 2D directly from the time-traveling equations involved when either a DW or a PW is emitted. The derived spatial transformation allows transforming the reference Cartesian space into a dedicated one where the modified medium can be considered as being excited by a PW. We show that the use of ultrasound Fourier-based techniques (methods of Lu and UFSB) from the received raw data along with the application of the proposed spatial transform allows reconstructing the insonified medium in the Cartesian space. Numerical simulations for point scatterers and anechoic cysts, experiments for CIRS phantom [CIR (2013)] and *in vivo* human heart are carried out to verify and evaluate the image quality (in terms of lateral resolution and image contrast) of the proposed method.

The main results in this chapter were presented at the IEEE International Ultrasonic Symposium in 2015 [Zhang *et al.* (2015)], and accepted as a journal paper in IEEE Transactions on Ultrasonics, Ferroelectrics, and Frequency Control [Zhang *et al.*].

6.2   Methodology

6.2.1   Extension of Fourier-based techniques to sectorial imaging

The key idea of this section is to establish an equivalence in terms of travel time when either a DW or a PW is used in transmission as illustrated in Figure 6.1. Indeed, such a relation would allow the reconstruction of a sectorial image from a DW using the same formalism as the one derived for linear acquisition. Isomorphism between travel times has already been used by Garcia *et al.* to adapt the seismic Stolt's migration technique to ultrasound PW imaging [Garcia *et al.* (2013)].

As shown in Figure 6.1, a 1-D linear array transducer located at $z = 0$ plane, centered at $x = 0$, where each transducer element E is positioned at $(x_E, 0)$, is excited to generate a DW (Figure 6.1a) or a PW (Figure 6.1b) to insonify the medium. For the moment, we assume that the aperture of the transducer is infinitely large for the PW transmission. A DW is obtained through the excitation of a virtual source located behind the probe and placed at (x_v, z_v), where $z_v \leq 0$ is determined by the chosen angular aperture α and the
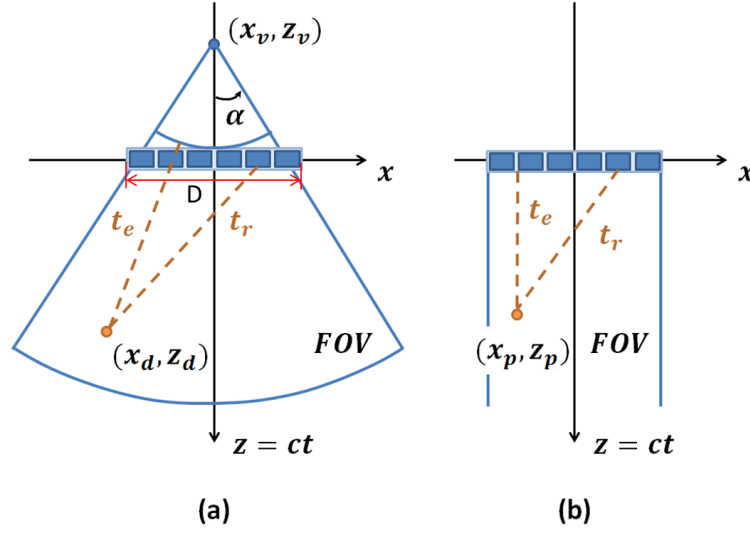
Figure 6.1: Illustration of the travel time (represented by t_e and t_r) involved when either (a) a DW or (b) a PW is used in transmission. In both cases, $(t_e + t_r)$ corresponds to the time needed by the insonifying wave to reach a scatterer (orange dot) and then come back to a specific transducer element.

sub-aperture width D, as in Figure 6.1a:

$$z_v = -\frac{D/2}{\tan(\alpha)} \tag{6.1}$$

The transmit delays Δ_E associated with the virtual source position are then computed as:

$$\Delta_E = \left(\sqrt{(x_E - x_v)^2 + z_v^2} + z_v \right) / c \tag{6.2}$$

Where c is the speed of sound, assumed to be homogeneous in the whole medium (1540 m/s in soft tissues). The second term in the brackets $+z_v$ is used as an offset to ensure that the smallest transmitted delay is null, x_E varies with different element positions.

In this context, the traveling time of a DW to reach a point scatterer positioned at (x_d, z_d) in the medium and to come back to a transducer element placed at $(x_E, 0)$ is given by:

$$\tau_d(x_E) = \left(\sqrt{(x_d - x_v)^2 + (z_d - z_v)^2} + z_v + \sqrt{(x_d - x_E)^2 + z_d^2} \right) / c \tag{6.3}$$

Where $\sqrt{(x_d - x_v)^2 + (z_d - z_v)^2} + z_v$ corresponds to the distance that the wave travels to reach the scatterer, and $\sqrt{(x_d - x_E)^2 + z_d^2}$ corresponds to the distance between the scatterer point and the transducer element.

In the case of PW with normal incidence, the travel time involved to reach a point

scatterer (x_p, z_p) and to come back to the same transducer element $(x_E, 0)$ is given by:

$$\tau_p(x_E) = (z_p + \sqrt{(x_p - x_E)^2 + z_p^2}\,) \, / \, c \tag{6.4}$$

By equating the first order Taylor approximation of (6.3) and (6.4) at $x_E = x_v$, the following relation between (x_d, z_d) and (x_p, z_p) can be derived:

$$
\begin{cases}
x_p \approx \dfrac{(x_d - x_v)\left(\sqrt{(x_d - x_v)^2 + (z_d - z_v)^2} + z_v + \sqrt{(x_d - x_v)^2 + z_d^2}\right)}{z_d + \sqrt{(x_d - x_v)^2 + z_d^2}} \, + \, x_v \\[4ex]
z_p \approx \dfrac{z_d \left(\sqrt{(x_d - x_v)^2 + (z_d - z_v)^2} + z_v + \sqrt{(x_d - x_v)^2 + z_d^2}\right)}{z_d + \sqrt{(x_d - x_v)^2 + z_d^2}}
\end{cases}
\tag{6.5}
$$

and

$$
\begin{cases}
x_d \approx \dfrac{1}{2} \dfrac{(x_p - x_v)\left(z_v^2 - \left(z_p + \sqrt{(x_p - x_v)^2 + z_p^2} - z_v\right)^2\right)}{z_v\, z_p - \left(z_p + \sqrt{(x_p - x_v)^2 + z_p^2} - z_v\right)\sqrt{(x_p - x_v)^2 + z_p^2}} \, + \, x_v \\[4ex]
z_d \approx \dfrac{1}{2} \dfrac{z_p \left(z_v^2 - \left(z_p + \sqrt{(x_p - x_v)^2 + z_p^2} - z_v\right)^2\right)}{z_v\, z_p - \left(z_p + \sqrt{(x_p - x_v)^2 + z_p^2} - z_v\right)\sqrt{(x_p - x_v)^2 + z_p^2}}
\end{cases}
\tag{6.6}
$$

Eq. (6.5) and Eq. (6.6) give an explicit equivalence between the scatterer positioned at (x_d, z_d) and (x_p, z_p), which is insonified by a DW with virtual source (x_v, z_v) and a horizontal PW, respectively. Thus, the following procedure is proposed to reconstruct a sectorial image: *i)* a DW with virtual source positioned at (x_v, z_v) is transmitted using a standard phased-array; *ii)* a standard Fourier-based technique (*e.g.* method of Lu and UFSB) for PW is applied to the received echoes. Thanks to Eq. (6.5), one can see that this step will reconstruct the desired ultrasound image but expressed in the (x_p, z_p) coordinate system; *iii)* the spatial transformation given through Eq. (6.6) is applied which allows expressing the reconstructed image in the conventional Cartesian space.

It is worth pointing out that Eq. (6.5) and Eq. (6.6) have been obtained for the particular case where $x_E = x_v$, meaning that the equivalence between the traveling time of Eq. (6.3) and Eq. (6.4) is exact only near the region defined by $x = x_v$, where the Taylor approximation remains valid. We thus investigate the error in terms of travel time difference for the special case $x_v = 0$ when the relation (6.5) and (6.6) are used for each point in the medium. More precisely, for each point (x_d, z_d) of the medium, we first compute the set of travel times $\{\tau_d(i)\}_{i \in [1, N]}$ (by Eq. (6.3)) from the virtual source point $(0, z_v)$ to (x_d, z_d) and back to each transducer element i of the probe (N being the number of elements). Thanks to Eq. (6.5), we then derived the corresponding
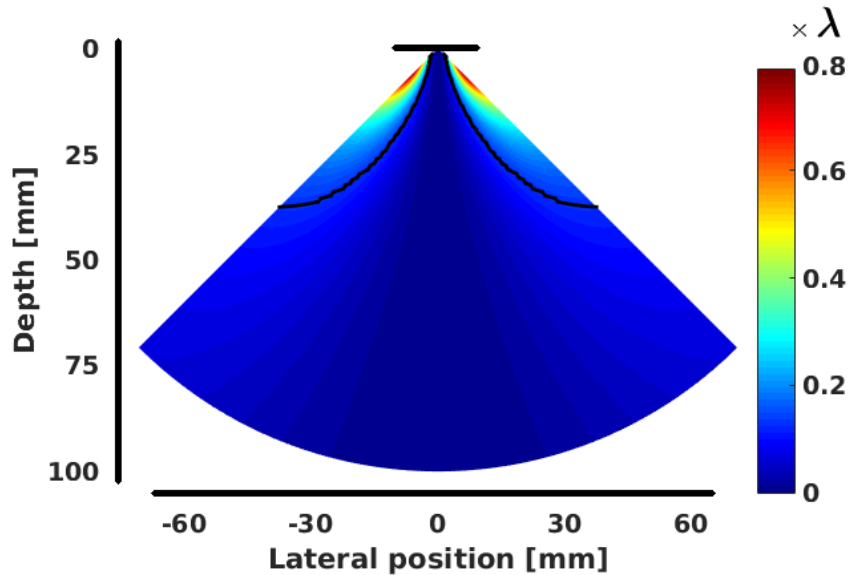
Figure 6.2: Error map derived from the traveling time equivalence between a sectorial acquisition using DW and the equivalent plane-wave imaging after the application of the proposed spatial transformation. The computed error is expressed relatively to the wavelength used in the experiments. The black line on the top of the figure models the transducer location while the axis origin is located at the center of the probe. The two black curves drawn inside the error map represent the boundary of the region at the edge of the image where the maximum error is higher than $\lambda/8$.

(x_p, z_p) points and computed the set of travel times $\{\tau_p(i)\}_{i \in [1,N]}$ (by Eq. (6.4)) from the probe to (x_p, z_p) back to each transducer element i. In the case of a perfect equivalence between the two systems (sectorial and linear after spatial transformation), the set of the pair-wise difference $\tau_d(i) - \tau_p(i)$ over the probe element should be zero. Figure 6.2 shows the corresponding maximum value (*i.e.* $\max_i(\tau_d(i) - \tau_p(i))$) computed for each point of the medium in terms of the wavelength λ. From this figure, one may first observe that there is no difference in terms of travel time at the center of the probe and this error increases when approaching the edge of the image. The maximum error appears in the near field (depth lower than 1-cm) at the edge of the image with a value around $0.8 \times \lambda$. This figure also allows the assessment of the potential defocusing effect induced by the proposed formulation. Indeed, each value displayed in Fig. 6.2 corresponds to the maximum of the error between the two systems computed over the full aperture. Since for each reconstructed point, the travel time error for most of the elements is below $\lambda/8$ (which is the commonly accepted value under which errors in travel distances can be neglected), it reveals the marginal effect of defocusing during the beamforming process. A more detailed investigation of this particular aspect is given in Appendix A.1. Finally, it is worth pointing out that the negligible effect of defocusing also justifies the correct reconstruction of the point positioning after the spatial transformation. This aspect will be further investigated in Section 6.3.2.

6.2.2   Reconstructive procedure and practical implementation

In this section, we combine the derived spatial transformation in the previous section with the Fourier-based techniques of UFSB and Lu for DW imaging. These two methods are indeed well adapted to the proposed framework since the underlying image formation is based on the use of the same transducer both in transmission and reception. Contrary to these approaches, the method of Garcia expresses the image formation through the exploding reflector model, leading to approximations which are not adapted in this work (see [Garcia *et al.* (2013)] for more details). The generic implementation of the procedure for sectorial imaging from the two Fourier-based techniques (*i.e.* UFSB and Lu) can be summarized as follows:

1. Transmit one or several DW to insonify the medium. The DW is implemented by delaying the firing time of each element of the array. The delay is given by Eq. (**??**) associated with the virtual source position (x_v, z_v). Then receive the back-scattered echoes on each transducer element simultaneously, a two dimensional data set is collected for each DW insonification.

2. Apply a Fourier-based PW imaging method (*i.e.* method of Lu or UFSB) to each collected echoes to reconstruct the corresponding RF image. The RF image obtained here is expressed in the dedicated space with positions (x_p, z_p).

3. Apply the spatial transformation given through Eq. (6.6) to reconstruct the RF image in the Cartesian space with coordinates (x_d, z_d).

4. If successive DW were used to perform coherent compounding, repeat steps 2 and 3 for each firing and average all the reconstructed RF images to get the final compounded image.

Note that step 2 implies the interpolation of the collected data on a regular grid in the Fourier domain in order to compute the reconstructed image using a regular 2D inverse Fourier transform. Such interpolation is an old topic which has been widely studied in the literature [Stark *et al.* (1981), O'sullivan (1985), Jackson *et al.* (1991)]. In particular, as described in details in [O'sullivan (1985)], the linear interpolation applied in k-space leads to the multiplication of the real image by a squared *sinc* function. This results in a decrease of the intensity of the current reconstructed image along depth. To reduce this artifact, we applied a depth-varying intensity correction for the Fourier-based techniques. An intensity correction of 0.5-dB/MHz/cm was used.

6.3   Numerical simulations

In this section, we evaluate the performance of the proposed framework associated with the Fourier-based techniques of UFSB and Lu. For all the tests, the extended methods are compared with the current state-of-the-art spatial-based method of Papadacci *et*

al. [Papadacci *et al.* (2014)]. A standard phased-array probe of 64 elements with a center frequency of 2.5-MHz (100% bandwidth), 0.32-mm pitch, 13-mm height and 60-mm elevation focus was implemented using Field II [Jensen and Svendsen (1992)]. No apodization was used in both transmission and reception. Each reconstructed image is obtained following this protocol: i) raw-data signals are acquired using DW with different virtual source point positions; ii) those signals are processed either following the proposed extension framework or using the method of Papadacci in order to obtain the compounded RF image; iii) the corresponding envelope image is derived through a Hilbert transform and normalized; iv) the envelope image is then gamma-compressed using $\gamma = 0.3$ as in [Garcia *et al.* (2013)] and finally converted to 8-bit grayscale to get the final B-mode image.

6.3.1 Transmission scheme

For comparison purposes and because of its efficiency, we propose to use the same transmission scheme as the one proposed in [Papadacci *et al.* (2014)], *i.e.* emitting several DW with virtual sources positioned at a certain z_v and for different x_v values. Each DW is emitted from a virtual source point with an angular aperture of 90° and a sub-aperture width composed of 21 elements. For a single transmission, the virtual source is placed at the center of the probe. For three transmissions, the two others sources are placed near the edges of the transducer (*i.e.* at x_v = [-6.7, 0, 6.7]-mm in our experiments). For more than three transmissions, the additional virtual sources are uniformly distributed (*i.e.* x_v = [-6.7, -3.35, 0, 3.35, 6.7]-mm for 5 transmissions in our experiments).

6.3.2 Validation of the extension model

In this section, we investigated the conceptual correctness of the proposed framework for the reconstruction of sectorial images from Fourier-based techniques. To this aim, we used a simple synthetic phantom composed of a discrete set of point scatterers. Firstly, we use 1 DW in transmission to validate the space transformation that we derived in Section 6.2. Figure 6.3 displays the corresponding images in the modified space with positions (x_p, z_p) (Figure 6.3a) and in the Cartesian space by the methods of UFSB (Figure 6.3b) and Lu (Figure 6.3c). The red circles correspond to the real position of the scatterers. From Figure 6.3a, it can be seen that applying the UFSB method directly on the received raw-data (collected from one DW in transmission) results in a dilation of the scatterer positions. The derived space transformation (Eq. (6.5) and Eq. (6.6)) allows reconstructing all the scatterers with the correct positions in the Cartesian space (Figure 6.3b). Figure 6.3c is the image reconstructed from the extension model of Lu. Visually, the two images (reconstructed by the extension of UFSB and Lu) are quite similar, we will investigate the image quality in the following section. These figures illustrate the marginal effect of the error map presented in Section 6.2.

The image quality can be improved by compounding coherently the images obtained with several DW at different virtual source positions. To validate the compounding model
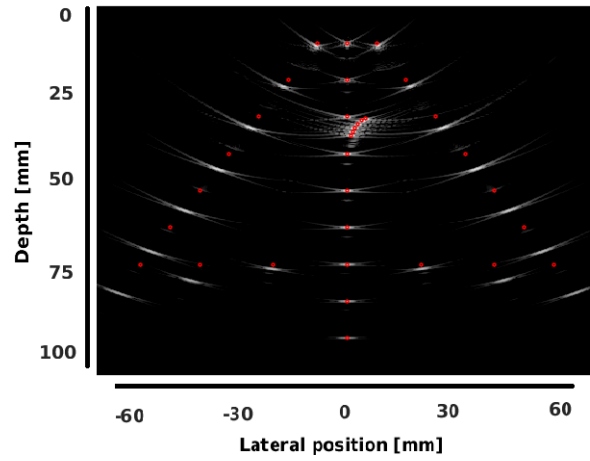
(a) Reconstructed image direct from UFSB method
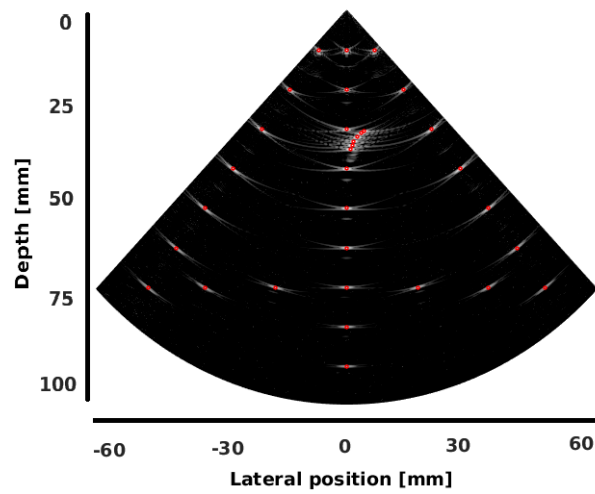
(b) Sectorial extension of UFSB method
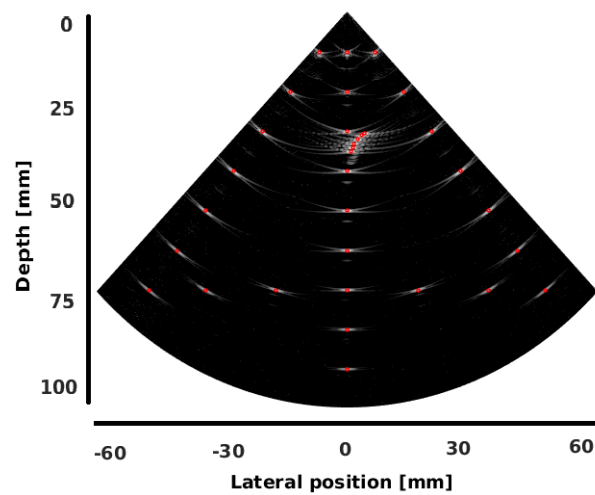
(c) Sectorial extension of Lu's method

Figure 6.3: Synthetic phantom reconstruction direct from (a) UFSB and from the extension methods of (b) UFSB and (c) Lu using 1 DW in transmission. The red circles correspond to the true position of the involved scatterers.

of the proposed framework, we choose a set of 15 DW with virtual source positioned on a line parallel to the x-axis, as described in Section 6.3.1. For each DW, an image is built following the previous procedure. All images are then added coherently to obtain a final compounded image. Figure 6.4 displays the corresponding images reconstructed from the algorithm described in Section 6.2.2 associated with the Fourier-based method of UFSB (Figure 6.4a) and Lu (Figure 6.4b) as well as the method of Papadacci. Compared with the images in Figure 6.3, it can be seen that the artifacts are eliminated thanks to the image compounding. The red circles correspond to the real position of the scatterers. From these figures, it can be seen that the proposed formulation allows the reconstruction of all the scatterers with the correct positions whatever the chosen Fourier-based technique and the virtual source positions of the DW.

6.3.3   Image quality evaluation

Lateral resolution

The quality of the reconstructed images was then evaluated through the lateral resolution using the numerical phantom displayed in Figure 6.4. The corresponding values were measured as the full width at half maximum of the point spread function associated to the points located at 20-mm, 40-mm, 60-mm and 80-mm in the envelope image (no gamma-compression was used here). Figure 6.5a investigates the influence of the number of DW on the lateral resolution using the different reconstruction techniques and for the different depths at the middle (azimuth angle of 0°). First, it can be seen that the 3 methods produce similar image quality whatever the depth and the number of involved DWs. In particular, it can be observed that the lateral resolution improves quickly for 3 DW and then tends to stabilize to the optimal value, *i.e.* around 0.8-mm at 20-mm depth, 1.4-mm at 40-mm depth, 2.0-mm at 60-mm depth and 2.7-mm at 80-mm depth. It is also important to note that, for each depth, the lateral resolution tends to decrease a little bit after the compounding of 3 DWs. This behavior can be explained by the chosen transmission scheme. Indeed, in the particular case of a monochromatic far-field approximation at a focal distance F, the width W of the main lobe corresponding to a coherent summation of N DW is in the order of (see Eq. (4) in [Papadacci *et al.* (2014)]):

$$W = 2 \frac{\lambda F}{W_{va}} \frac{N-1}{N} \tag{6.7}$$

where $\lambda = 2\pi/k$ and W_{va} corresponds to the width of virtual array which is considered as fixed in this study. Based on this equation, we display in Figure 6.6 the evolution of the approximation of the full width at half-maximum from the probe settings used in our simulations at a focal distance of 60-mm. From this figure, one can see that the theoretical evolution of this measure (which is directly linked to the lateral resolution of the system) for increasing number of DW is coherent with the lateral resolution measured in simulations.
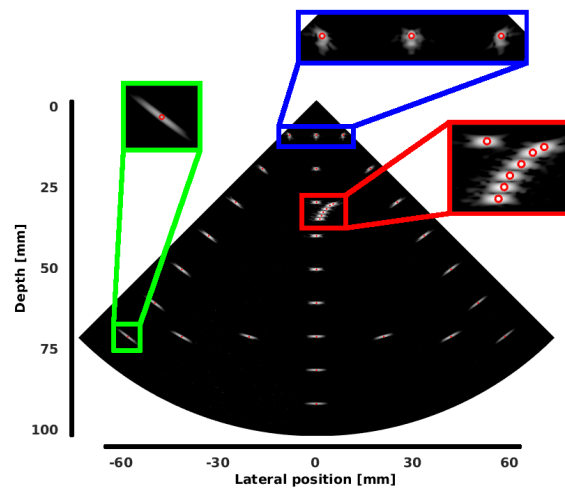
(a) Sectorial extension of UFSB method
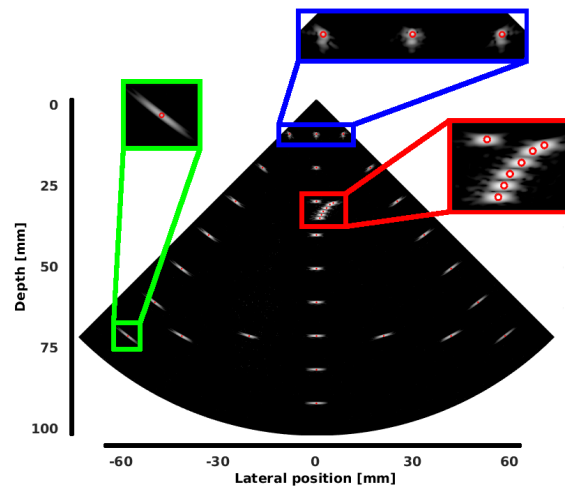
(b) Sectorial extension of Lu's method
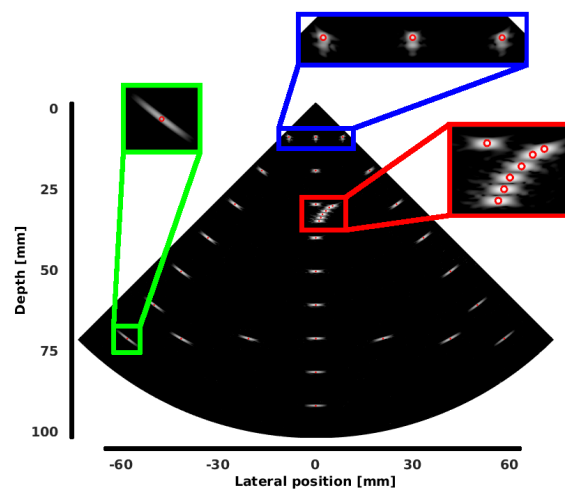
(c) Papadacci's method

Figure 6.4: Synthetic phantom reconstructed from the extension of the Fourier-based methods of (a) UFSB and (b) Lu as well as (c) the method of Papadacci using 15 DW in transmission. The red circles correspond to the true position of the involved scatterers.

(a)

(b)
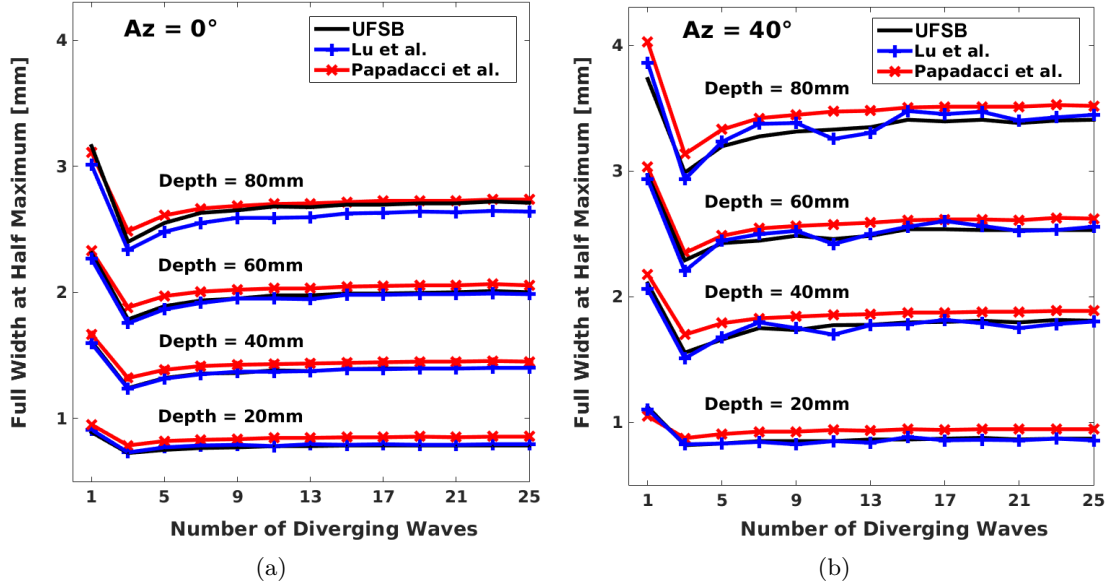
Figure 6.5: Numerical phantom - lateral resolution measurements as a function of the number of DW computed at 20-mm, 40-mm, 60-mm and 80-mm at (a) the middle of the image (azimuth angle of 0°) and (b) at the edge of the image (azimuth angle of 40°).
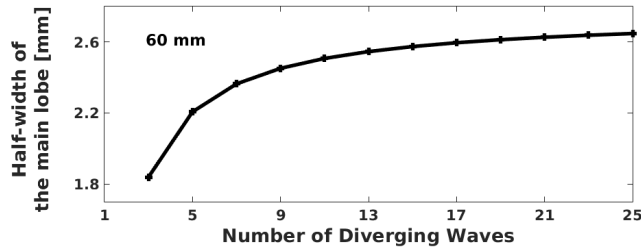
Figure 6.6: Approximation of the half-width of the main lobe corresponding to the coherent summation of DW in the case of a monochromatic far-field at a focal distance of 60-mm.

Figure 6.5b investigates the influence of the number of DW on the lateral resolution using the different reconstruction techniques and for different depths at the edge of the image (azimuth angle of 40°). As for the middle case, it can be seen that the 3 methods produce similar image quality whatever the depth and the number of the involved DWs. It is also interesting to note that the lateral resolution (computed along the azimuth direction for consistency) degrades with the azimuth angle. For instance, at 80-mm depth, the lateral resolution goes from values around 2.7-mm at the middle of the image to values around 3.4-mm at the edge. This phenomenon can be explained by the fact that the region where the different DWs contribute to the image pixels is optimal at the middle of the image, leading to a better image resolution. The limited opening angle of the effective aperture may also reinforce this phenomenon. Finally, it can be observed from Figure 6.5a and 6.5b that the difference in terms of lateral resolution between Papadacci's method and the Fourier based methods varies in average from 0.06-mm (at 20-mm depth) to 0.10-

mm (at 80-mm), which corresponds of a maximum difference lower than $\lambda/6$. Since this difference is much lower than half of the wavelength, this phenomenon may be considered as negligible.

Image contrast

The contrast of the reconstructed image was then investigated and measured from the B-mode images using the classical contrast ratio (CR) (see Eq.(2.5) in Section 2.1.4). Figure 6.7 and Figure 6.8 display the contrast of the reconstructed images with different number of DWs in transmission at the middle (azimuth angle of 0°) and the edge (azimuth angle of 40°) of the image, respectively. The comparison was made by using a synthetic medium with high density of scatterers (20 per resolution cell) with two anechoic cysts of diameter 8-mm lying at 40 and 80-mm depth, respectively. The phantom was insonified with successive DW according to the compounding scheme described in Section 6.3.1. Figure 6.7a and Figure 6.8a display the CR values measured at the two different depths for different number of DW and different azimuth angles. The three methods yield very close results, the CR measurements showing same tendency with an increasing number of DW and with better CR scores at 40-mm. This can be easily explained by the intrinsic decrease of the transmit ultrasound pressure with depth which inevitably induces lower contrast. It is of importance to note that the image contrast decreases a little with the azimuth angle. For instance, at 40-mm depth, the CR decreases from values around 13-dB at the middle of the image down to values around 10-dB at the edge. This phenomenon can be explained by the same reason as for lateral resolution that the region where the different DWs contribute to the image pixels is optimal at the middle of the image. The limited opening angle of the effective aperture may also reinforce this phenomenon. It is also interesting to note that for more than 15 DW, the image contrast tends to stabilize to the optimal value for all methods, which is consistent with the results provided in [Papadacci et al. (2014)]. Finally, Figure 6.7b to 6.7d display the images reconstructed with the three different methods using 15 DW. These results illustrate visually the closeness in terms of image quality and speckle definition of the images reconstructed from the proposed extension of the Fourier-based techniques and the spatial-based method of Papadacci *et al.*

We also assessed the performance of the different methods in terms of contrast for varying level of noise added on the received echoes using the numerical phantom displayed in Figure 6.7. Figure 6.9 displays the measured contrast as a function of the number of DW with two different signal-to-noise ratios (SNR) applied on the received echoes: one case corresponding to a higher level of noise (Figure 6.9a, SNR = 10 dB) and one case corresponding to a moderate level of noise (Figure 6.9b, SNR = 20 dB). Compared with Figure 6.7a, one can first observe that an increase of the noise on the received signal naturally degrades the quality of the reconstructed images for all the methods, which goes from an optimal value of 14 dB using the signal without noise to a maximum value of

(a) Contrast ratio measurements for different depths

(b) Sectorial extension of UFSB method

(c) Sectorial extension of Lu's method

(d) Papadacci's method
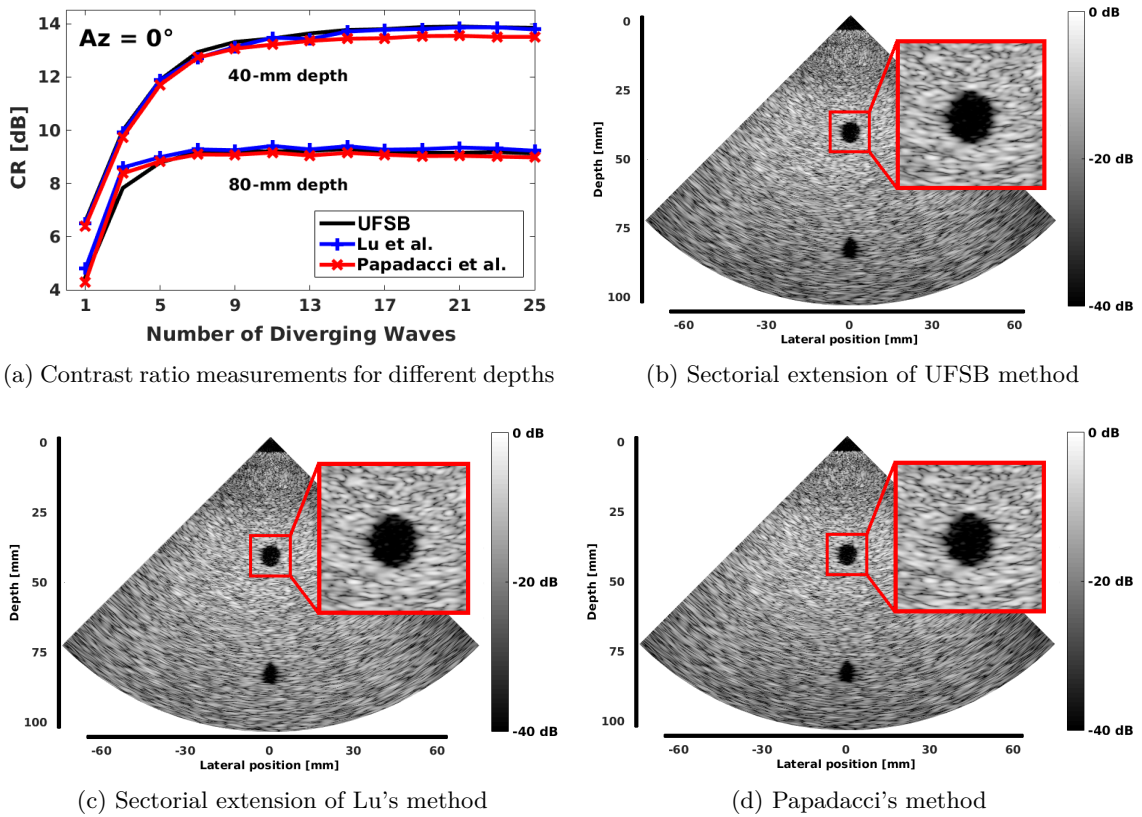
Figure 6.7: Numerical phantom - (a) contrast ratio measurements as a function of the number of DW. B-mode images reconstructed from (b) the proposed extension of UFSB method, (c) the proposed extension of Lu's method and (d) the spatial-based method of Papadacci using 15 DW with coherent compounding.

(a) Contrast ratio measurements for different depths

(b) Sectorial extension of UFSB method
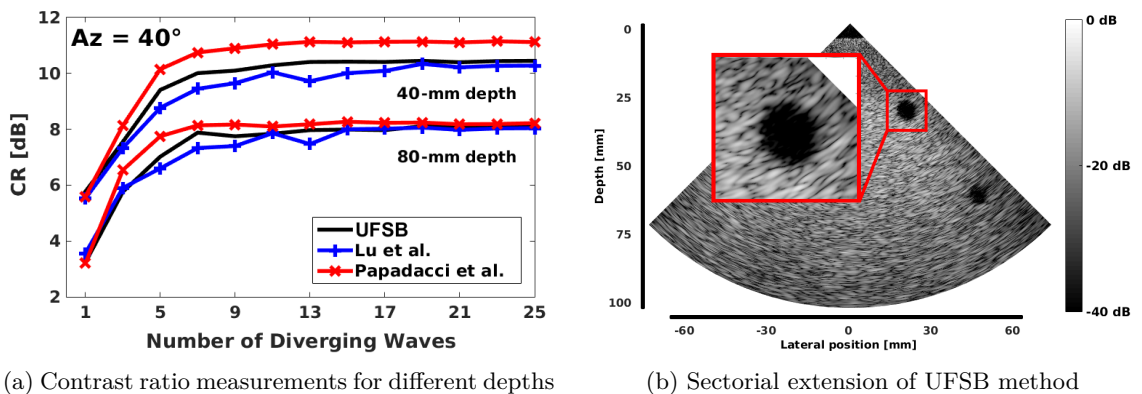
Figure 6.8: Numerical phantom - (a) contrast ratio measurements computed at the edge of the image (azimuth angle of 40°) as a function of the number of DW. B-mode images reconstructed from (b) the proposed extension of UFSB method using 15 DW with coherent compounding.

12.6 dB using the received signal with a SNR of 10 dB. Moreover, one can see that the influence of the noise is stronger for a low number of DW involved in the compounding scheme (DWs ≤5). This highlights the need of performing compounding with more DW in order to reduce the influence of potential source of noise that could affect the received data. Finally, it is interesting to note that in all cases, the contrast values tend to stabilize to the maximum value when the number of DW is larger than 15, which illustrates the consistency of the tested methods with noise.

(a) SNR = 10dB   (b) SNR = 20dB
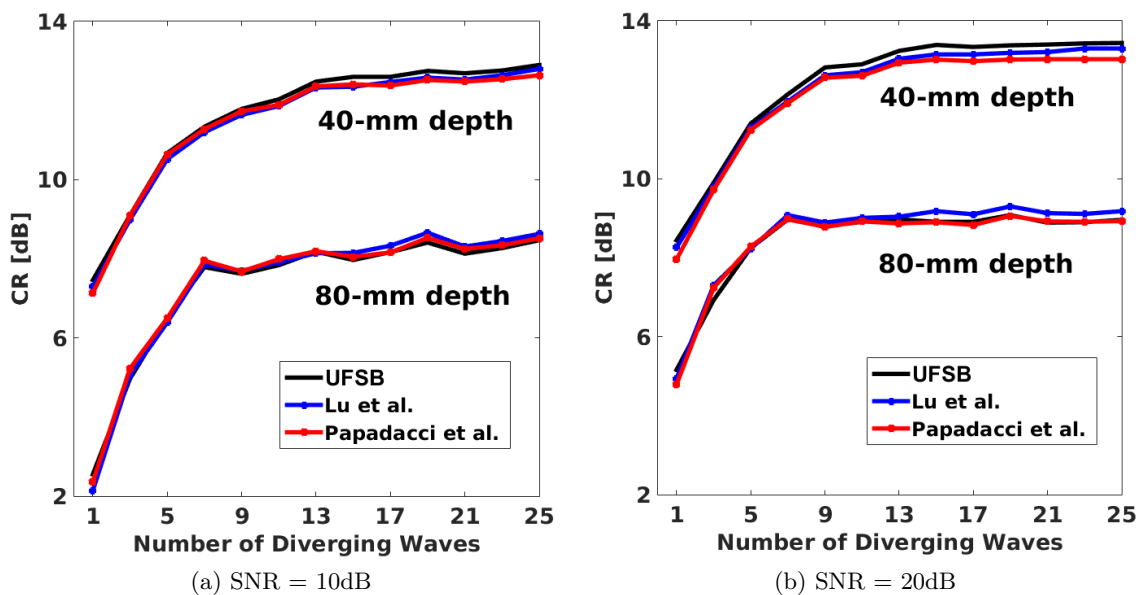
Figure 6.9: Numerical phantom - Contrast ratio measurements as a function of the number of DW with an SNR of (a) 10dB and (b) 20dB.

6.4 *In vitro* and *in vivo* experiments

6.4.1 *In vitro* experiment on CIRS phantom

The imaging quality was also assessed experimentally using an ultrasound phantom (CIRS model: 054GS) [CIR (2013)]. Figure 6.10 displays the schematic diagram of the corresponding phantom along with the imaging sector used in this experiment. A standard phased array probe (64 elements, center frequency of 2.5-MHz, Verasonics - P4-2) with the same characteristics as the one used in simulations was interfaced with a Verasonics system to image the phantom from DW. The imaging depth was set to 100-mm. The number of emitted DW varied from 1 to 25, providing a frame rate between 7700 and 308 frame per second (fps), respectively. The transmission properties of the DW (angular aperture, sub-aperture width and virtual source positioning) were the same as the ones used in simulations. The received raw-data were processed using the proposed Fourier-based framework and the method of Papadacci *et al.* The beamformed RF data were
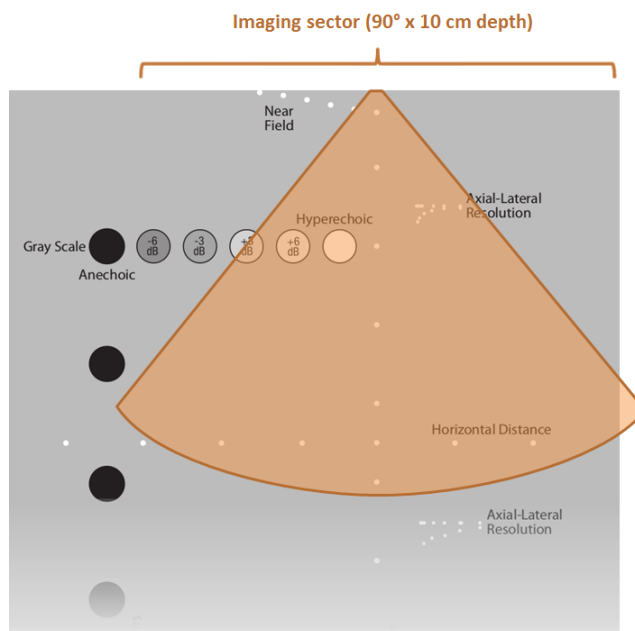
Figure 6.10: Schematic diagram of the CIRS tissue-mimicking phantom with the corresponding imaging sector used in the DW experiments.

time-gain compensated and the corresponding envelope images were log-compressed to obtain the final B-mode images with a 60-dB dynamic range.

Lateral resolution

The lateral resolution was first investigated from the acquisition centered on the 0.1-mm nylon monofilament targets displayed in Figure 6.10 and positioned at 20-mm, 40-mm, 60-mm and 80-mm. Figure 6.11 investigates the improvement of the lateral resolution with the number of DW for the different reconstruction techniques and for the different depths. One can first see that all the experimental results are consistent with what have been previously observed from simulations, both in terms of tendency and measured values. Indeed, for all the methods, the lateral resolution improves quickly for 3 DW and then tends to stabilize to the optimal value, *i.e.* around 0.8-mm at 20-mm depth, 1.4-mm at 40-mm depth, 2.1-mm at 60-mm depth and 3.2-mm at 80-mm depth. Moreover, it is worth pointing out that at each depth, the different methods tend to have a stable lateral resolution for the transmission of 15 DW, leading to a frame rate of 855 fps.

Image contrast

We investigated in Figure 6.12 the quality of the reconstructed images in terms of contrast. In particular, Figure 6.12a displays the CR values measured at 40-mm depth for each compounding experiment. From the corresponding graph, it can be observed that the three methods yield very close results. The CR measurements involve same tendency over the increase of the number of DW. The optimal CR values are reached in all cases after the
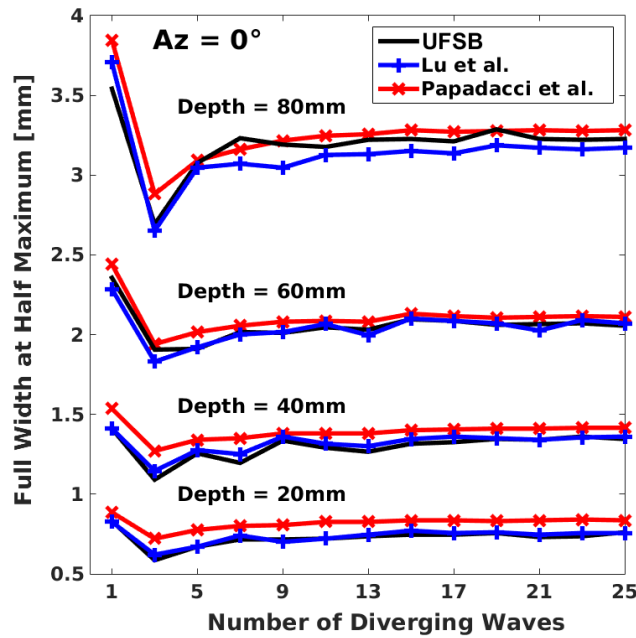
Figure 6.11: Real acquisition - lateral resolution measurements as a function of the number of DW computed at 20-mm, 40-mm, 60-mm and 80-mm at the middle of the image.

transmission of 15 DW (frame rate of 855 fps), which is in accordance with the simulation results we obtained in Section 6.3.3. Figure 6.12b to 6.12d display the reconstructed B-mode images obtained using 15 DW with coherent compounding. As in simulations, these results illustrate visually the closeness in terms of image quality and speckle definition of the images produced by different methods. It is also interesting to note that the decrease of the intensity observed at the two borders of the image can be explained, on the left side, by the presence of a structure with high reflectivity (due to an unexpected flaw present in the CIRS phantom we used at the interface between the background and the hyperechoic cyst of +3dB) which produces classical ultrasound shadow and, on the right side, by the physical limit of the CIRS phantom which induces reverberation phenomenon. Finally, the limited opening angle of the transducer elements and the limited opening angle of the effective aperture may be additional causes responsible for the observed decrease of intensity at the edges.

6.4.2 *In vivo* experiment of a human heart

Finally, we investigated the performance of the extended Fourier-based ultrafast imaging methods of the human heart *in vivo*. As introduced in Section 3.3, tissue motion is an important factor that causes phase shift, leading to a degradation of image quality. For an *in vivo* heart, therefore, the phase delays due to the heartbeat must be compensated during the coherent compounding process to minimize the image degradation. The experiment was performed with a Verasonics research scanner (V-1-128, Verasonics Inc., Redmond, WA) and a 2.5MHz phased array transducer (ATL P4-2, 64 elements), with

(a) Contrast ratio measurements

(b) Sectorial extension of UFSB method

(c) Sectorial extension of Lu's method

(d) Papadacci's method
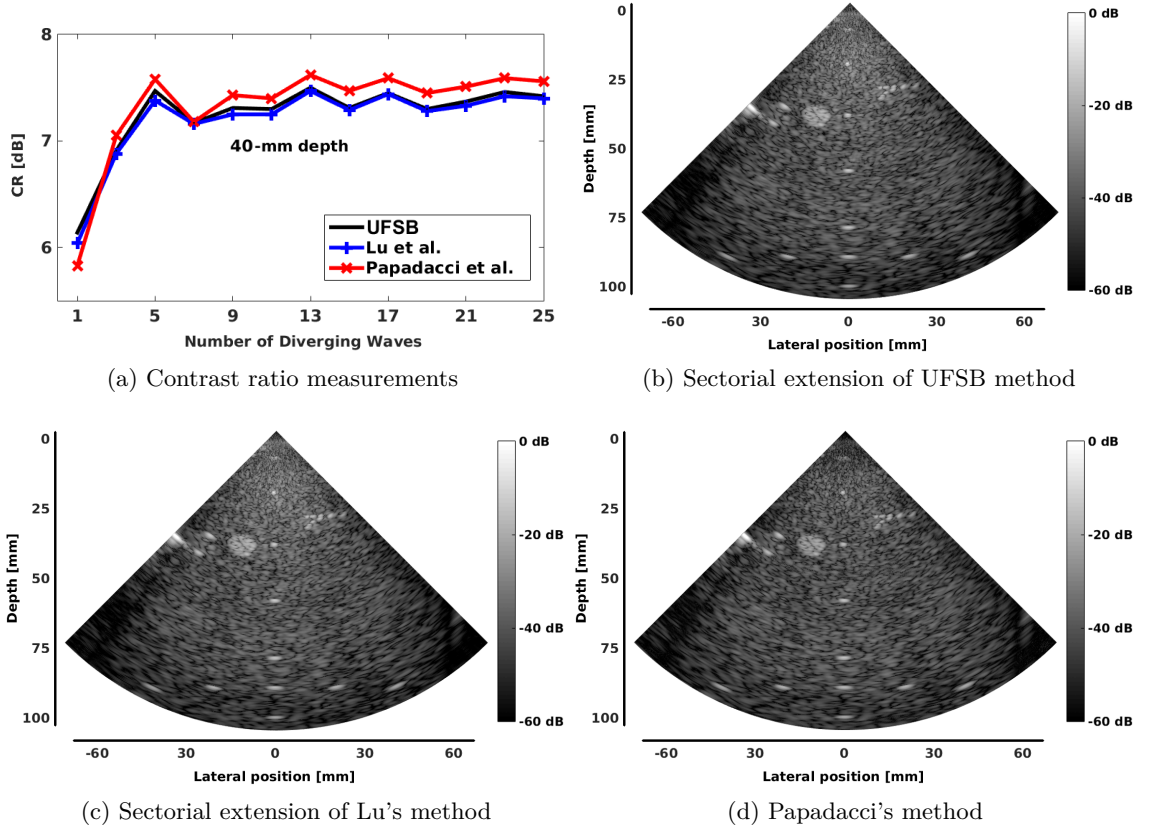
Figure 6.12: Real acquisition - (a) Contrast ratio measurements as a function of the number of DW. B-mode images reconstructed from (b) the proposed extension of UFSB method, (c) the proposed extension of Lu's method and (d) the spatial-based method of Papadacci using 15 DW with coherent compounding.

central frequency = 2.5MHz, fractional bandwidth at 6 dB = 60%, pitch =0.3 mm, kerf =50 μm. In order to assess the ability of our approach to deal with *in vivo* data, we applied the exact same triangle transmission scheme as the one described in [Poree *et al.* (2016)], *i.e.* 32 diverging beams generated by the full array aperture, with 90° angle aperture, the tilt angles linearly spaced between $-25°$ and $25°$ (see Figure 3.5 in Section 3.3.2).

Firstly, we reconstruct the cardiac image using the extended Fourier-based methods and spatial-based Papadacci's method without any motion compensation, as shown in Figure 6.13. As in simulations and *in vitro* experiments, these results illustrate visually the closeness of the images produced by different methods in terms of image quality and speckle definition. However, motion artifacts can be observed in the image, as illustrated in [Poree *et al.* (2016)]. This is due to the fact that the myocardium velocities can reach speed value around 20 cm/s during systolic event, resulting in non negligible tissue motion between two consecutive DW transmits.

In order to minimize the influence of motion on the image quality, Poree *et al.* proposed in [Poree *et al.* (2016)] to integrate the Doppler-based motion compensation (MoCo, described in Section 3.3.2) in the coherent compounding process of DAS method (*i.e.* method

of Papadacci). We thus investigated the feasibility of integrating the motion compensation proposed by Poree *et al.* with the proposed Fourier-based approach. Figure 6.14 displays one particular frame of the full sequence we reconstructed from a real acquisition using the sectorial extension of Lu's method with and without motion compensation. It can be seen that the image quality is improved with MoCo. In particular, the septum became well perceptible and contrasted in Figure 6.14b. This result also demonstrates the feasibility to apply the proposed method for *in vivo* acquisition, as well as its flexibility, since we could easily integrate the motion compensation framework proposed by Poree *et al.* [Poree *et al.* (2016)].

6.5   Discussion

6.5.1   Fourier-based methods of sectorial imaging

We proposed in this study an explicit transformation which allows the extension of existing Fourier-based approaches, initially proposed for linear acquisition, to the reconstruction of sectorial images with wide angle using DW. The proposed formulation was evaluated through the extension of two Fourier-based techniques, *i.e.* the one proposed by Lu *et al.* which samples the Fourier space along the k_z axis direction and the one of Bernard *et al.* which samples the Fourier space radially. Results obtained from both simulations and experiments revealed that the two extended Fourier-based approaches of Lu and Bernard reconstruct images with comparable quality as it is the case for linear acquisition, the introduced spatial transform having no effect on their relative behavior. More importantly, we also demonstrated in this study that the proposed extended Fourier-based approaches produce competitive results compared to the state-of-the art method proposed by Papadacci *et al.* both in terms of lateral resolution and image contrast.

Although the proposed transformation has been specifically designed for the transmission scheme described in [Papadacci *et al.* (2014)] (*i.e.* the virtual source point of each DW lies on a horizontal line positioned behind the probe), our approach can also be easily used for other strategies like, for instance, the steered DW presented in [Hasegawa and Kanai (2011)] and [Poree *et al.* (2016)]. In the case of steered DW of angle θ, the second term z_v of Eq.(6.2) has to be simply replaced by $-\min_E \sqrt{(x_E - x_v)^2 + z_v^2}$ to ensure that the smallest transmit delay is null. The same reasoning then holds to derivate the akin spatial transformation. The corresponding equations have been used to produce the results given in Section 6.4.2.

6.5.2   Computational complexity

One strong interest of Fourier-based techniques for sectorial acquisition is a potential reduction of the computational complexity compared to the conventional DAS method. To determine the computational complexity of the proposed extension of Lu and Bernard methods, let n_e denotes the number of elements that compose the transducer (in general
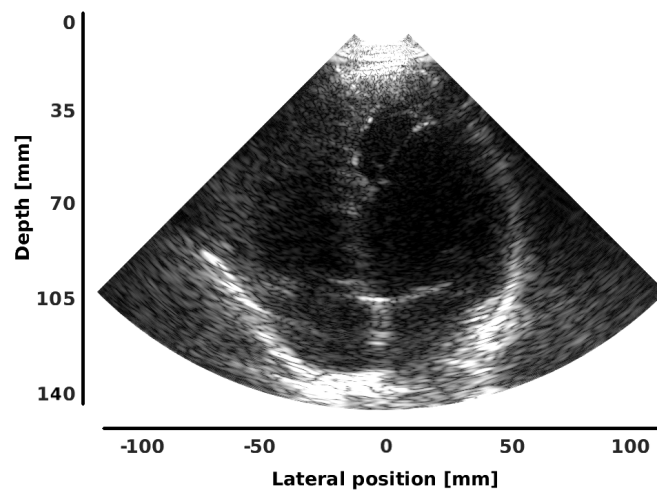
(a) Sectorial extension of UFSB method
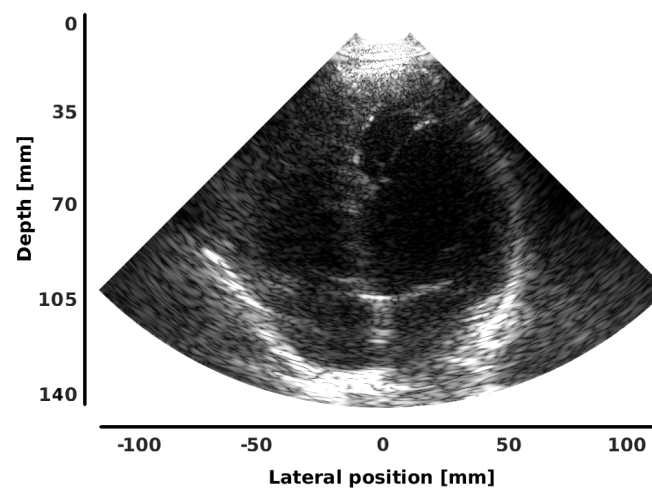
(b) Sectorial extension of Lu's method
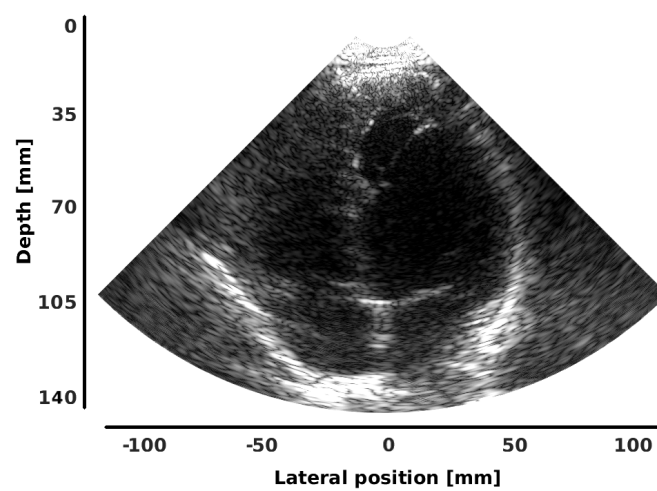
(c) Papadacci's method

Figure 6.13: *In vivo* experiments - Image reconstructed from (a) the proposed extension of UFSB method, (b) the proposed extension of Lu's method and (c) the spatial-based method of Papadacci using 32 DW with coherent compounding and without motion compensation.
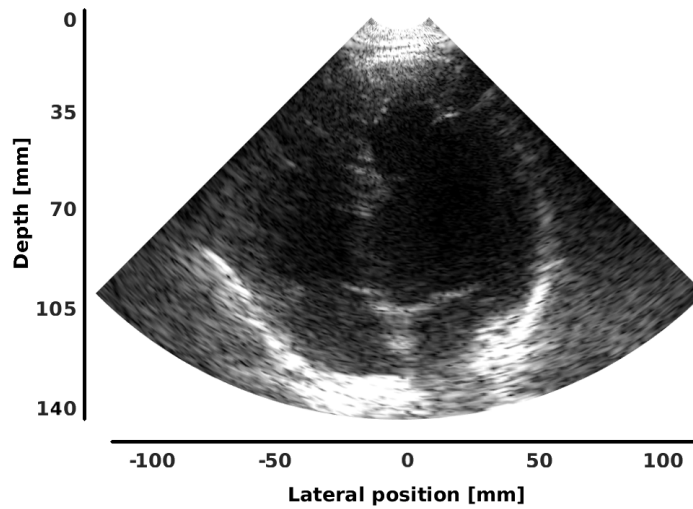
(a) Extension of Lu's method without MoCo
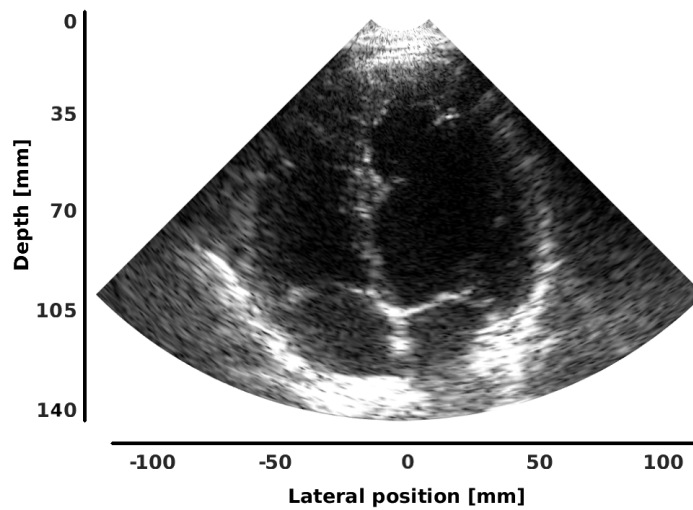
(b) Extension of Lu's method with MoCo

Figure 6.14: *In vivo* experiments - Motion compensation (MoCo) for high frame rate echocardiography of the left ventricle using the sectorial extension of Lu's method (a) without and (b) with MoCo.

64, 128 or 192), n_s the number of time samples (typically $\geq$ 1000-3000), n_x the number of samples along the x-axis for the reconstructed image (typically between 100 and 500) and n_ξ the number of angles used in reception for Bernard's method (this value was fixed to 170 in our experiments, the reader is refered to [Bernard *et al.* (2014)] for more details).

Complexity of Papadacci's method

The DAS method proposed by Papadacci *et al.* must retrieve $\lambda\,(n_x\,n_s\,n_e)$ interpolated data and perform $\lambda\,(n_x\,n_s)$ summations over n_e, λ being the ratio between the scanned sectorial area and the corresponding encompassing rectangle (with dimensions $n_x\,n_s$). For an angular aperture of $90°$, λ is defined between $[0.5, 1]$. The computational complexity of the method of Papadacci *et al.* thus corresponds to $O(n_x\,n_s\,n_e)$.

Complexity of the proposed extension of Lu's method

The sectorial extension of Lu's method requires two 2-D FFTs (complexity of $O(n_x\,n_s\,log(n_x\,n_s))$) and two times the computation of $(n_x\,n_s)$ interpolated values (one for the regridding step performed in the Fourier space and one for the spatial transformation introduced in this work). The computational complexity of the extension of Lu's method thus reduces to $O(n_x\,n_s\,log(n_x\,n_s))$ compared to the method of Papadacci.

Complexity of the proposed extension of UFSB method

The sectorial extension of UFSB method requires n_e 1-D FFTs (complexity of $O(n_e\,n_s\,log(n_s))$), one 2D FFT (complexity of $O(n_x\,n_s\,log(n_x\,n_s))$), the computation of $(n_\xi\,n_e\,n_s/2)$ multiplications for the delays applied in reception (the ratio of 2 being explained by the use of half of the spectrum) and two times the computation of $(n_x\,n_s)$ interpolated values (one for the regridding step performed in the Fourier space and one for the spatial transformation introduced in this work). The computational complexity of the extension of UFSB method thus corresponds to $O(n_\xi\,n_e\,n_s)$, making the extension of this method less attractive than for the extension of Lu's method.

The computational complexity thus reduces from $O(n_x\,n_s\,n_e)$ for the current state-of-the-art method of Papadacci *et al.* to $O(n_x\,n_s\,log(n_x\,n_s))$ for the proposed extension of the Fourier-based method of Lu.

6.5.3 Extension to temporal acquisitions with tissue motion

Tissue motion is an important source of artifact in ultrafast imaging. In particular, when the motion of the structures of interest between two consecutive firings is higher than $\lambda/8$, it is common to observe a weakening of the compounding effect if no particular strategy is applied. Several approaches have thus been proposed to tackle this problem, both on PW [Denarie *et al.* (2013)b] and DW [Poree *et al.* (2016)]. In this paper, we showed the feasibility of the application of the motion compensation algorithm developed

in [Poree *et al.* (2016)] on the images reconstructed from the proposed approach. This proves the accuracy of our technique and validates further the marginal effect of the error map presented in Section 6.2.

6.6   Summary

In this chapter, an explicit transformation for the extension of Fourier-based techniques to the reconstruction of sectorial images using DW has been presented. The key concept of the proposed formulation is based on the derivation of an equivalence in terms of travel time between a linear system based on PW and a sectorial one based on DW. In particular, we proposed an explicit spatial transformation which allows the reconstruction of wide angle images from different compounding schemes in transmission (*i.e.* the line transmit sequences described in Section 6.3.1 for stationary objects and the triangle transmit sequences in Section 3.3.2 for the *in vivo* heart). Results obtained from simulations and experiments revealed that the proposed extension of Lu's method produces competitive results with lower computational complexity when compared to conventional delay-and-sum technique and the generality of the derived space transformation no matter how the virtual source position moves.

<div align="right">

Chapter 7

</div>

3D Ultrafast Cardiac Imaging

In this chapter, the 2D Fourier-based methods for sectorial imaging described in Chapter 6 are extended for 3D cardiac imaging. To this aim, the UFSB PW imaging method proposed in Chapter 5 is firstly extended to 3D PW imaging. The space transformation derived in Section 6.2 is then extended to 3D by equating the travel time associated with PW and DW insonifications. Using the same formalism as in 2D, the corresponding Fourier-based DW imaging methods adapted to the firing of 3D DW are finally derived. Results obtained from numerical simulations show that the proposed 3D method reconstructs the same image quality as the one produced by spatial-based method, but with lower computational complexity as in 2D.

7.1 Introduction

Despite two dimensional echocardiography (2DE) is widespread in clinical routine for the evaluation of cardiac structures and functions, it presents fundamental limitations since 3D morphology and motion are analyzed from a set of 2D planes. Moreover, 2D acquisitions introduce variabilities in the angle plane of the heart, leading to potential geometrical measurement differences. To overcome these limitations, three dimensional echocardiography (3DE) was proposed with the first reconstruction of 3D ultrasound images of the heart in 1974 [Dekker *et al.* (1974)] and has experienced a rapid development from slow and labor-intense off-line reconstruction to real-time volumetric imaging [Hung *et al.* (2007), Mor-Avi and Lang (2010)]. However, as described in Section 1.1, the frame rate of 3DE is limited by the intrinsic speed of sound and the amount of firings needed to reconstruct a full volume. Although many approaches (*i.e.* parallel receive beamforming,

multi-line transmission, ECG gating) have been proposed to increase the frame rate for 3D cardiac imaging, a limited frame rate of around $10 \sim 40$ Hz is currently reached by the commercial equipment with a compromise between resolution and potential stitching artifacts [Perrin *et al.* (2012)a].

As described in the previous chapter for 2D, one potential solution is the use of 3D DW compared to the conventional beam focused approach in order to insonify the entire volume with only one firing. In this context, Provost *et al.* recently demonstrated the feasibility of compounding DW using a sparse virtual array located behind the probe to achieve high frame rates for 3D cardiac imaging [Provost *et al.* (2014)]. Their corresponding reconstruction method is based on the conventional delay and sum beamforming technique. In order to reduce the computational complexity, we thus extend the 2D Fourier-based DW imaging method in 3D. To this aim, we first describe the generalization of the method of Lu and the proposed UFSB for 3D PW imaging. The space transformation derived in Section 6.2 is then extended to 3D by explicitly taking into account the y-coordinate in the different travel time equations.

Although the Fourier sampling scheme between the method of Lu and UFSB is different, it has been shown in Chapter 5 that these two methods reconstruct close Fourier spectrum, resulting in a very similar image quality. In addition, we showed in Section 6.5.2 that the extension of Lu's method to sectorial acquisition presents the lowest computational complexity compared to the conventional DAS technique and the extension of UFSB. In this chapter, we thus only perform the comparison of the state-of-the-art DAS technique with the proposed 3D extension of the Fourier-based method of Lu. Part of the results given in this chapter were presented at the IEEE International Ultrasonic Symposium in 2016 [Zhang *et al.* (2016)].

7.2 Extension of the 2D Fourier-based sectorial imaging technique to 3D

As described in Chapter 6, the 2D Fourier-based sectorial imaging technique is implemented by applying the PW imaging methods to the received echoes after DW transmissions and following by an explicit space transformation. The key idea of this section is to extend this formalism to 3D acquisitions.

7.2.1 3D Fourier-based plane wave imaging methods

As shown in Figure 7.1, a 2D transducer located at $z = 0$ plane is excited to generate a PW with direction $\mathbf{n_e} = (\sin \zeta_T \cos \theta_T, \sin \zeta_T \sin \theta_T, \cos \zeta_T)$, where ζ_T is the polar angle and θ_T is the azimuthal angle of $\mathbf{n_e}$. For a given transmission, both ζ_T and θ_T are fixed. To steer such a PW, linear delays are applied to each transducer elements as follows:

$$d(x_E, y_E) = (x_E \sin \zeta_T \cos \theta_T + y_E \sin \zeta_T \sin \theta_T)/c \qquad (7.1)$$
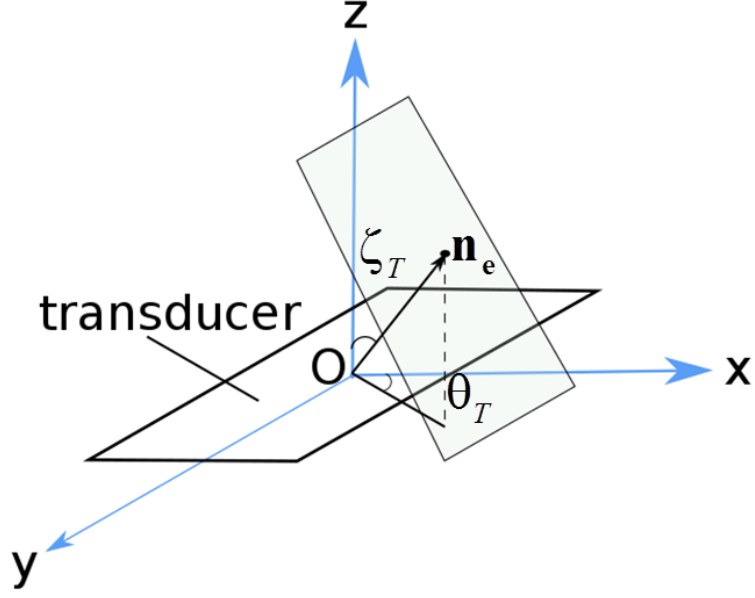
Figure 7.1: Illustration of the transducer geometry and steered PW front in 3D.

where $x_E \in (-D_x/2, D_x/2)$, $y_E \in (-D_y/2, D_y/2)$ are the element positions of the 2D transducer, D_x, D_y are the size of the transducer aperture in x and y directions. To make the system causal, an additional constant delay $dt = \frac{|D_x \sin \zeta_T \cos \theta_T| + |D_y \sin \zeta_T \sin \theta_T|}{2c}$ may be added to the delay function Eq.(7.1). From the transmission of such 3D PW, similar image formation as the ones for 2D can be employed. The 3D version of Lu and the UFSB methods are described in the following sections.

3D version of Lu's method for plane wave imaging

As described in [Cheng and Lu (2006)], the relationship between the 3D Fourier transform of measured echo signals at the transducer surface and the 3D spatial Fourier transform of the object function for a PW transmitted with a steered angle (ζ_T, θ_T) is given by (see Eq.(34) in [Cheng and Lu (2006)]):

$$
\begin{cases}
k'_x = k_x + k \sin \zeta_T \cos \theta_T \\[2mm]
k'_y = k_y + k \sin \zeta_T \sin \theta_T \\[2mm]
k'_z = \sqrt{k^2 - k_x{}^2 - k_y{}^2} + k \cos \zeta_T
\end{cases}
\tag{7.2}
$$

where k is the wavenumber while (k_x, k_y, k) and (k'_x, k'_y, k'_z) represent the coordinates of the Fourier spectrum of the received echoes and the object function, respectively. The inverse functions given in Eq.(7.2) can be computed as:

$$
\begin{cases}
k_x = k'_x - \dfrac{(k'^2_x + k'^2_y + k'^2_z) \sin \zeta_T \cos \theta_T}{2(k'_x \sin \zeta_T \cos \theta_T + k'_y \sin \zeta_T \sin \theta_T + k'_z \cos \zeta_T)} \\[3mm]
k_y = k'_y - \dfrac{(k'^2_x + k'^2_y + k'^2_z) \sin \zeta_T \sin \theta_T}{2(k'_x \sin \zeta_T \cos \theta_T + k'_y \sin \zeta_T \sin \theta_T + k'_z \cos \zeta_T)} \\[3mm]
k = \dfrac{k'^2_x + k'^2_y + k'^2_z}{2(k'_x \sin \zeta_T \cos \theta_T + k'_y \sin \zeta_T \sin \theta_T + k'_z \cos \zeta_T)}
\end{cases}
\tag{7.3}
$$

For the particular case of a horizontal PW in transmission $(\zeta_T, \theta_T) = (0,0)$ and the following relations can be obtained:

$$
\begin{cases}
k_x = k'_x \\[3mm]
k_y = k'_y \\[3mm]
k = \dfrac{k'^2_x + k'^2_y + k'^2_z}{2k'_z}
\end{cases}
\tag{7.4}
$$

From Eq.(7.3) and (7.4), the mapping between the Fourier transform of the echo signals in (k_x, k_y, k) space and the Fourier transform of the object function in (k'_x, k'_y, k'_z) space can be done with interpolation. After getting the spectrum of the object, by simply taking a 3D inverse Fourier transform, one can obtain the beamformed image.

3D extension of UFSB method for plane wave imaging

The UFSB method proposed in Chapter 5 can be easily extended to 3D. To this end, one has to take into account the y-direction in the fundamental relations between the Fourier transform of the received steered PW and the Fourier transform of the object function (Eq.(5.10) and Eq.(5.11)). For a 3D steered PW with direction $\mathbf{n_e} = (\sin \zeta_T \cos \theta_T, \sin \zeta_T \sin \theta_T, \cos \zeta_T)$, the following relations can be easily derived:

$$
\begin{cases}
k'_x = k(\sin \zeta_T \cos \theta_T + \sin \xi_i \cos \phi_j) \\[3mm]
k'_y = k(\sin \zeta_T \sin \theta_T + \sin \xi_i \sin \phi_j) \\[3mm]
k'_z = k(\cos \zeta_T + \cos \xi_i)
\end{cases}
\tag{7.5}
$$

and

$$
\begin{cases}
k &= \dfrac{{k'_x}^2 + {k'_y}^2 + {k'_z}^2}{2(k'_x \sin\zeta_T \cos\theta_T + k'_y \sin\zeta_T \sin\theta_T + k'_z \cos\zeta_T)} \\[2ex]
\xi_i &= \arctan \dfrac{2(k'_x \sin\zeta_T \cos\theta_T + k'_y \sin\zeta_T \sin\theta_T + k'_z \cos\zeta_T)\sqrt{{k'_x}^2 + {k'_y}^2}}{{k'_z}^2 - {k'_x}^2 - {k'_y}^2} \\[2ex]
\phi_j &= \arctan \dfrac{2k'_y(k'_x \sin\zeta_T \cos\theta_T + k'_y \sin\zeta_T \sin\theta_T + k'_z \cos\zeta_T) - ({k'_x}^2 + {k'_y}^2 + {k'_z}^2)\sin\zeta_T \sin\theta_T}{2k'_x(k'_x \sin\zeta_T \cos\theta_T + k'_y \sin\zeta_T \sin\theta_T + k'_z \cos\zeta_T) - ({k'_x}^2 + {k'_y}^2 + {k'_z}^2)\sin\zeta_T \cos\theta_T}
\end{cases}
\tag{7.6}
$$

where ξ_i and ϕ_j are the angles of steered PW in reception with the corresponding direction $\mathbf{n_r} = (\sin\xi_i \cos\phi_j, \sin\xi_i \sin\phi_j, \cos\xi_i)$. k is the wavenumber, (k'_x, k'_y, k'_z) represents the Fourier spectrum space of the object. In the particular case of an horizontal PW (where $\mathbf{n_e} = (0, 0, 1)$), the above spectrum remapping function can be simplified to:

$$
\begin{cases}
k &= \dfrac{{k'_x}^2 + {k'_y}^2 + {k'_z}^2}{2k'_z} \\[2ex]
\xi_i &= \arctan \dfrac{2k'_z \sqrt{{k'_x}^2 + {k'_y}^2}}{{k'_z}^2 - {k'_x}^2 - {k'_y}^2} \\[2ex]
\phi_j &= \arctan \dfrac{k'_y}{k'_x}
\end{cases}
\tag{7.7}
$$

Eq.(7.5) to Eq.(7.7) provide the fundamental relations between the temporal Fourier transform of the received signals and the Fourier transform of the object function derived from the UFSB method when the emitted field corresponds to a 3D steered PW. In this way, by using a sequence of varying steered angles (*i.e.* ξ_i and ϕ_j) in reception, this technique allows from the transmission of one single PW to radially recover the Fourier space of the insonified medium. By taking the 3D inverse Fourier transform of the sample object spectrum, the beamformed image can then be obtained.

7.2.2 3D extension of the space transformation introduced in Chapter 6

The key idea of this part is to extend the derived 2D space transformation in Chapter 6 to 3D, *i.e.* establish an equivalence in terms of travel time when either a 3D DW or a 3D PW is used in transmission by taking into account the y-coordinate. Indeed, such a relation would allow the reconstruction of a sectorial image from a 3D DW using the same formalism as the one we illustrated in Section 6.2.2.

Figure 7.2 shows a 2-D array transducer located at $z = 0$ plane, centered at $x = 0$ and $y = 0$, where each transducer element is positioned at $(x_E, y_E, 0)$. A transmitted 3D DW is obtained through the excitation of a virtual source located behind the probe and placed at (x_v, y_v, z_v) as shown in Figure 7.2a, where $x_v \in [-L_x/2, L_x/2]$, $y_v \in [-L_y/2, L_y/2]$ (L_x, L_y being the dimension of the probe along x and y directions). z_v is determined by

(a)

(b)
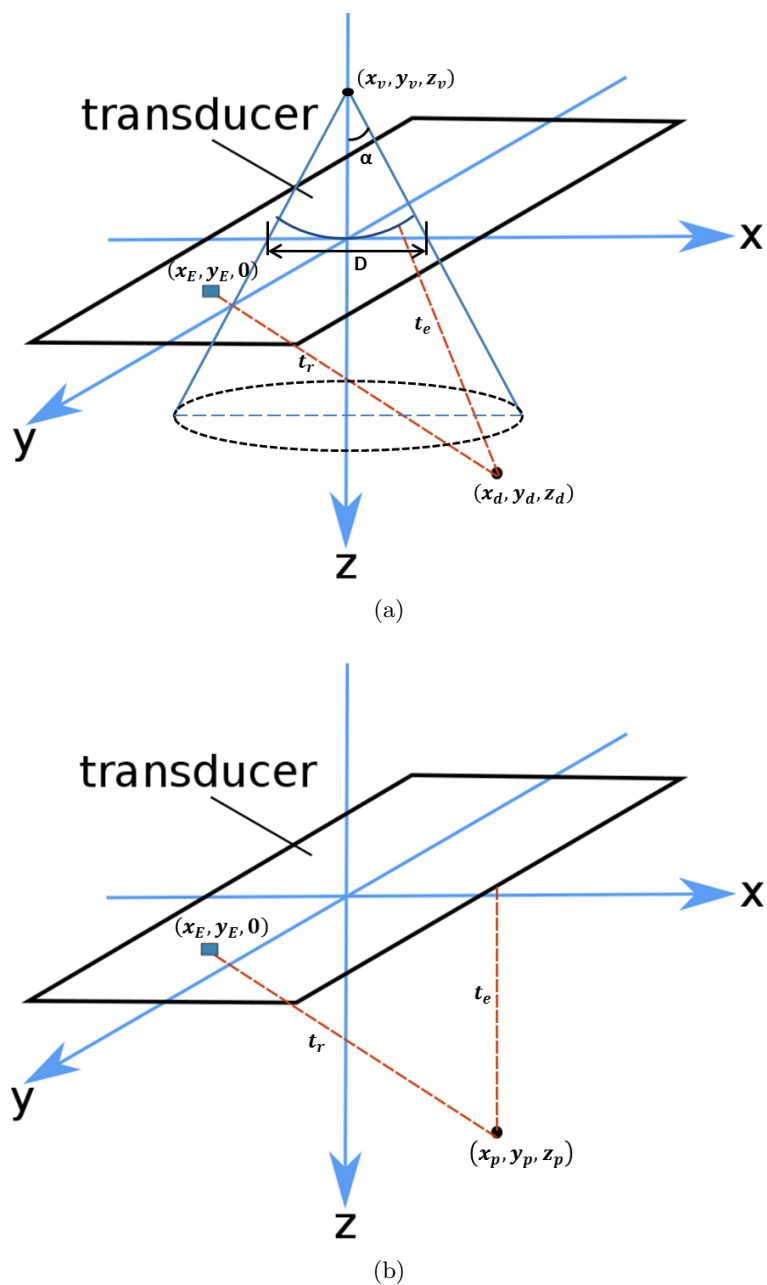
Figure 7.2: Illustration of the 3D travel time (represented by t_e and t_r) involved when either (a) a DW or (b) a PW is used in transmission. In both cases, $(t_e + t_r)$ corresponds to the time needed by the insonifying wave to reach a scatterer (black dot) and then come back to a specific transducer element.

the chosen angular aperture α and the sub-aperture width D as:

$$z_v = -\frac{D/2}{\tan(\alpha)} \tag{7.8}$$

The transmit delay of each transducer element associated with the virtual source po-

sition are then computed as:

$$\Delta(x_E, y_E) = \left(\sqrt{x_E^2 + y_E^2 + z_v^2} + z_v \right) \; / \; c \qquad (7.9)$$

where c represents the speed of sound, assumed to be homogeneous in the whole medium (1540 m/s in soft tissues). In this context, the travel time needed for a DW to reach a point scatterer positioned at (x_d, y_d, z_d) in the medium and to come back to a transducer element placed at $(x_E, y_E, 0)$ is given by:

$$\tau_d(x_E, y_E) = \left(\sqrt{(x_d - x_v)^2 + (y_d - y_v)^2 + (z_d - z_v)^2} \right.$$
$$\left. + \; z_v + \; \sqrt{(x_d - x_E)^2 + (y_d - y_E)^2 + z_d^2} \right) \; / \; c \quad (7.10)$$

In the case of a horizontal PW in transmission, the travel time needed to reach a point scatterer (x_p, y_p, z_p) and to come back to the same transducer element $(x_E, y_E, 0)$ is given by:

$$\tau_p(x_E, y_E) = (z_p + \sqrt{(x_p - x_E)^2 + (y_p - y_E)^2 + z_p^2} \;) \; / \; c \qquad (7.11)$$

By equating the first order Taylor approximation of Eq.(7.10) and Eq.(7.11) at $x_E = x_v$ and $y_E = y_v$, the following relation between (x_d, y_d, z_d) and (x_p, y_p, z_p) can be derived:

$$
\begin{cases}
x_p \approx \dfrac{(x_d - x_v)\left(\sqrt{(x_d-x_v)^2+(y_d-y_v)^2+(z_d-z_v)^2} + z_v + \sqrt{(x_d-x_v)^2+(y_d-y_v)^2+z_d^2}\right)}{z_d + \sqrt{(x_d-x_v)^2+(y_d-y_v)^2+z_d^2}} + x_v \\[3ex]
y_p \approx \dfrac{(y_d - y_v)\left(\sqrt{(x_d-x_v)^2+(y_d-y_v)^2+(z_d-z_v)^2} + z_v + \sqrt{(x_d-x_v)^2+(y_d-y_v)^2+z_d^2}\right)}{z_d + \sqrt{(x_d-x_v)^2+(y_d-y_v)^2+z_d^2}} + y_v \\[3ex]
z_p \approx \dfrac{z_d\left(\sqrt{(x_d-x_v)^2+(y_d-y_v)^2+(z_d-z_v)^2} + z_v + \sqrt{(x_d-x_v)^2+(y_d-y_v)^2+z_d^2}\right)}{z_d + \sqrt{(x_d-x_v)^2+(y_d-y_v)^2+z_d^2}}
\end{cases} \quad (7.12)
$$

and

$$
\begin{cases}
x_d \approx \dfrac{1}{2} \dfrac{(x_p - x_v)\left(z_v^2 - \left(z_p + \sqrt{(x_p-x_v)^2+(y_p-y_v)^2+z_p^2} - z_v\right)^2\right)}{z_v z_p - \left(z_p + \sqrt{(x_p-x_v)^2+(y_p-y_v)^2+z_p^2} - z_v\right)\left(\sqrt{(x_p-x_v)^2+(y_p-y_v)^2+z_p^2}\right)} + x_v \\[3ex]
y_d \approx \dfrac{1}{2} \dfrac{(y_p - y_v)\left(z_v^2 - \left(z_p + \sqrt{(x_p-x_v)^2+(y_p-y_v)^2+z_p^2} - z_v\right)^2\right)}{z_v z_p - \left(z_p + \sqrt{(x_p-x_v)^2+(y_p-y_v)^2+z_p^2} - z_v\right)\left(\sqrt{(x_p-x_v)^2+(y_p-y_v)^2+z_p^2}\right)} + y_v \\[3ex]
z_d \approx \dfrac{1}{2} \dfrac{z_p\left(z_v^2 - \left(z_p + \sqrt{(x_p-x_v)^2+(y_p-y_v)^2+z_p^2} - z_v\right)^2\right)}{z_v z_p - \left(z_p + \sqrt{(x_p-x_v)^2+(y_p-y_v)^2+z_p^2} - z_v\right)\left(\sqrt{(x_p-x_v)^2+(y_p-y_v)^2+z_p^2}\right)}
\end{cases} \quad (7.13)
$$

From Eq.(7.12) and Eq.(7.13) the following generic algorithm is thus proposed to reconstruct a 3D sectorial image: i) transmission of a DW using a standard 2D array; ii)

from the received echo, application of a Fourier-based method derived for 3D PW (*i.e.* Lu's method). Thanks to Eq.(7.12), one can see that the output of this step will reconstruct the desired ultrasound image but expressed in the (x_p, y_p, z_p) coordinate system; iii) application of the spatial transformation given through Eq.(7.13) which allows the reconstruction of the image in the conventional Cartesian space.

As introduced in Section 6.2.2, during the reconstruction process of the Fourier-based PW imaging methods, we need to interpolate the Fourier spectrum of the collected data on a regular grid and such interpolation results in a decrease of the intensity of the reconstructed image along depth and along the polar angle. Moreover, this decrease of intensity is intrinsically worse in 3D than in 2D. To take this aspect into account, we thus applied an intensity correction of 1-dB/MHz/cm along the radial distance and along the polar angle for the Fourier-based technique.

7.3   3D diverging wave transmission scheme study

In this section, the coherent summation of multiple 3D DW is performed analytically to investigate the synthetic focus achieved in transmit. Each transmitted 3D DW is defined by the position of a virtual source located behind the probe.

Let us consider a virtual array of $M \times N$ point sources located behind the probe at positions $r_{m,n} = (x_m, y_n, z_0)^T$, where z_0 is kept constant for all the sources, x_m varies between $-a$ and a in the x direction, while y_m varies between $-b$ and b in the y direction. $x_m = mp_x$ and $y_n = np_x$, p_x and p_y being the pitch of the virtual array in the x and y directions. In the case of a coherent summation over the bandwidth (k_1, k_2) of the acoustic fields generated by the DW defined above at the synthetic focal point $r_c = (x_c, y_c, z_c)^T$, the expression of the corresponding field $\Phi(r)$ is given by:

$$\Phi(r) = \int_{k_1}^{k_2} A(k) \sum_{m=-a}^{a} \sum_{n=-b}^{b} \frac{e^{jk|r-r_{m,n}|}}{|r - r_{m,n}|} \cdot e^{-jk|r_c-r_{m,n}|} \mathrm{d}\,k \qquad (7.14)$$

where $e^{-jk|r_c-r_{m,n}|}$ is the phase correction needed to achieve the coherent summation at point r_c and $A(k)$ is the amplitude. In the far-field, near the central line $x = 0$ and $y = 0$, one can assume that $|z_c - z_0| \gg |x - x_m|$ and $|z_c - z_0| \gg |y - y_n|$. As proposed in [Papadacci *et al.* (2014)], the amplitude can then be approximated as:

$$|r - r_{m,n}| = \sqrt{(x - x_m)^2 + (y - y_n)^2 + (z - z_0)^2}$$
$$= (z - z_0)\sqrt{1 + \frac{(x - x_m)^2}{(z - z_0)^2} + \frac{(y - y_n)^2}{(z - z_0)^2}}$$
$$\approx (z_c - z_0) = F \qquad (7.15)$$

By taking the two first terms of the truncated binomial expansion $\sqrt{1 + a} = 1 + \frac{1}{2}a - \frac{1}{8}a^2 + o(a^2)$, an approximation can also be made on the phase:

$$|r - r_{m,n}| \approx (z - z_0) \left[1 + \frac{1}{2} \frac{(x - x_m)^2}{(z - z_0)^2} + \frac{1}{2} \frac{(y - y_n)^2}{(z - z_0)^2} \right]$$

$$= F + \frac{1}{2} \frac{(x - x_m)^2}{F} + \frac{1}{2} \frac{(y - y_n)^2}{F} \tag{7.16}$$

Therefore,

$$\Phi(x, y) \approx \int_{k_1}^{k_2} A(k) \frac{1}{F} \sum_{m=-a}^{a} \sum_{n=-b}^{b} e^{jk(F + (x-x_m)^2/2F + (y-y_n)^2/2F)}$$

$$\cdot \, e^{-jk(F + (x_c-x_m)^2/2F + (y_c-y_n)^2/2F)} \mathrm{d}\, k \tag{7.17}$$

The above equation can be rearranged as:

$$\Phi(x, y) \approx \int_{k_1}^{k_2} A(k) \frac{1}{F} e^{j(k/2F)(x^2 - x_c{}^2 + y^2 - y_c{}^2)} \sum_{m=-a}^{a} e^{j(k/F)x_m(x_c - x)}$$

$$\cdot \sum_{n=-b}^{b} e^{j(k/F)y_n(y_c - y)} \mathrm{d}\, k \tag{7.18}$$

For the virtual array defined at the begining of this section, we have $x_m = mp_x, y_n = np_y$ and $\Phi(x, y)$ thus further simplifies to:

$$\Phi(x, y) \approx \int_{k_1}^{k_2} A(k) \frac{1}{F} e^{j(k/2F)(x^2 - x_c{}^2 + y^2 - y_c{}^2)} \sum_{m=-a}^{a} e^{j(k/F)mp_x(x_c - x)}$$

$$\cdot \sum_{n=-b}^{b} e^{j(k/F)np_y(y_c - y)} \mathrm{d}\, k \tag{7.19}$$

The last two summation terms involved in Eq.(7.19) correspond to classical geometrical series that have explicit expressions. $\Phi(x, y)$ can thus be written as:

$$\Phi(x, y) \approx \int_{k_1}^{k_2} A(k) \frac{1}{F} e^{j(k/2F)(x^2 - x_c{}^2 + y^2 - y_c{}^2)} \frac{\sin(kp_x(x - x_c)(2a + 1)/2F)}{\sin(kp_x(x - x_c)/2F)}$$

$$\cdot \frac{\sin(kp_y(y - y_c)(2b + 1)/2F)}{\sin(kp_y(y - y_c)/2F)} \mathrm{d}\, k \tag{7.20}$$

In the particular case of the monochromatic far-field approximation, the magnitude of

the field can finally be expressed as:

$$|\Phi(x,y)| \approx A(k) \frac{1}{F} \left| \left(\frac{\sin(kp_x(x-x_c)\,M/2F)}{\sin(kp_x(x-x_c)/2F)} \right) \left(\frac{\sin(kp_y(y-y_c)\,N/2F)}{\sin(kp_y(y-y_c)/2F)} \right) \right| \qquad (7.21)$$

where $M = (2a+1)$ and $(N = 2b+1)$ are the number of virtual sources along x and y directions, respectively.

This last equation allows the investigation of the width of the main lobe along with the positions of the associated side lobes for the 3D case. Figure 7.3 shows an example of the wave pressure computed from Eq.(7.21) with $M \times N = 9 \times 9$ DW with a center frequency of 3 MHz.
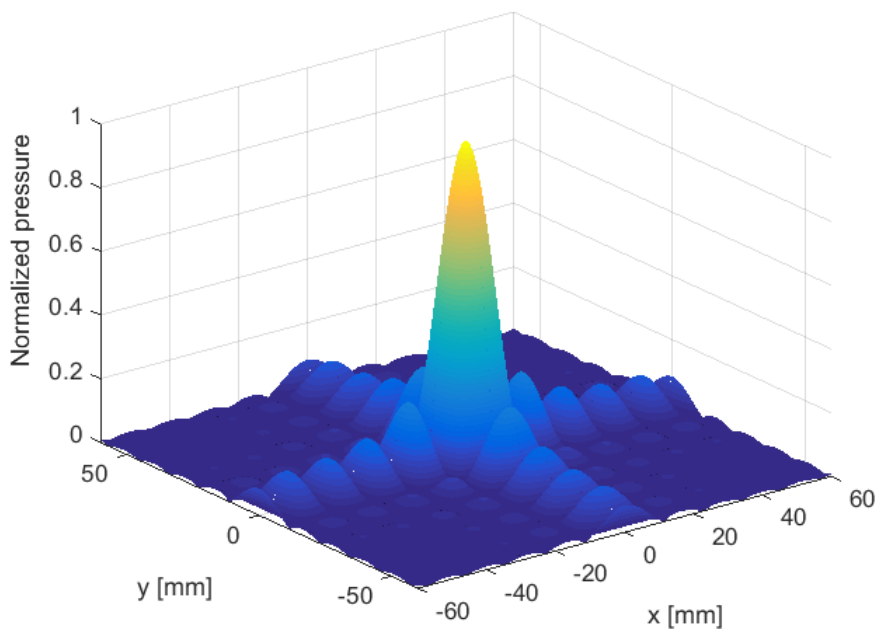
Figure 7.3: An example of the compounded wave pressure computed from Eq.(7.21) with 9×9 DW with a center frequency of 3 MHz. The wave is displayed as a map of the normalized pressure amplitude at 60-mm depth.

Working with the spatial variables (X, Y) centered on the synthetic focal point (x_c, y_c), the pressure field $\Phi(X, Y)$ vanishes when

$$X = \frac{\lambda F}{M p_x} l, \quad l \in Z^* \qquad (7.22)$$

or

$$Y = \frac{\lambda F}{N p_y} l, \quad l \in Z^* \qquad (7.23)$$

where $\lambda = 2\pi/k$ corresponds to the standard expression of the wavelength. From the above two equations, the width W_x and W_y of the main lobe along x and y directions can

Miaomiao ZHANG

be easily derived:

$$W_x = 2\frac{\lambda F}{Mp_x} = 2\frac{\lambda F}{W_{vx}}\frac{M-1}{M} \approx 2\frac{\lambda F}{W_{vx}} \tag{7.24}$$

and

$$W_y = 2\frac{\lambda F}{Np_y} = 2\frac{\lambda F}{W_{vy}}\frac{N-1}{N} \approx 2\frac{\lambda F}{W_{vy}} \tag{7.25}$$

where W_{vx} and W_{vy} are the width of the virtual array in x and y directions, respectively. Compared to Eq.(6.7) obtained in the 2D case, one can see that the width of 3D main lobe computed along the x and y directions shares the same properties as in 2D, *i.e.* its value decreases with the total aperture of the virtual array. We thus propose to extend in 3D the dichotomous transmission scheme detailed in Chapter 4. In particular, by maintaining the maximum width of the virtual array W_{vx} and W_{vy} for varying number of transmissions in x and y directions, the reconstructed images will roughly keep the same resolution, making this approach more attractive than the conventional scheme used in [Provost *et al.* (2014)]. Figure 7.4 illustrates the dichotomous scheme extended to the 3D case.

(a) 1   (b) 5   (c) 9   (d) 25   (e) 81
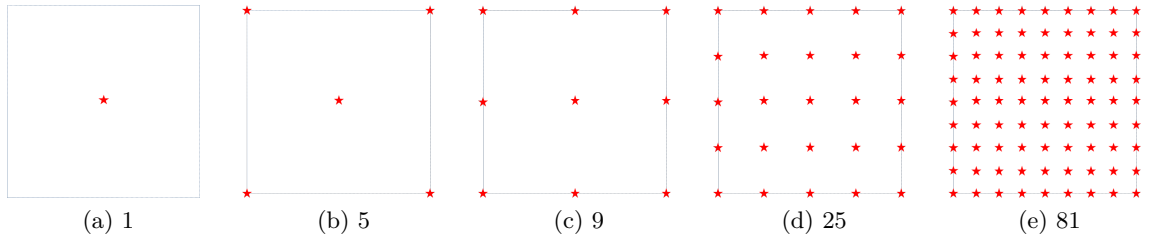
Figure 7.4: Illustration of the extension in 3D of the dichotomous scheme used for the compounding of 3D DW. (a)-(e) The virtual array for different number of virtual sources (*i.e.* 1, 5, 9, 25, 81). The red stars show the position of the virtual sources. The rectangular box represents the border of the virtual array.

7.4 Numerical simulations

In this section, numerical simulations were performed to validate and assess the performances (in terms of lateral resolution and image contrast) of the extended Fourier-based method of Lu for 3D DW imaging. For all the tests, we used the transmission scheme described in the previous section. The proposed extension method of Lu was compared with the current state-of-the-art ultrafast 3D DW imaging algorithm, *i.e.* the method of Provost *et al.* [Provost *et al.* (2014)]. A 2D matrix array of 32×32 elements with a center frequency of 3-MHz (100% bandwidth) and a 0.3 mm pitch was implemented using Field II [Jensen and Svendsen (1992), Jensen (1996)]. The sampling frequency was set to 50 MHz. No apodization was used in both transmission and reception. Each reconstructed image was obtained from the following protocol: i) raw-data signals were acquired using

DW with different virtual source point positions; ii) those signals were processed either following the proposed extension framework or using the method of Provost in order to obtain the compounded image; iii) the corresponding envelope image was derived through a Hilbert transform and normalized; iv) the envelope image was then gamma-compressed using $\gamma = 0.3$ as in [Garcia *et al.* (2013)] and finally converted to 8-bit grayscale to get the final B-mode image.

7.4.1 Lateral resolution

To verify the derived space transformations of Eq. (7.12) and (7.13), a numerical phantom composed by a set of distinct point scatterers was used. Figure 7.5 displays the orthogonal slices along $x - z$ direction of the volumetric images reconstructed from the proposed extension of Lu's method (Figure 7.5a) and the current DAS method of Provost *et al.* (Figure 7.5b) using 81 DW, respectively. The red circles correspond to the real position of the scatterers. From these figures, one can see that the extended method of Lu in 3D reconstructed the PSFs at the correct position. The 3D spatial transform did not introduced any geometrical distortion. We can also observe that the image obtained using the extension of Lu's method present slightly higher intensity with depth, which is due to the intensity correction that we applied to limit the Fourier interpolation artifacts.

(a) Extension of Lu's method in 3D   (b) Provost's method
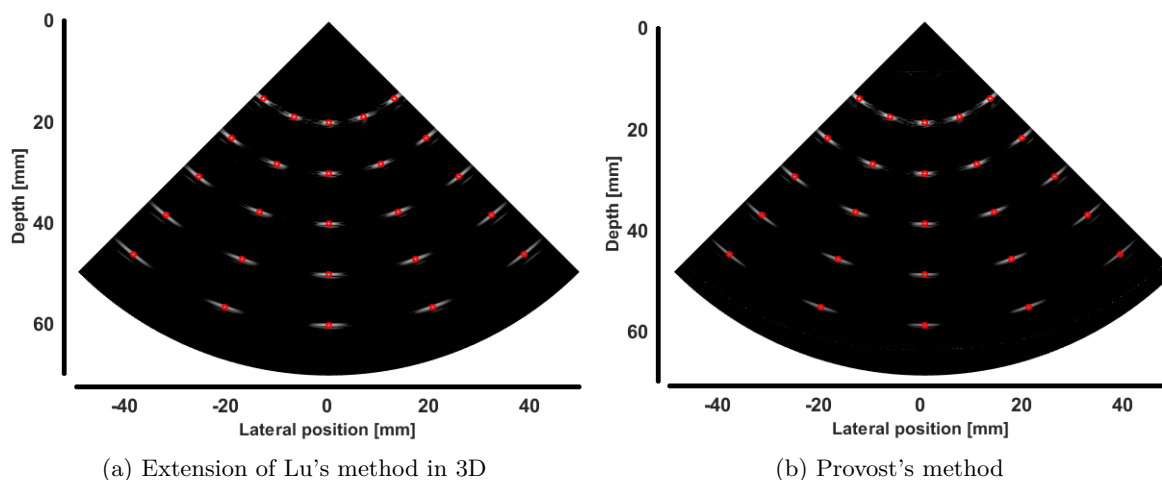
Figure 7.5: Orthogonal slices along $x - z$ direction of the reconstructed point scatterers phantom from (a) the proposed extension of Lu's method and (b) the method of Provost *et al.* using 81 DW. The red circles correspond to the real positions of the point scatterers involved in the simulation.

Figure 7.6 investigates the influence of the number of DW on the lateral resolution using the different reconstruction techniques and for different depths at the middle (azimuth angle of 0°) and the border (azimuth angle of 40°) of the image. The lateral resolution was estimated by measuring the full width at half maximum (FWHM) of the real envelopes of the beamformed image (no gamma-compression was used here). First, it can be seen that the two methods produced similar image quality whatever the depth and the number

(a) Extension of Lu's method in 3D

(b) Provost's method

(c) Extension of Lu's method in 3D
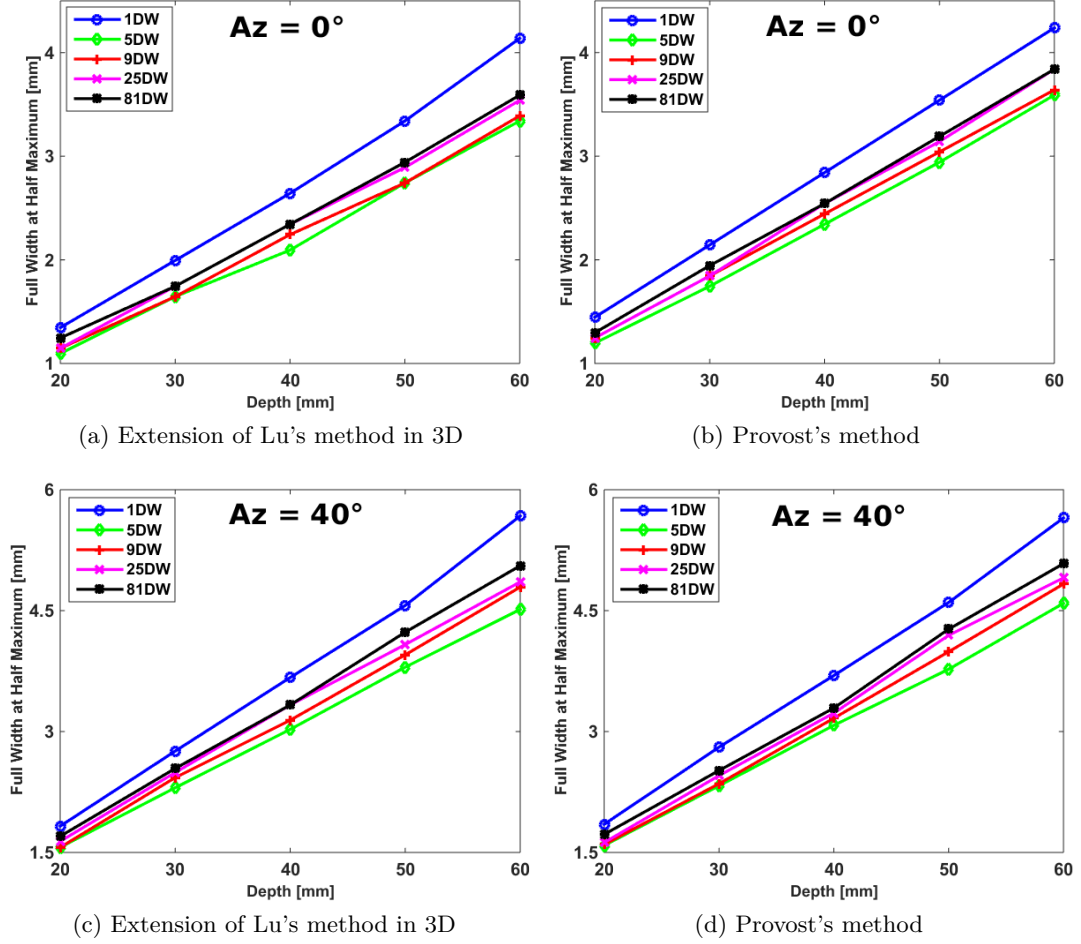
(d) Provost's method

Figure 7.6: Resolution measurements as a function of depth for different number of DW involved in the compounding scheme using (left) the extension of Lu's method in 3D and (right) the DAS technique proposed by Provost *et al.* [Provost *et al.* (2014)]. The lateral resolutions are computed at 20-mm, 30-mm, 40-mm, 50-mm and 60-mm in (top) the middle of the image (azimuth angle of 0°) and (bottom) at the edge of the image (azimuth angle of 40°).

of involved DW for both the middle and the edge of the image. In particular, it can be observed that the lateral resolution degraded with an increase of the azimuth angle. For instance, at 60-mm depth, the lateral resolution goes from values around 4.1-mm in the middle of the image to values around 5.7-mm at the edge for the transmission of 1 DW. This phenomenon can be explained by the limited opening angle of the effective aperture for the measurement involving only 1 DW and by the fact that the region where the different DWs contribute to the image pixels is optimal in the middle of the image for the measurements involving more than 1 DW. It is also interesting to note that the lateral resolution improved quickly for 5 DW and then degraded a little after increasing the number of DW. This behavior can be explained by the chosen transmission scheme described in Section 7.3, which has the same tendency as in 2D, *i.e.* for a fixed width of the virtual array, the lateral resolution degrades a little bit by increasing the number of

DW (from five to more firings in this case) and then tends to stabilize to the optimal value (see Figure 6.6 for 2D case).

7.4.2 Image contrast

The quality of the reconstructed image was then investigated from the contrast ratio (CR) measurements performed through numerical phantoms (*i.e.* a homogeneous medium with high density of scatterers, 10 per resolution cell with an anechoic cyst of diameter 10-mm lying at 40-mm and 80-mm depth in the middle and the border of the image). Figure 7.7 investigates the improvement of the image contrast with the number of DW. From Figure 7.7a and 7.7b it can be seen that the two methods produced similar image quality. Figure 7.7c and 7.7d display the contrast values measured for varying number of DW involved in the compounding scheme for different depths and azimuth angles. The two methods yielded very close results, the CR measurements showing same tendency with an increasing number of DW whatever the depth and the number of DW. In particular, the two methods produce same CR values at the border (azimuth angle of 40°) and present 0.8 dB of difference at the middle of the image (azimuth angle of 0°), which could be considered as negligible. A better CR score was obtained at 40-mm which can be explained by the intrinsic decrease of the transmit ultrasound pressure with depth which induces lower contrast. CR values also decreased a little with the azimuth angle. This can be explained by the fact that the region where different DW contribute to the image pixels is optimal at the middle of the image. The limited opening angle of the effective aperture may also reinforce this phenomenon. It is also interesting to note that the image contrast increased rapidly with small number of DW (*i.e.* 5, 9, or 13) and reaches a plateau after 25 DW.

7.5 Discussion

In this chapter, the feasibility of using Fourier-based method for 3D sectorial imaging was investigated. In particular, an explicit transformation has been proposed, which allows the extension of the existing Fourier-based methods (*e.g.* Lu's method), initially proposed for planar acquisition, to the reconstruction of sectorial images with wide angle using 3D DW. Simulation results showed that the proposed extended Fourier-based approach produces competitive results compared to the state-of-the-art DAS method proposed by Provost *et al.* [Provost *et al.* (2014)].

One of the strong interest of Fourier-based technique compared to the DAS method concerns the reduction of the computational complexity as shown in Chapter 6. We thus investigated in this section the computational ratio between the different techniques in 3D. Let n_{ex} and n_{ey} denote the number of elements in x and y directions of the 2D array, n_s the number of time samples, n_x and n_y the number of samples along the x-axis and y-axis for the reconstructed image. The proposed extension of Lu's method has a computational complexity of $O(n_x n_y n_s \log(n_x n_y n_s))$ while the DAS method has a computational

(a) Extension of Lu's method in 3D

(b) Provost *et al.*

(c) Az = 0°

(d) Az = 40°
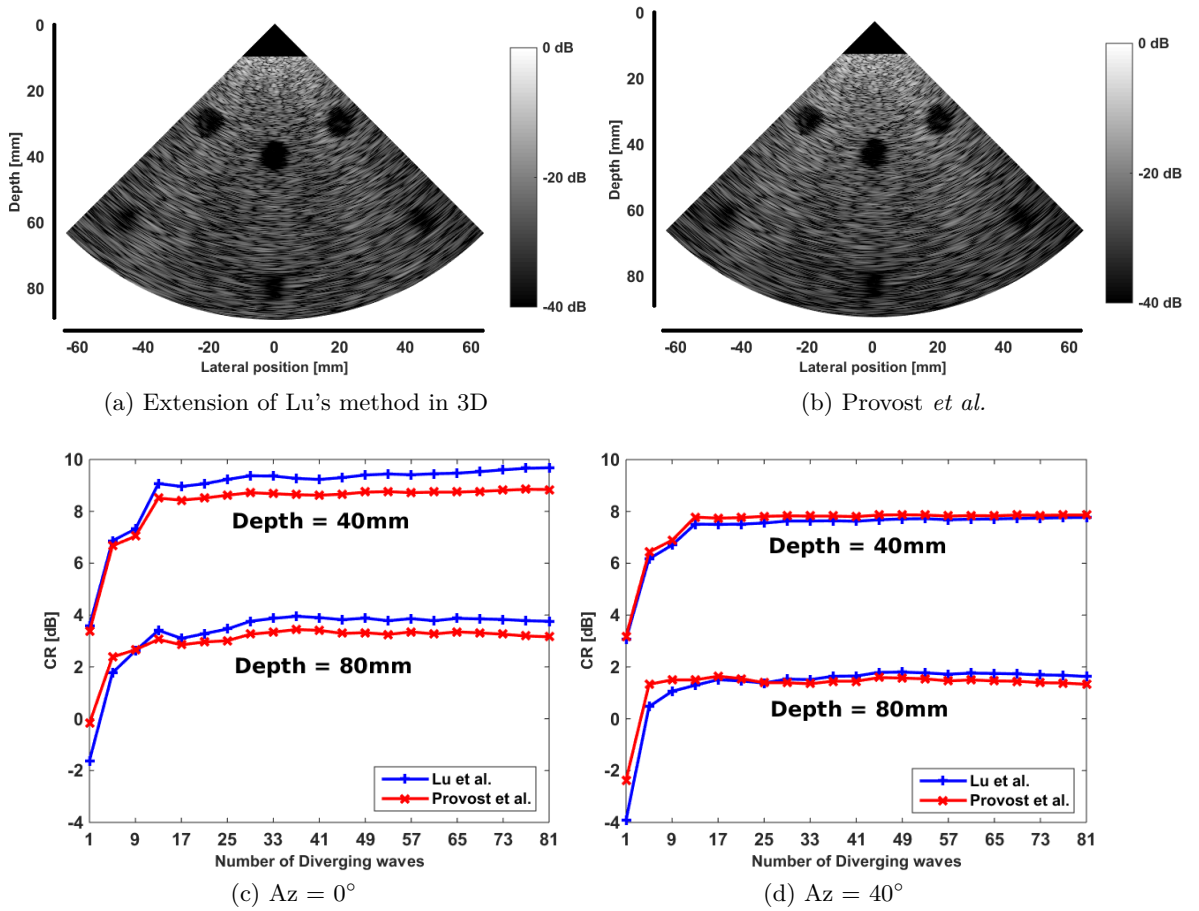
Figure 7.7: Orthogonal slices along $x - z$ direction of the reconstructed numerical phantom from (a) the proposed extension of Lu's method and (b) the method of Provost *et al.* using 81 DW. Contrast ratio (CR) as a function of the number of DW for the above two methods in (c) the middle of the image (azimuth angle of 0°) and (d) the border of the image (azimuth angle of 40°).

complexity of $O(n_x n_y n_s n_{ex} n_{ey})$. Interestingly, in the 3D case, the computational ratio between the proposed method and the DAS technique thus goes up to $n_{ex} n_{ey}/\log(n_x n_y n_s)$, making the interest of our approach even more stronger than in 2D.

7.6 Summary

In this chapter, the formulation proposed in Chapter 6 was extended to 3D. Computer simulations were performed to validate the ability of the proposed formulation to reconstruct images without geometrical distortion. Measurements of the lateral resolution and contrast performed from numerical phantoms showed the ability of the proposed method in reconstructing same image quality as the one obtained from the conventional DAS technique, but with a significant reduction of the computational complexity.

Miaomiao ZHANG

IV   Conclusions and Perspectives

Chapter 8

Conclusions and Perspectives

8.1 Conclusions

The goal of this PhD was to propose a method for ultrafast sectorial imaging in echocardiography based on DW insonification and Fourier domain reconstruction.

First of all, we investigated the influence of the transmission scheme on image quality using PW in transmission. We presented a dichotomous transmission scheme designed for linear acquisition based on an analytical study of the synthetic pressure field generated during compounding scheme. In particular, we showed that this transmission scheme can improve the quality of the reconstructed images at a constant frame rate using the current state-of-the-art reconstruction algorithms. The quality of the reconstructed images was evaluated in terms of resolution and contrast from both simulations and phantom experiments.

We then proposed a new Fourier-based reconstruction method by exploiting the well-known Fourier slice theorem when PW are used in transmission. In contrary to the existing Fourier-based techniques, this method allows the reconstruction of the object spectrum radially in the Fourier domain. This new technique was evaluated and compared to the existing PW imaging methods from computer simulations as well as from *in vitro* and *in vivo* experiments. The obtained results revealed the ability of the proposed approach to reconstruct ultrasound images with the same quality as the one obtained from the state-of-the art techniques.

We then derived an explicit transformation to extend the 2D Fourier-based methods from linear to sectorial imaging from the use of DW in transmission. This transformation was obtained by establishing an isomorphism in terms of travel time when either a DW

or a PW is used in transmission. Results obtained from both simulations and *in vivo* experiments showed that the application of the introduced spatial transformation to the method of Lu allows the reconstruction of images with the same quality as the one obtained from the conventional delay and sum technique from the transmission of DW, but with lower computational complexity.

Finally, the proposed 2D Fourier-based ultrafast sectorial imaging formulation was extended to 3D. This was done by explicitly taking into account the *y*-coordinate in the equations involved when either DW or PW are exploited. From the analytical study of the synthetic pressure field resulting from the combination of a set of 3D DW, we introduced a dichotomous scheme to improve the quality of the reconstructed images at a constant frame rate compared to the conventional transmission approach. Based on preliminary results derived from computer simulations, we showed that the combination of the dichotomous scheme with the 3D extension of the Fourier-based method of Lu produced competitive image quality compared to the delay and sum technique but with a much lower computational complexity.

8.2 Perspectives

In this thesis, we derived a Fourier-based formalism for 3D ultrafast ultrasound imaging using DW in transmission. One direct improvement of the proposed approach is the use of nonuniform Fast Fourier Transform (NUFFT) which would allow a reduction of the artifact introduced during the spectrum interpolation step, as described in [Kruizinga *et al.* (2012)].

Since the transmitted energy of a 3D DW decreases as the cube of depth, the signal to noise ratio of the image decreases significantly for large depths. It would thus be important to investigate methods that could limit this degrading effect. Several approaches would be interesting to investigate, among them the design of dedicated post-processing steps such as regularization [Carrillo *et al.* (2015)] or the use of multiplane wave-like transmission scheme [Tiran *et al.* (2015)].

In this manuscript, the properties of the 3D version of the proposed reconstruction method was assessed from numerical simulations. More experiments on both *in vitro* phantoms and *in vivo* ultrasound data volumes are under investigation. In the particular case of cardiac imaging, the 3D displacement of the heart will cause unavoidable motion artifacts that will have a strong impact during the compounding steps. Further investigations have thus to be done in order to develop a dedicated motion compensation algorithm well adapted for 3D cardiac imaging. For instance, the extension in 3D of the MoCo algorithm proposed by Poree *et al.* implies the extension of the tissue doppler and the triangular sequence (see Section 3.3.2 for more details) in 3D. Once high quality 3D cardiac volumes with competitive hardware costs will be reached, it would be interesting to further implement this solution on commercial ultrasound machines for clinical applications to serve the physician's diagnosis.

Finally, it is very interesting to assess myocardial mechanical properties from the developed ultrafast cardiac imaging technique, such as cardiac displacement and strain, fiber orientations or vector flow imaging. Additional studies will be conducted to assess the impact of our technique on the measurement of corresponding parameters.

Miaomiao ZHANG

Résumé en français

Résumé en français

I. Introduction

Chapitre 1. Introduction

1.1 Motivation

L'échocardiographie en trois dimensions (3DE) est une modalité d'imagerie sûre, non-invasive, qui est utilisée pour évaluer la fonction et l'anatomie cardiaque en routine clinique. Cette technique améliore la précision de l'évaluation des volumes des cavités cardiaques par rapport à l'imagerie 2D et fournit une vue réaliste des valves cardiaques et des anomalies congénitales. Elle correspond de ce fait à l'une des méthodes les plus prometteuses pour le diagnostic de la cardiopathie valvulaire [Lang *et al.* (2006), Monaghan (2006), Shiota (2014)]. Toutefois, la limitation de la cadence d'acquisition représente une réelle limitation pour l'utilisation de la 3DE dans la pratique clinique quotidienne. Effectivement, en imagerie échographique conventionnelle, les volumes sont obtenus par transmission séquentielle de faisceaux émis dans des directions différentes afin de couvrir un secteur de l'image souhaitée. En supposant que la seule limite à la fréquence d'imagerie est la propagation des ondes ultrasonores, le temps nécessaire pour construire une image est donc proportionnel au nombre de lignes, à la profondeur d'image et à la vitesse du son. Pour les tissus mous humains, la vitesse de propagation des ondes est approximativement de 1540 m/s. Avec une profondeur de 200 mm, il faut environ 260 μs à un seul faisceau pour se propager dans le corps humain et revenir. Cela permet 3850 transmissions par seconde. Pour l'imagerie cardiaque, l'acquisition d'un seul volume avec une qualité raisonnable exige des milliers de faisceaux pour imager le cœur avec suffisamment de détails, ce qui conduit à un fréquence d'imagerie d'environ 1 volume per seconde (Figure VF.1a), ce qui se révèle insuffisant en pratique. De ce fait il est clair qu'avec des cadences d'imagerie aussi faibles la 3DE conventionnelle, telle que décrite ci-dessus, n'est pas en mesure de produire en un seul cycle cardiaque des images permettant l'évaluation de la dynamique du cœur.

Il y a plusieurs façons de traiter le compromis entre la fréquence d'acquisition et la qualité d'image. Une possibilité consiste à utiliser la technique dite de formation de voie

parallèle en réception pour générer plusieurs faisceaux d'imagerie en parallèle en transmettant des faisceaux plus larges [Shattuck *et al.* (1984)], ce qui peut être obtenu en réduisant l'ouverture d'émission [Von Ramm *et al.* (1991), Pavy (1993), Hergum *et al.* (2007)] et en transmettant des faisceaux non focalisés ou défocalisés [von Ramm *et al.* (1984), Hasegawa and Kanai (2011)] (Figure VF.1b). Une autre façon d'augmenter la fréquence d'imagerie, appelée "Multi-Line Transmit" (MLT) est d'utiliser plusieurs faisceaux d'émission. Avec cette technique, plusieurs impulsions ultrasonores focalisées dirigées dans différentes directions latérales sont transmises et le même nombre de lignes sont reconstruites simultanément [Shirasaka (1989), Mallart and Fink (1992)]. En utilisant la MLT, la fréquence d'image peut être M fois plus rapide, M étant le nombre d'impulsions parallèles de chaque transmission. La troisième technique correspond à synchroniser l'acquisition avec le signal ECG [Brekke *et al.* (2007)] pour acquérir des sous-volumes lors de cycles cardiaques différents. Ceci est possible car l'activité cardiaque est un processus cyclique. Avec ce procédé, les sous-volumes acquis lors de battement cardiaques consécutifs sont concaténés pour former un volume complet ce qui permet d'augmenter la taille du volume imagé tout en maintenant la fréquence d'imagerie (Figure VF.1c).

(a)   (b)   (c)
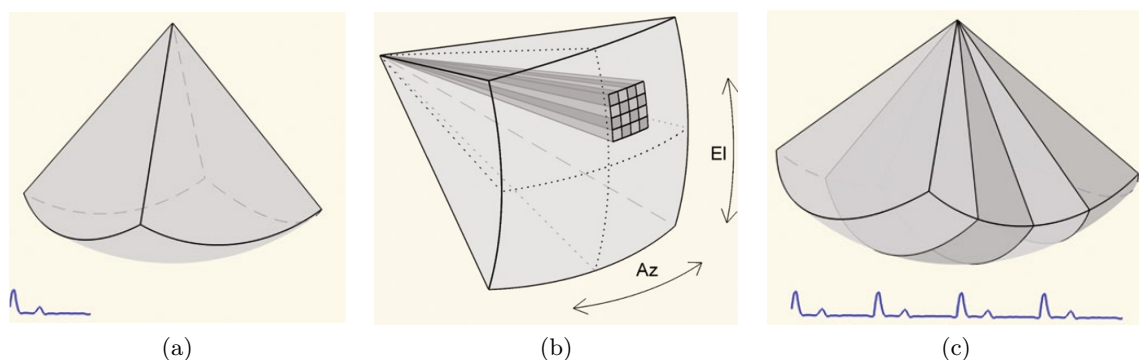
Figure VF.1: (Figure 2.1 and 2.3 dans [Rabben (2010)]) (a) Imagerie 3D en temps réel: un volume couvrant 60x60 degrés est acquis en temps réel. (b) Dans la formation de voies 3D, les faisceaux sont orientés dans les directions azimutale (Az) et d'élévation (El) en utilisant tous les éléments de la sonde matricielle 2D. En plus de la commande électronique, les systèmes 3D actuels sont capables d'effectuer la formation de voie en réception en parallèle. Dans ce cas, le système transmet un faisceau large et reçoit sur plusieurs canaux de réception (dans ce cas 16 éléments fonctionnent en réception). (c) Imagerie 3D synchronisée sur l'ECG: les sous-volumes correspondant à quatre battements cardiaques consécutifs sont concaténés pour obtenir un volume global couvrant 80x80 degrés.

Plusieurs approches sont également proposées pour augmenter la fréquence d'acquisition de volumes échographiques 3D [Perrin *et al.* (2012)b, Skaug *et al.* (2014)], en réduisant le nombre de transmissions. Cependant, la fréquence d'imagerie obtenue en utilisant ces méthodes est encore limitée et insuffisante pour effectuer la mesure du mouvement cardiaque et du flux sanguin sur la totalité du volume. Pour réduire de manière significative le nombre de transmissions, un concept différent a été proposé, basé sur un plus petit nombre d'ondes ultrasonores non-focalisées en transmission pour insonifier l'ensemble du milieu [Tanter and Fink (2014)]. Ce type d'imagerie est quelques fois appelé échographie ultra-rapide. La sommation cohérente des images ultrasonores acquises à chaque transmission permet une focalisation synthétique dans l'image complète, comme en imagerie par synthèse d'ouverture [Jensen *et al.* (2006)b]. Plusieurs approches ont été pro-

posées et validées en 2D à partir de ce concept en utilisant des emissions par ondes planes (PW) [Lu (1997), Cheng and Lu (2006), Montaldo *et al.* (2009), Garcia *et al.* (2013)] et par ondes divergentes (DW) [Hasegawa and Kanai (2011), Papadacci *et al.* (2014)] pour différentes applications, telles que l'élastographie [Montaldo *et al.* (2009)] et l'imagerie cardiaque [Hasegawa and Kanai (2011), Papadacci *et al.* (2014)]. Très récemment, Provost *et al.* ont démontré la faisabilité de la sommation cohérente des ondes divergentes en utilisant une matrice virtuelle parcimonieuse située derrière la sonde afin d'atteindre des cadences élevées pour l'imagerie cardiaque 3D [Provost *et al.* (2014)]. Ces approches utilisent des PW ou des DW pour insonifier l'ensemble du milieu à chaque émission. Les échos rétrodiffusés sont ensuite acquis et traités pour reconstruire simultanément toutes les lignes de l'image d'intérêt, soit dans le domaine de Fourier [Lu (1997), Cheng and Lu (2006), Garcia *et al.* (2013)] soit dans le domaine spatial [Montaldo *et al.* (2009), Hasegawa and Kanai (2011), Papadacci *et al.* (2014)]. Il a été montré dans [Garcia *et al.* (2013)] que la complexité de calcul du processus de reconstruction en PW dans le domaine spatial est plus élevée que dans le domaine de Fourier. En ce qui concerne l'imagerie cardiaque, toutes les méthodes ultrarapides existantes reposent sur une configuration sectorielle associée à des DW, en raison de l'accès anatomique limité du cœur. De plus, il est intéressant de noter que toutes les méthodes basées sur des DW qui ont été proposées [Hasegawa and Kanai (2011), Papadacci *et al.* (2014), Provost *et al.* (2014)] effectuent la reconstruction dans le domaine spatial, ce qui entraîne une complexité de calcul élevée. Afin de réduire la charge de calcul en échocardiographie ultrarapide, une approche intéressante serait donc de développer une méthode de reconstruction d'imagee opérant avec des DW dans le domaine de Fourier pour l'imagerie cardiaque en 2D et 3D.

1.2 Objectif

Dans le contexte décrit ci-dessus, l'objectif de ce travail est donc de développer une méthode permettant de réaliser une imagerie échocardiographique 3D ultrarapide, sur la base d'émissions en DW et d'une reconstruction réalisée dans le domaine de Fourier, ainsi que l'évaluation précise de cette approche. En partant du cas de l'imagerie 2D par onde plane, le présent travail se propose d'atteindre progressivement ce but en abordant successivement les aspects méthodologiques suivants:

- Une nouvelle méthode d'imagerie 2D par ondes planes, basée sur le théorème de la coupe centrale. Cet algorithme permet une reconstruction radiale du spectre de l'objet et fournit une alternative aux techniques d'imagerie basées sur des ondes planes et travaillant dans le domaine de Fourier.

- Une extension des méthodes d'imagerie 2D par ondes planes opérant dans le domaine de Fourier pour l'imagerie sectorielle par ondes divergentes. Nous proposons une transformation explicite en établissant un isomorphisme en termes de temps de parcours lorsque soit une onde divergente soit une onde plane est utilisée en transmission. Cette formulation permet la reconstruction d'images présentant un grand secteur angulaire dans le domaine de Fourier avec une complexité de calcul plus faible par rapport aux techniques actuelles.

- Une méthode d'imagerie 3D par ondes divergentes dans le domaine de Fourier. La formulation proposée en 2D est étendue en 3D. La méthode ainsi obtenue fournit des résultats compétitifs en termes de qualité d'image tout en conduisant à une complexité de calcul beaucoup plus faible relativement aux méthodes classiques de retard-sommation.

II. Contexte

Chapitre 2. Échocardiographie

2.1 Formation de l'image ultrasonore

L'échocardiographie est une modalité d'imagerie diagnostique qui permet de visualiser l'intérieur du cœur humain. Elle est basée sur la transmission dans le tissu d'impulsions ultrasonores focalisées à partir d'un transducteur, suivie du traitement des échos rétrodiffusés revenant de structures internes pour former une image du tissu.

Les images ultrasonores cardiaques sont généralement acquises en utilisant des sondes multiéléments, qui se composent d'un réseau d'éléments piézoélectriques 1D (ou d'une matrice 2D pour l'imagerie 3D) permettant de convertir l'énergie électrique en une pression acoustique et vice versa. La Figure VF.2 montre le principe de fonctionnement d'un élément de la sonde en transmission et réception de signaux. Lors de la transmission des impulsions, une tension de fréquence appropriée est appliquée aux éléments de la sonde, ce qui conduit les structures piézoélectriques à vibrer et à générer des ondes ultrasonores (Figure VF.2a). En réception, lorsque la partie réfléchie de l'impulsion ultrasonore atteint le transducteur, les vibrations acoustiques induisent un signal électrique, qui est appelé le signal d'écho.

(a)   (b)
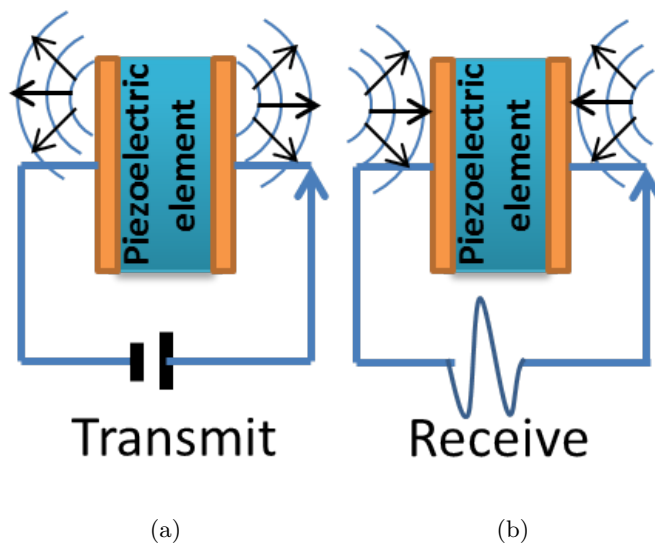
Figure VF.2: Principe de fonctionnement d'un élément de la sonde en transmission et réception. (a) En transmission, l'application d'une tension conduit l'élément piézoélectrique à vibrer et générer une onde ultrasonore. (b) En réception, l'application d'une vibration (une onde ultrasonore) conduit l'élément à produire une tension.

Classiquement, les images cardiaques 2D (ou images volumiques en 3D) sont construits en émettant successivement des faisceaux focalisés qui sont dirigés dans différentes directions pour couvrir le secteur désiré. Le procédé de pilotage et de focalisation des impulsions provenant de chaque élément de la sonde est appelé formation de voie. En échocardiographie, le formateur de voie le plus couramment utilisé est basé sur des retards et somme (DAS), ce qui est représenté schématiquement en Figure VF.3. L'idée du DAS est d'appliquer des retards différents à chaque élément piézo-électrique afin d'obtenir une focalisation en un point donné à la fois en transmission (Figure VF.3a) et en réception

(Figure VF.3b).

(a)

(b)
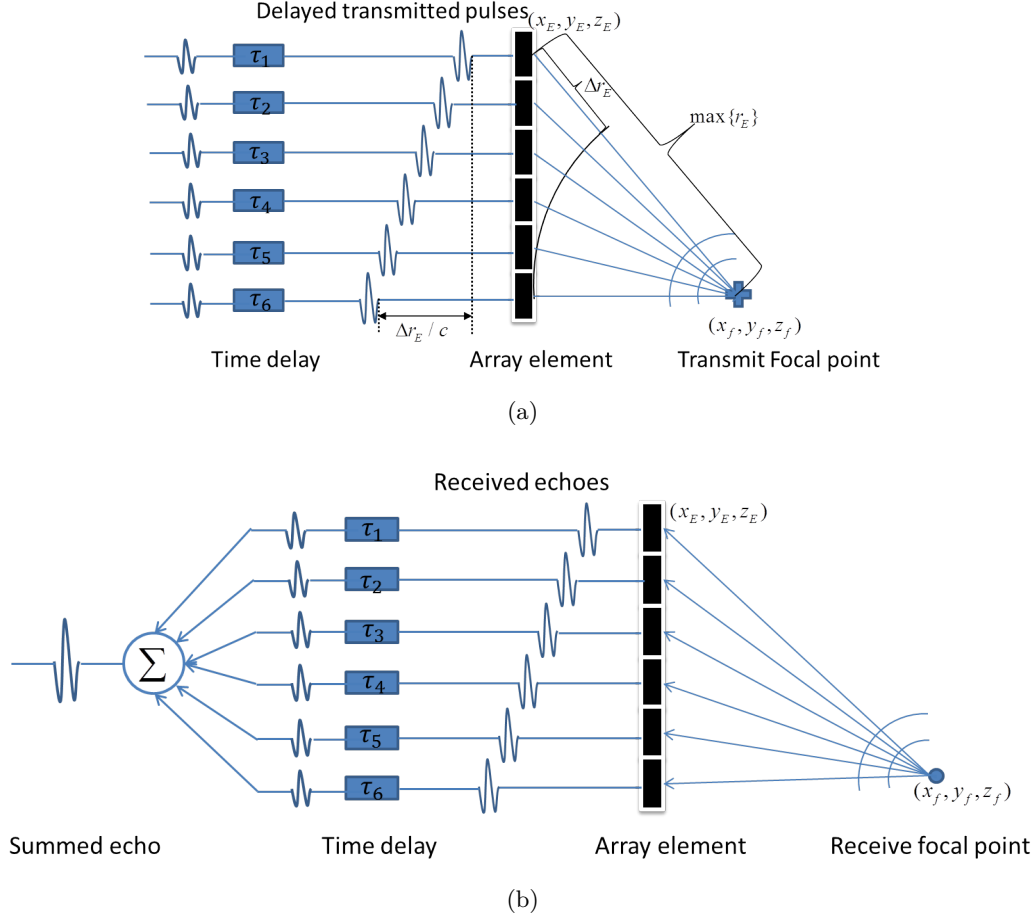
Figure VF.3: Ilustration du processus de formation de voie par retard et somme. (a) En émission, les impulsions provenant d'un ensemble d'éléments piézoélectriques sont retardés de manière appropriée (à savoir par application d'un τ_E différent à chaque élément) afin d'obtenir la direction et la focalisation en un point focal souhaité (x_f, y_f, z_f). (b) En réception, les échos reçus à partir d'un point (x_f, y_f, z_f) par chaque élément piézoélectrique sont également retardés, puis additionnés pour former le signal d'écho.

Lors de la transmission, tous les éléments piézo-électriques sont excités à des instants différents (*i.e.* application du retard τ_E dans la Figure VF.3a) ce qui permet aux ondes provenant de l'ensemble des éléments d'atteindre un point donné en même temps. La distance entre un élément (x_E, y_E, z_E) et le point focal (x_f, y_f, z_f) est:

$$r_E = \sqrt{(x_E - x_f)^2 + (y_E - y_f)^2 + (z_E - z_f)^2} \tag{VF.1}$$

Le retard τ_E qui est appliqué à chaque élément de la matrice peut alors facilement calculé par:

$$\tau_E = \frac{1}{c}\Delta\, r_E = \frac{1}{c}(\max\{r_E\} - r_E) \tag{VF.2}$$

où c est la vitesse du son. L'utilisation de ces retards sur les éléments permet de générer un faisceau et dirigé et concentré en un point quelconque du milieu imagé.

À la réception, les signaux reçus sur chaque élément sont décalés de la même manière

qu'en transmission (à savoir différents retards τ_E sont appliqués sur chaque élément pour compenser la différence des distances de propagation des ondes). Tous les signaux retardés sont ensuite additionnés afin d'obtenir le signal final qui contient toutes les contributions provenant du même diffuseur ponctuel dans le milieu.

La qualité d'une image ultrasonore dépend principalement de la résolution spatiale (*i.e.* la résolution axiale et latérale) et du contraste (par exemple, un rapport de contraste) du système d'acquisition.

2.2 Les modes d'imagerie

En application clinique de l'échocardiographie, trois modes d'imagerie sont employés: imagerie mode-M (ou mode mouvement), imagerie en deux dimensions (2D ou en mode B) et imagerie Doppler. La Figure VF.4 est un exemple d'intégration d'imageries 2D et mode M. Tout d'abord, une image 2D est acquise (image du haut de la Figure VF.4) et une ligne de balayage (ligne pointillée) est placée le long de la zone d'intérêt (ici la valve mitrale). Le Mode M montre alors les mouvements des tracts mitraux au fil du temps le long de l'axe de la ligne en pointillé (image en bas de la Figure VF.4). La Figure VF.5 donne un exemple d'imagerie Doppler couleur d'une régurgitation mitrale.
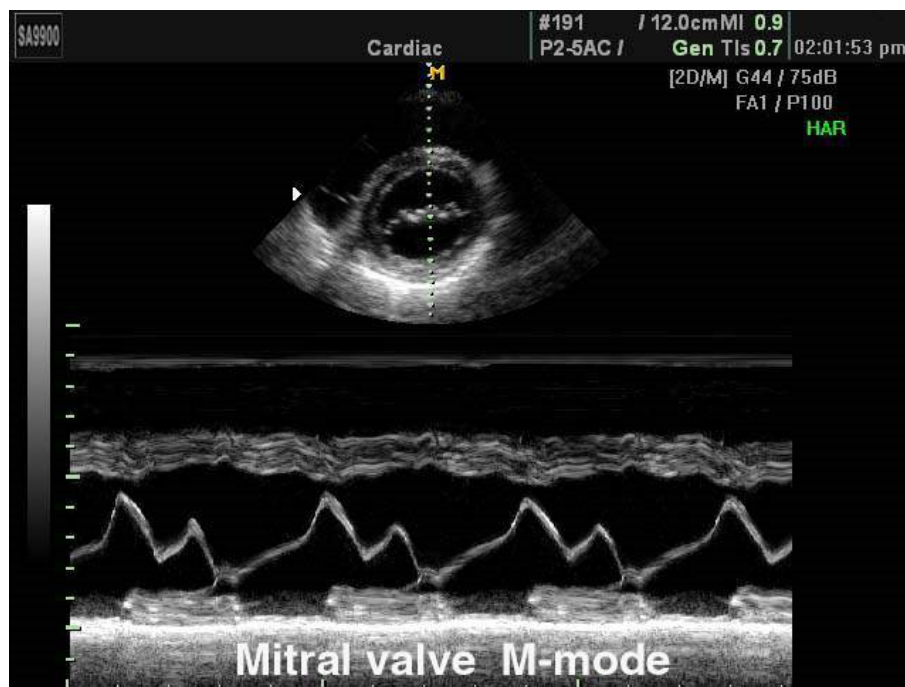
Figure VF.4: Images en M-mode M et B-mode. (En haut) Image en mode B représentant une section du cœur. (En bas) Représentation en mode M de la ligne pointillée. Image extraite de http://www.medison.ru/uzi/eho177.htm
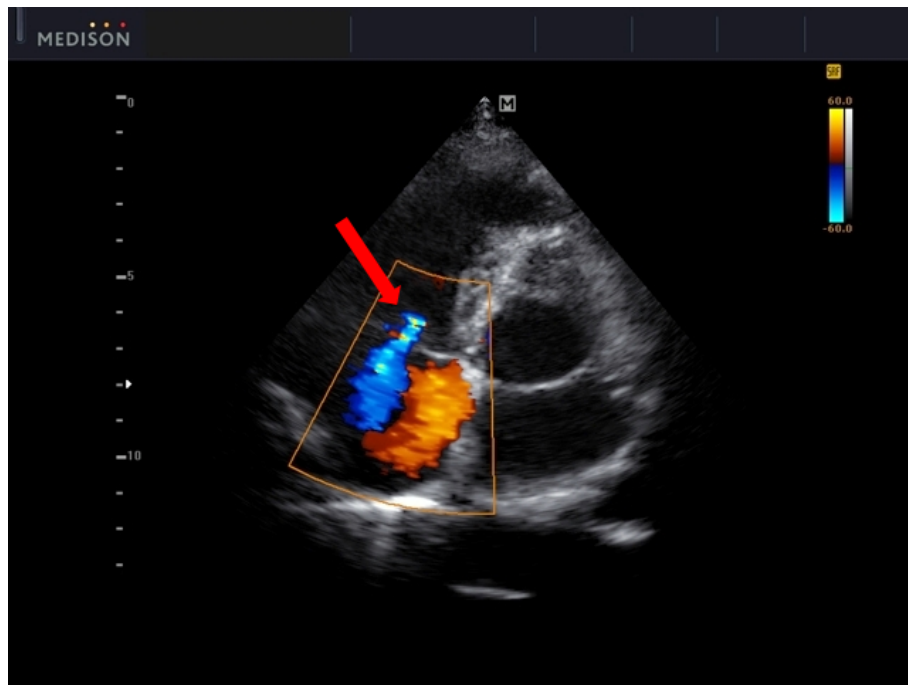
Figure VF.5: Un exemple d'imagerie Doppler couleur d'une régurgitation mitrale. Image extraite de http://www.medison.ru/uzi/eho562.htm

Chapitre 3. Etat de l'art: les méthodes ultra-rapides d'imagerie par ultrasons

3.1 Les méthodes ultra-rapides d'imagerie par ultrasons

Comme cela a été décrit en Section 1.1 et résumé dans [Cikes *et al.* (2014)], l'état de l'art des méthodes d'imagerie cardiaque ultra-rapides incluent la formation de voie parallèle en réception (également appelé acquisition multiligne (MLA) dans [Cikes *et al.* (2014)]), l'imagerie par émission multiligne, la synchronisation ECG et l'imagerie par ondes planes / divergentes. Avec les deux premières techniques, la cadence maximale d'imagerie atteinte est encore limitée (typiquement on peut obtenir une augmentation d'un facteur 2, 4, 8 de la cadence d'imagerie) en raison de la dégradation de la qualité de l'image (liée à une résolution inférieure, au couplage et aux artefacts de recouvrement). L'imagerie par ondes planes ou divergentes sont très prometteuses pour atteindre des cadences d'acquisition très élevées avec une qualité d'image contrôlée. Ces techniques utilisent des ondes planes (PW) ou des ondes divergentes (DW) pour insonifier l'ensemble du milieu avec une seule émission. Les échos rétrodiffusés sont ensuite acquis et traités pour reconstituer simultanément toutes les lignes de l'image d'intérêt. Un aperçu de ces méthodes est donné dans le tableau VF.1.

Table VF.1: Vue d'ensemble des méthodes d'imagerie ultrarapide par ondes planes ou divergentes existantes

Type d'onde	Premier auteur (Références)	Dimensions de exécution/domaine
Onde plane	Lu *et al.* [Lu (1997), Cheng and Lu (2006)]	2D et 3D/ Domaine de Fourier
	Montaldo *et al.* [Montaldo *et al.* (2009)]	2D/ Domaine spatial
	Garcia *et al.* [Garcia *et al.* (2013)]	2D/ Domaine de Fourier
	Provost *et al.* [Provost *et al.* (2014)]	3D/ Domaine spatial
Onde divergente	Hasegawa *et al.* [Hasegawa and Kanai (2011)]	2D/ Domaine spatial
	Papadacci *et al.* [Papadacci *et al.* (2014)]	2D/ Domaine spatial
	Provost *et al.* [Provost *et al.* (2014)]	3D/ Domaine spatial

3.2 Principe de la sommation cohérente

L'insonification avec une onde simple (PW ou DW) permet d'obtenir une cadence d'imagerie maximale, mais conduit à une qualité d'image (définie en termes de résolution et de contraste) intrinsèquement inférieure à celle obtenue avec la formation de voie multi-ligne focalisée classique. Afin de surmonter cette limitation, la technique de sommation cohérente spatiale a été utilisée dans toutes les études mentionnées ci-dessus pour améliorer la qualité de l'image. En utilisant plusieurs PW dépointées selon différents angles (ou DW provenant de différentes sources virtuelles), une focalisation synthétique est réalisée sur

toute l'image, comme cela se fait en imagerier synthétique d'ouverture (STA) [Jensen *et al.* (2006)b].

La Figure VF.6 montre le principe de la sommation cohérente pour des ondes planes. Les ondes planes directives sont transmises par le transducteur et insonifient l'ensemble de la région d'intérêt. Une image est reconstruite pour chacune des insonifications individuelles. L'image individuelle obtenue à partir de chaque onde plane est une image de mauvaise qualité. La sommation cohérente de ces images crée une focalisation synthétique sur l'ensemble de l'image et permet d'obtenir une image de haute qualité. Il a été montré dans [Montaldo *et al.* (2009)] que la focalisation synthétique obtenue par sommation cohérente est la même que celle obtenue par la méthode de focalisation classique si un nombre suffisant d'ondes planes est utilisé (à savoir 71 ondes planes en transmission, ce qui correspond à une cadence de 176 Hz dans [Montaldo *et al.* (2009)]), ce qui permet d'avoir la même qualité d'image dans les deux cas.

La Figure VF.7 (Figure 1 dans [Papadacci *et al.* (2014)]) montre le principe de la sommation cohérente pour des ondes divergentes en transmission. Chaque onde est transmise individuellement dans le milieu (Figure VF.7a). En appliquant des retards adéquats sur chaque onde, la sommation cohérente de ces ondes permet de focaliser à des profondeurs et des positions latérales différentes et ((b), (c), (d) en Figure VF.7).
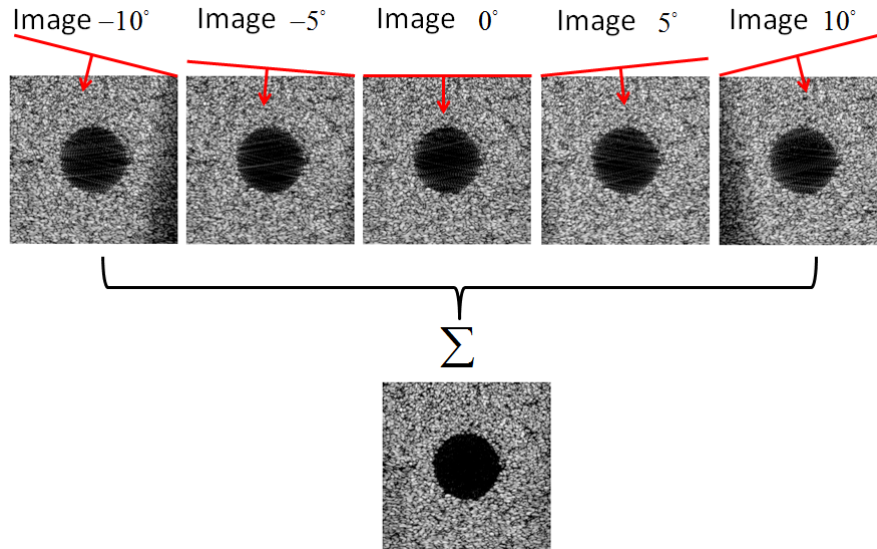
Figure VF.6: Principe de sommation cohérente d'ondes planes. Le milieu est insonifié avec des ondes planes dépointées, et les images sont reconstruites individuellement pour chaque onde plane. Les images individuelles obtenues à partir de chaque onde plane sont des images de faible qualité. La sommation cohérente de ces images crée une focalisation sur l'ensemble de l'image et permet d'obtenir une image de bonne qualité.

3.3 Méthodes de compensation de mouvement pour l'imagerie ultrarapide

Comme cela est décrit ci-dessus, l'image finale produite par des techniques d'imagerie ultra-rapide (sur la base d'insonifications par ondes planes ou divergentes) dépend de la sommation cohérente des images obtenues par plusieurs émissions, de façon à ce qu'une focalisation synthétique soit obtenue sur l'ensemble de l'image. Cependant, lorsque les diffuseurs se déplacent rapidement entre deux transmissions, un décalage temporel apparaît dans les deux signaux successifs reçus, ce qui entraîne une dégradation de la qualité de
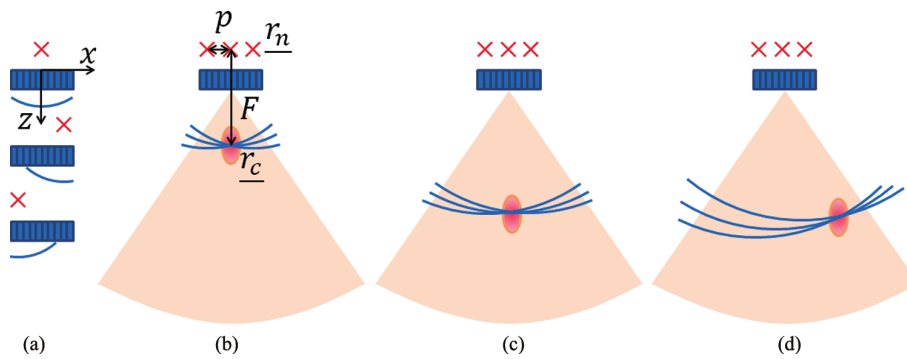
Figure VF.7: (Figure 1 dans [Papadacci *et al.* (2014)]) Principe de sommation cohérente avec des ondes divergentes. (a) Trois ondes divergentes définies par leur source virtuelle (les croix rouges en r_n) espacées d'un pas virtuel p, sont envoyés de façon indépendante avec une sonde multiéléments directement en contact avec la région d'intérêt. Chaque onde divergente est rétrodiffusée par les hétérogénéités et la sonde reçoit l'écho correspondant. La formation de voie est réalisée, par application de retards correspondant à une interférence constructive de ces ondes divergentes au point focal r_c. (b) En modifiant le retard appliqué à chacun des échos rétrodiffusés en (a), les ondes résultantes peuvent interférer et être focalisées à des profondeurs différentes, comme en (c) et à des positions latérales différentes, comme en (d).

l'image lors de la sommation cohérente [Wang and Lu (2007)]. Lorsque le mouvement est inférieur à $\lambda/4$ (λ représentant la longueur d'onde), ce décalage temporel peut être approximé par un décalage de phase dans les signaux de réception démodulé en quadrature (IQ) [Denarie *et al.* (2013)b]. Pour des tissus en mouvement, ce déphasage doit être pris en compte au cours du processus de sommation cohérente de façon à diminuer les artefacts dus au mouvement.

Plusieurs approches ont donc été proposées pour résoudre ce problème en imagerie par synthèse d'ouverture (STAI) [Trahey and Nock (1992), Kim *et al.* (2002), Oddershede and Jensen (2007), Yiu *et al.* (2008), Gammelmark and Jensen (2014)]. Très récemment, les méthodes de compensation de mouvement adaptées à la sommation cohérente en PW et DW ont été étudiées dans [Denarie *et al.* (2013)b] et [Poree *et al.* (2016)]. Dans ces deux méthodes, seul le mouvement radial (*i.e.* le mouvement perpendiculaire à la surface du transducteur) est considéré, puisque le déplacement latéral (à savoir un mouvement parallèle à la surface du transducteur) est supposé avoir une influence plus faible sur l'image [Wang and Lu (2007)].

III. Contribution

Chapitre 4. Influence du schéma de transmission en imagerie ultra-rapide par ondes planes

Dans ce chapitre, nous réalisons une étude détaillée de l'influence du schéma de transmission sur le système d'imagerie part ondes planes. Une étude analytique du problème nous permet de définir un schéma de transmission efficace dit dichotomique pour l'acquisition linéaire, ce qui permet d'améliorer la qualité des images reconstruites pour une cadence d'acquisition fixée. Le schéma de transmission dichotomique est décrit ci-dessous:

1. Nous fixons d'abord la profondeur maximale z_f que nous voulons imager.

2. L'équation (4.11) permet alors de calculer l'angle maximum optimal α_{max} qui est utilisé quel que soit le nombre de SPW impliqués dans la sommation cohérente.

3. Les valeurs des angles de la SPW utilisés en transmission sont alors répartis de manière uniforme sur l'intervalle $-\alpha_{max}$ to α_{max}.

L'efficacité du schéma de transmission dichotomique est évaluée au travers de son application aux techniques de reconstruction récentes utilisées en imagerie rapide. La qualité des images reconstruites est évaluée en termes de résolution et de contraste en simulations et sur des données acquises *in vitro*. La Figure VF.8 permet d'observer l'amélioration de la résolution latérale en fonction du nombre de SPW pour les différentes techniques de reconstruction et pour différentes profondeurs. En premier lieu, on peut constater que les trois méthodes produisent une qualité d'image similaire que ce soit pour une PW unique (Figure VF.8a) ou en utilisant 21 SPW avec sommation cohérente (Figure VF.8b). Ces observations sont confirmées par les deux graphes de la Figure VF.8c, qui présentent l'évolution des résolutions latérales mesurées à 20 et 40 mm en fonction du nombre de SPW. Ainsi, la résolution latérale correspondant à la transmission dichotomique s'améliore rapidement pour 3 SPW, puis tend à se stabiliser à la valeur optimale, quelle que soit la méthode de reconstruction, à savoir environ 0.9 mm à 20 mm de profondeur et entre 0.6 et 0.8 mm pour 40 mm de profondeur, ce qui est cohérent avec ce qui a été précédemment observé à partir de simulations. Le schéma dichotomique atteint la valeur optimale de résolution latérales avec la transmission de seulement 3 SPW (correspondant à une cadence d'acquisition de 5133 image/s), tandis que le schéma classique (lignes pointillées) atteint la même valeur après la transmission de 21-SPW (correspondant à une cadence d'acquisition de 733 image/s). La comparaison avec le schéma de transmission classique démontre donc le potentiel de l'approche dichotomique, puisqu'elle permet de diviser par un facteur quatre le nombre d'ondes planes utilisées, tout en conservant la même qualité d'image.
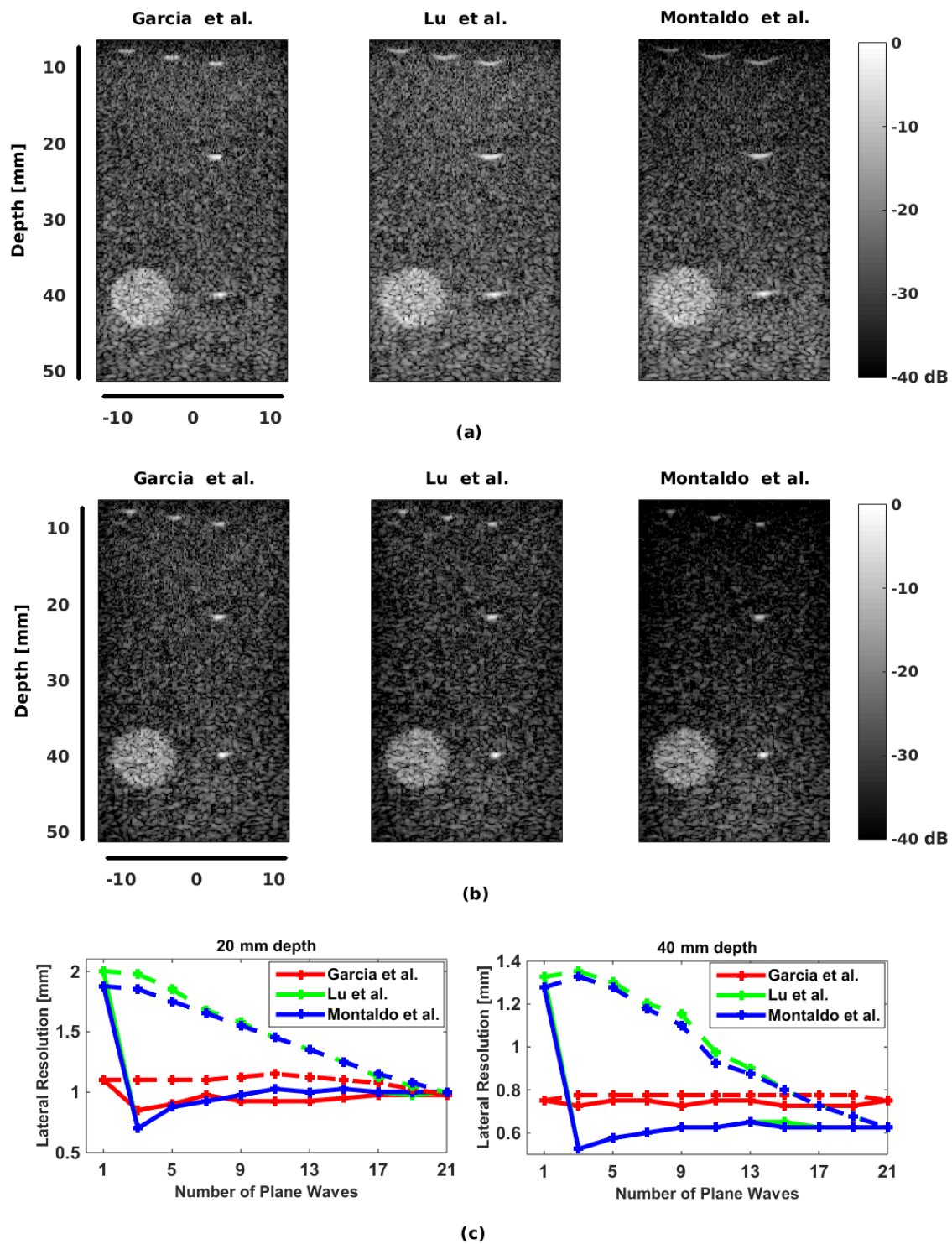
Figure VF.8: Images en mode B d'un fantôme CIRS (modèle: 054GS) obtenues à partir des trois méthodes de reconstruction avec (a) 1-PW et (b) la sommation cohérente de 21-SPW. (c) mesure de la résolution latérale en fonction du nombre de SPW. Les lignes pleines correspondent au schéma de transmission dichotomique proposé, tandis que les lignes en pointillés correspondent au schéma de transmission classique.

Chapitre 5. Ultrasound Fourier Slice Beamforming

Dans ce chapitre, une méthode alternative d'imagerie ultra-rapide alternative Fourier (UFSB) est proposée. L'aspect théorique de la méthode UFSB est basé sur l'exploitation du théorème de la coupe centrale pour la reconstruction de l'image échographique. La mise en œuvre générique de l'approche UFSB proposée (basée sur insonifications SPW) peut être résumée comme suit:

1. Transmission d'une onde plane avec un angle ϕ_j. L'angle de tir ϕ_j est obtenu en appliquant un retard au temps d'activation de chaque élément de la matrice. Le retard d est donné par $d(x_i) = x_i \sin(\phi_j)/c, x_i \in (-D/2, D/2)$, où x_i est la position de l'élément de la sonde, c est la vitesse du son, et D est la taille d'ouverture. Pour rendre le système causal, un retard supplémentaire constant $dt = \left| \frac{D \sin(\phi_j)}{2c} \right|$ est ajouté à la fonction de retard.

2. Réception simultanée des échos rétrodiffusés sur chaque élément du transducteur. Les données 2D $s(x_i, t)$ sont recueillies. Chaque colonne de $s(x_i, t)$ correspond aux données reçues par l'élément situé à la position x_i.

3. Transformation de Fourier 1D des données reçues $s(x_i, t)$ par rapport à t pour obtenir les échos dans le domaine fréquentiel $S(x_i, f)$.

4. Application des retards en réception pour obtenir une réception des SPW avec un angle ξ_i. Dans le domaine temporel, les retards appliqués sur les $s(x, t)$ sont donnés par $\tau(x_i) = x_i \sin(\xi_i)/c, x_i \in (-D/2, D/2)$ pour recevoir une SPW avec un angle ξ_i. Puisqu'un retard dt constant a été ajouté à transmission, celui-ci doit être compensé à la réception. Le retard appliqué à la réception est alors $\tau - dt$. En application de la propriété de décalage de la transformée de Fourier, une multiplication par une exponentielle complexe $\exp(-j2\pi f(\tau - dt))$ est appliquée à $S(x_i, f)$. Une ligne radiale du spectre de Fourier 2D de l'objet est obtenue en effectuant la sommation des signaux correspondants $S(x_i, f) \exp(-j2\pi f(\tau - dt))$ selon x_i.

5. Répétition de l'étape 4 avec un angle différent ξ_i afin d'échantillonner le spectre complet de l'objet, puis interpolation du spectre radial échantillonné sur une grille régulière.

6. Application de la transformée de Fourier inverse 2D pour reconstruire l'image RF correspondante.

7. Si des SPW successives sont utilisées dans le but de réaliser une sommation cohérente, répétition des étapes 3 à 6 pour chaque tirs et calcul de la moyenne de l'ensemble des d'images RF reconstruites qui fournit l'image finale.

Les performances de la méthode UFSB en termes d'imagerie sont évaluées à partir de données simulées et expérimentales. Les résultats obtenus ont montré que la technique UFSB produit des résultats très compétitifs en termes de qualité d'image relativement aux méthodes les plus récentes. Les Figures VF.9a et VF.9b montrent des images de carotide obtenues avec la méthode UFSB proposée ainsi que par trois méthodes imagerie récentes en utilisant soit 1 PW soit 21 SPW pour la transmission avec sommation cohérente. Ces résultats illustrent visuellement le fait que les images produites par les différentes méthodes sont très proches en termes de qualité d'image et de définition de speckle. Afin d'étudier l'influence des quatre méthodes de reconstruction, nous affichons en la Figure VF.9c les

différences absolues des images normalisées de la carotide de la Figure VF.9b. Sur cette figure, on constate que les différences entre UFSB et les trois autres méthodes sont assez faibles. En particulier, la différence entre UFSB et la méthode de Lu est presque nulle pour la région d'imagerie d'intérêt (*i.e.* de 5 mm à la profondeur de 40 mm), ce qui renforce les observations du fait que le rapport de contraste (CR) de ces deux méthodes présentent les valeurs les plus proches.
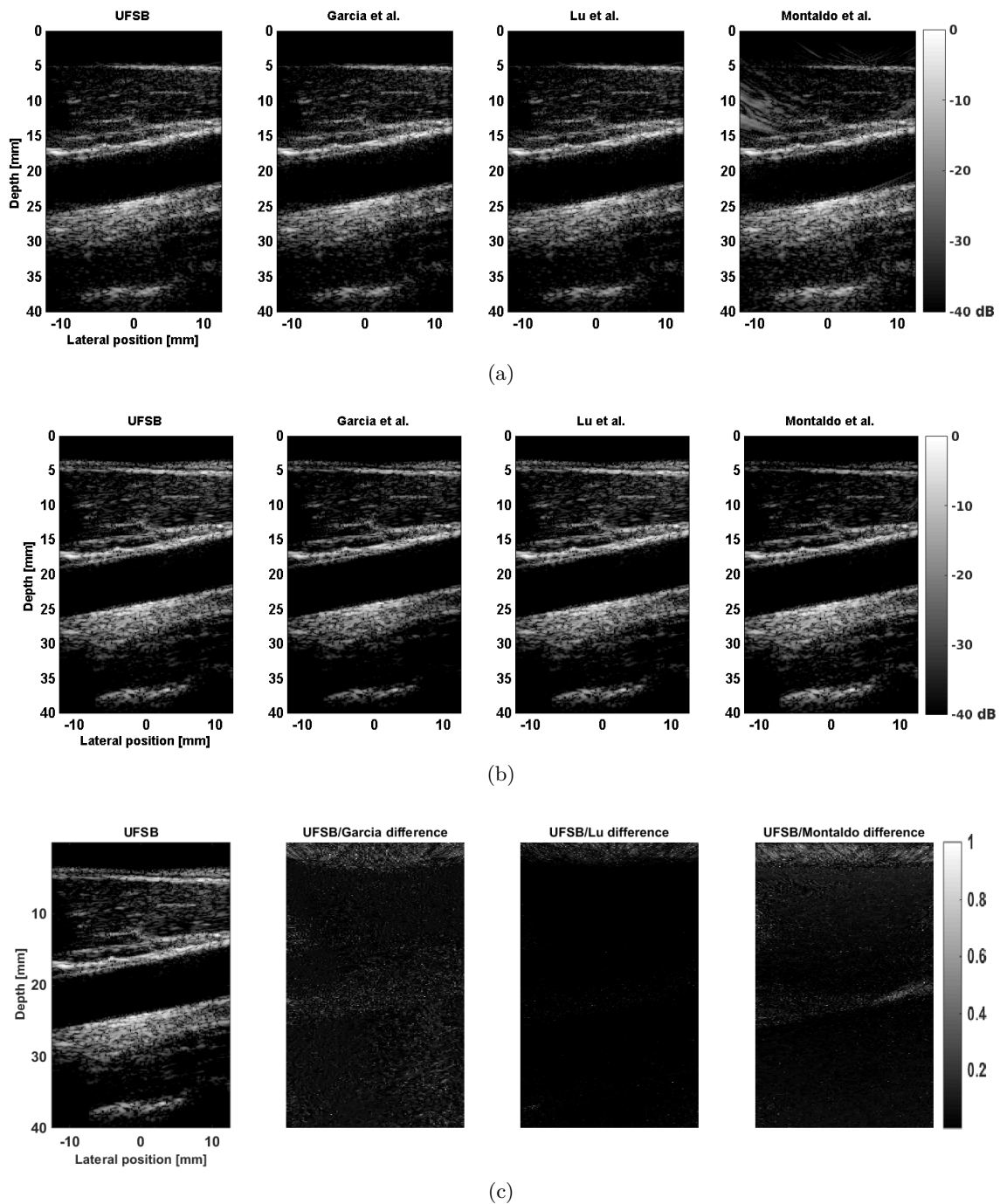
Figure VF.9: Données expérimentales acquises *in vivo* - Image de la carotide reconstruite selon quatre méthodes d'imagerie par ondes planes en utilisant (a) 1-PW et (b) 21-SPW avec sommation cohérente. (c) Différences absolues entre les images obtenues par UFSB et les 3 autres méthodes de reconstruction.

Chapitre 6. Extension des méthodes opérant dans le domaine Fourier à l'imagerie sectorielle 2D

Dans ce chapitre, nous présentons une transformation explicite permettant l'extension des techniques opérant dans le domaine de Fourier à la reconstruction des images sectorielles utilisant des ondes divergentes. L'idée principale est d'établir une équivalence en termes de temps de vol entre une transmission par DW ou par PW, comme cela est illustré en Figure VF.10. En effet, une telle relation permettrait la reconstruction d'une image sectorielle à partir d'une DW en utilisant le même formalisme que celui utilisé pour une acquisition linéaire en PW. Ce type d'isomorphisme entre temps de vol a déjà été utilisé par Garcia *et al.* pour adapter la technique de migration de Stolt issue du domaine de la sismique à l'imagerie ultrasonore en onde plane [Garcia *et al.* (2013)].
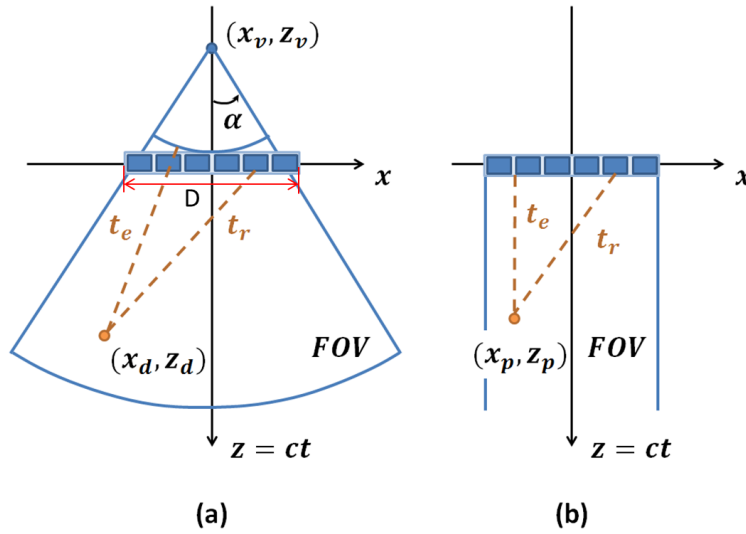
Figure VF.10: Illustration du temps de vol (noté t_e et t_r) obtenus lorsque soit (a) une onde divergente ou (b) une onde plane est utilisée en transmission. Dans les deux cas, $(t_e + t_r)$ correspond au temps nécessaire à l'onde d'insonification pour atteindre un diffuseur (point orange), puis revenir à un élément spécifique du transducteur.

Comme cela est représenté sur la Figure VF.10, un transducteur linéaire 1-D situé dans le plan z = 0, centré en x = 0 et où chaque élément de la sonde E est positionné à $(x_E, 0)$ est excité pour générer une DW (Figure VF.10a) ou une PW (Figure VF.10b) pour insonifier le milieu. Pour le moment, nous supposons pour la transmission PW que l'ouverture de la sonde est infinie. Une DW est obtenue par l'excitation d'une source virtuelle située en arrière de la sonde et située aux coordonnées (x_v, z_v), où $z_v \leq 0$ est déterminé par l'ouverture angulaire choisie α et la sous-ouverture de largeur D, comme cela est montré en Figure VF.10a:

$$z_v = -\frac{D/2}{\tan(\alpha)} \tag{VF.3}$$

Dans ce contexte, le temps nécessaire à une DW pour atteindre un diffuseur ponctuel positionné en (x_d, z_d) dans le milieu et de revenir à un élément du transducteur situé en $(x, 0)$ est donné par:

$$\tau_d(x_E) = \left(\sqrt{(x_d - x_v)^2 + (z_d - z_v)^2} + z_v + \sqrt{(x_d - x_E)^2 + z_d^2} \right) / c \qquad \text{(VF.4)}$$

Où $\sqrt{(x_d - x_v)^2 + (z_d - z_v)^2} + z_v$ correspond à la distance que parcourt l'onde pour atteindre le diffuseur, et $\sqrt{(x_d - x_E)^2 + z_d^2}$ correspond à la distance entre le diffuseur et l'élément du transducteur.

Dans le cas d'une PW avec une incidence normale, le temps vol nécessaire pour atteindre un diffuseur ponctuel en (x_p, z_p) et revenir au même élément $(x_E, 0)$ est donné par:

$$\tau_p(x_E) = (z_p + \sqrt{(x_p - x_E)^2 + z_p^2}) / c \qquad \text{(VF.5)}$$

En imposant l'égalité du développement de Taylor au premier ordre des termes (VF.4) et (VF.5) avec $x_E = x_v$, la relation suivante entre (x_d, z_d) et (x_p, z_p) peut être obtenue:

$$\begin{cases} x_p \approx \dfrac{(x_d - x_v)\left(\sqrt{(x_d-x_v)^2+(z_d-z_v)^2}+z_v+\sqrt{(x_d-x_v)^2+z_d^2}\right)}{z_d+\sqrt{(x_d-x_v)^2+z_d^2}} + x_v \\[4mm] z_p \approx \dfrac{z_d\left(\sqrt{(x_d-x_v)^2+(z_d-z_v)^2}+z_v+\sqrt{(x_d-x_v)^2+z_d^2}\right)}{z_d+\sqrt{(x_d-x_v)^2+z_d^2}} \end{cases} \qquad \text{(VF.6)}$$

et

$$\begin{cases} x_d \approx \dfrac{1}{2}\dfrac{(x_p-x_v)\left(z_v^2-\left(z_p+\sqrt{(x_p-x_v)^2+z_p^2}-z_v\right)^2\right)}{z_v\,z_p-\left(z_p+\sqrt{(x_p-x_v)^2+z_p^2}-z_v\right)\sqrt{(x_p-x_v)^2+z_p^2}} + x_v \\[4mm] z_d \approx \dfrac{1}{2}\dfrac{z_p\left(z_v^2-\left(z_p+\sqrt{(x_p-x_v)^2+z_p^2}-z_v\right)^2\right)}{z_v\,z_p-\left(z_p+\sqrt{(x_p-x_v)^2+z_p^2}-z_v\right)\sqrt{(x_p-x_v)^2+z_p^2}} \end{cases} \qquad \text{(VF.7)}$$

Les équations (VF.6) et Eq. (VF.7) fournissent une équivalence explicite entre le diffuseur positionné en (x_d, z_d) et (x_p, z_p) insonifié par une DW avec une source virtuelle (x_v, z_v) et une PW avec une incidence normale. Par conséquent, la procédure suivante est proposée pour reconstruire une image sectorielle: i) une DW associée à la source virtuelle positionnée en (x_v, z_v) est transmise en utilisant une sonde cardiaque multiéléments conventionnelle de type phase array; ii) une technique de reconstruction pour PW et opérant dans le domaine de Fourier (par exemple la méthode de Lu ou UFSB) est appliquée aux échos reçus. L'équation (VF.6) montre que cette étape permet de reconstruire l'image ultrasonore souhaitée, mais exprimée dans le repère (x_p, z_p); iii) la transformation spatiale donnée par l'équation (VF.7) est appliquée, ce qui permet d'exprimer l'image reconstruite dans le repère cartésien classique.

Nous avons ensuite étudié au moyen de simulations numériques la validité du cadre proposé pour la reconstruction d'images sectorielles par des techniques travaillant dans le domaine de Fourier. Dans ce but, nous avons utilisé un fantôme synthétique simple, composé d'un ensemble discret de diffuseurs ponctuels. Tout d'abord, nous utilisons 1 DW en transmission pour valider la transformation spatiale que nous avons obtenue ci-dessus. La Figure VF.11 montre les images correspondantes dans l'espace modifié, *i.e.*

dans le repère (x_p, z_p) (Figure VF.11a) et les images finales obtenues dans l'espace cartésien par les méthodes UFSB (Figure VF.11b) et de Lu (Figure VF.11c). Les cercles rouges correspondent à la position réelle des diffuseurs. La Figure VF.11a montre que l'application de la méthode UFSB aux données collectées à partir d'une transmission en DW se traduit par une dilatation des positions des diffuseurs. La transformation spatiale (Eq. (VF.6) et Eq. (VF.7)) permet ensuitede reconstruire tous les diffuseurs avec des positions correctes dans l'espace cartésien (Figure VF.11b). La Figure VF.11c est l'image reconstruite à partir de la méthode de Lu. Visuellement, les deux images (reconstruites par UFSB et la méthode de Lu) sont assez semblables.

Nous avons également étudié les performances des méthodes ultra-rapides opérant dans le domaine de Fourier pour l'imagerie du cœur humain *in vivo*. Tout d'abord, nous reconstruisons l'image cardiaque en utilisant soit l'extension de méthodes opérant dans le domaine de Fourier décrite précédemment, soit la méthode spatiale de Papadacci sans aucune compensation de mouvement, comme le montre la Figure VF.12. Comme dans les simulations, ces résultats illustrent visuellement le fait que des images produites par ces différentes méthodes sont proches en termes de qualité d'image et de définition de speckle. Cependant, des artéfacts de mouvement peuvent être observés dans l'image, comme cela a été montré dans [Poree *et al.* (2016)]. Ceci est dû au fait que les vitesses du myocard peuvent atteindre des valeurs d'environ 20 cm/s au cours de la systole, ce qui entraîne un mouvement non négligeable des tissus entre la transmission de deux ondes consécutives.

Afin de minimiser l'influence du mouvement sur la qualité de l'image, Poree *et al.* ont proposé dans [Poree *et al.* (2016)] d'intégrer une compensation de mouvement basée sur le Doppler (MoCo, décrit en la Section 3.3.2) dans le processus de sommation cohérente de la méthode DAS (à savoir la méthode spatiale de Papadacci). Nous avons étudié ainsi la possibilité d'intégrer la compensation de mouvement proposée par Poree *et al.* dans l'approche de type Fourier que nous proposons. La Figure VF.13 montre une image extraite de la séquence complète que nous avons reconstruite en utilisant l'extension sectorielle de la méthode de Lu avec et sans compensation de mouvement. On peut voir que la qualité d'image est améliorée avec MoCo. En particulier, le septum peut être aisément distingué et présente un bon contraste, comme cela est montré en Figure VF.13b. Ce résultat démontre donc également la possibilité d'appliquer la méthode proposée pour des acquisitions *in vivo*, ainsi que sa flexibilité, puisque nous avons pu facilement intégrer la méthode de compensation de mouvement proposée par Poree *et al.* [Poree *et al.* (2016)].

Les résultats obtenus à partir des simulations et des données expérimentales ont révélé que l'extension de la méthode de Lu proposée produit des résultats compétitifs avec une complexité de calcul plus faible par rapport à la technique de retard et somme (DAS) conventionnelle. Ces résultats ont également montré la généralité de la transformation spatiale, et ce indépendamment de la position de la source.
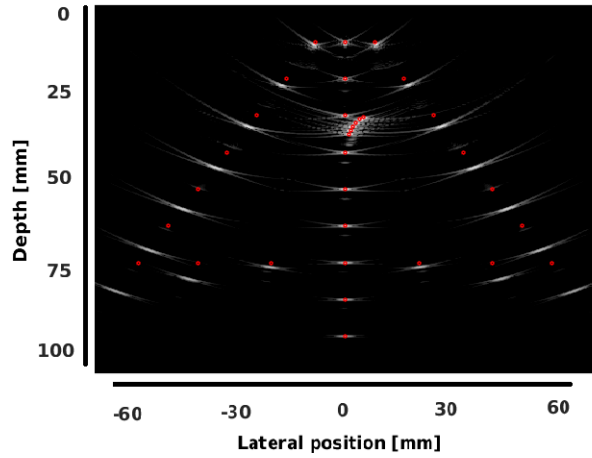
(a)
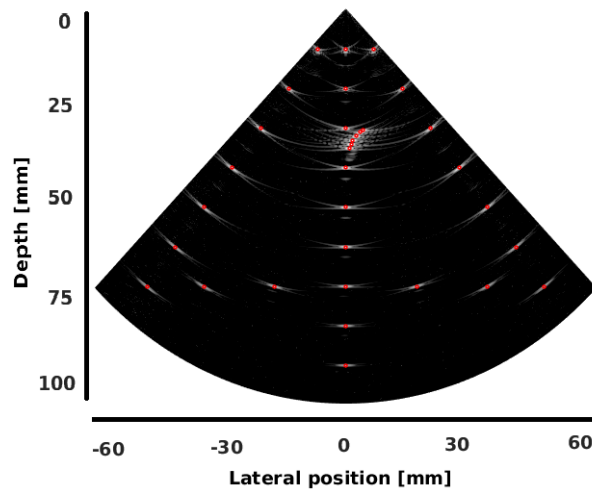
(b)
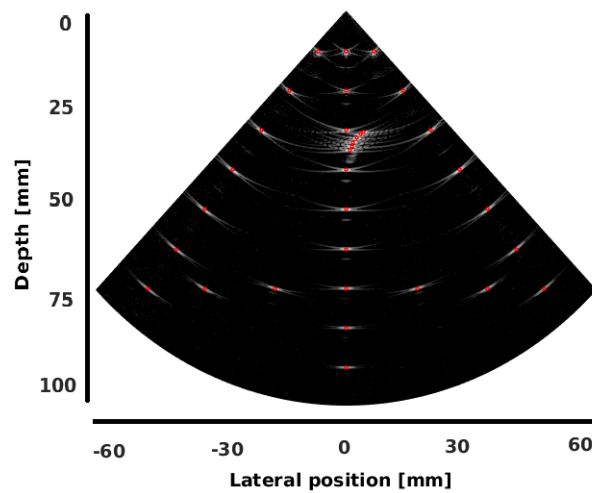
(c)

Figure VF.11: Reconstruction de l'image d'un fantôme synthétique (a) dans le repère direct avec la méthode UFSB et (b) dans le repère cartésien avec une reconstruction par (b) UFSB et (c) la méthode de Lu. Les images ont été obtenues en utilisant 1 onde divergente en transmission. Les cercles rouges correspondent à la position réelle des diffuseurs.
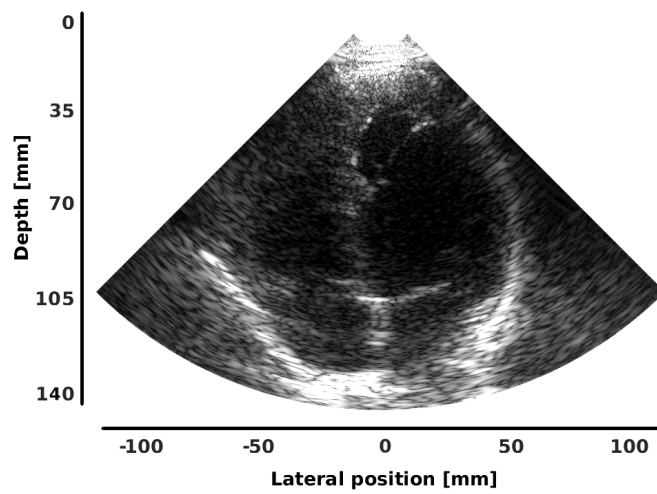
(a) Sectorial extension of UFSB method
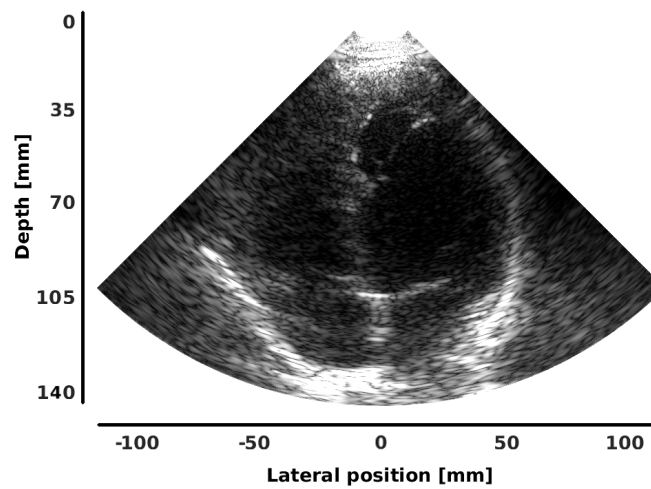
(b) Sectorial extension of Lu's method
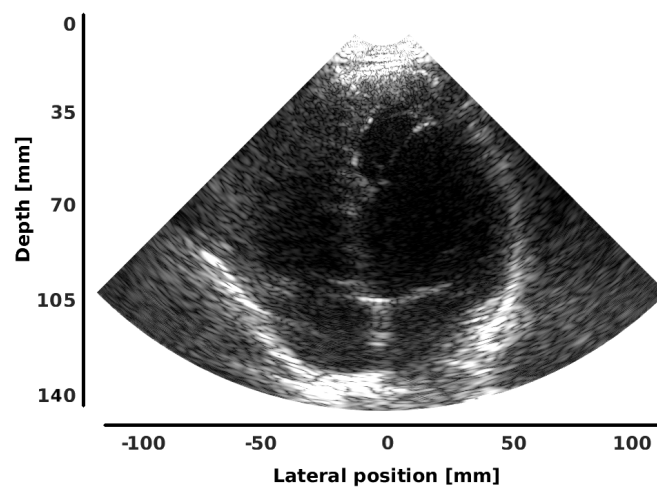
(c) Papadacci's method

Figure VF.12: Acquisitions *In vivo* - Image reconstruite à partir de (a) l'extension de la méthode UFSB, (b) l'extension de la méthode de Lu et (c) la méthode spatiale de Papadacci. Les reconstructions utilisent 32 ondes divergentes avec sommation cohérente et aucune compensation de mouvement.
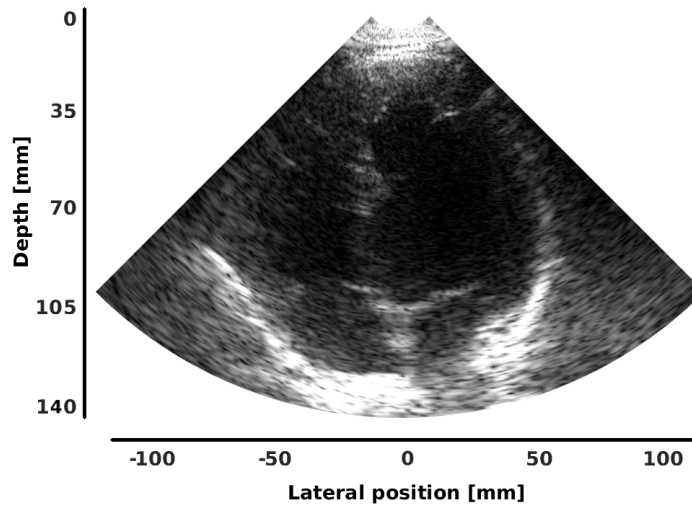
(a)
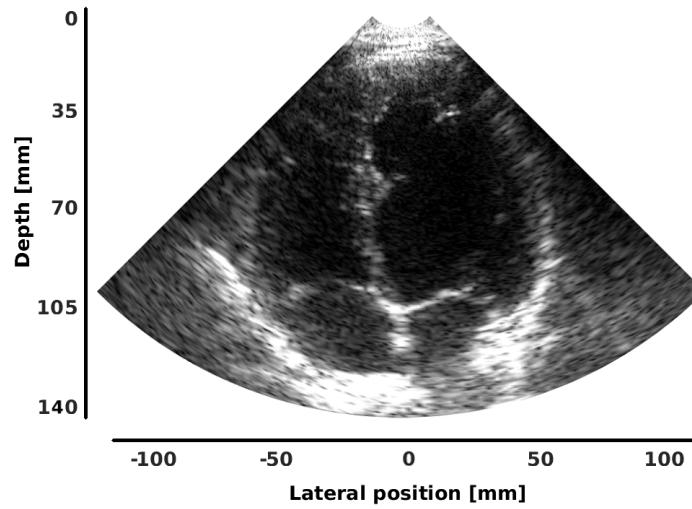
(b)

Figure VF.13: Acquisition *in vivo* - Compensation de mouvement (MoCo) appliquée en échocardiographie ultrarapide du ventricule gauche, en utilisant l'extension sectorielle de la méthode de Lu (a) sans et (b) avec MoCo.

Chapitre 7. Imagerie cardiaque ultra-rapide 3D

Dans ce chapitre, la formulation proposée dans le chapitre 6 est étendue en 3D en prenant en compte la coordonnée y dans l'équation du temps de vol lorsqu'une DW 3D ou une PW 3D est utilisée en transmission. La transformation spatiale 3D peut être alors obtenue et s'exprime comme suit:

$$
\begin{cases}
x_p \approx \dfrac{(x_d - x_v)\left(\sqrt{(x_d-x_v)^2+(y_d-y_v)^2+(z_d-z_v)^2}+z_v+\sqrt{(x_d-x_v)^2+(y_d-y_v)^2+z_d^2}\right)}{z_d+\sqrt{(x_d-x_v)^2+(y_d-y_v)^2+z_d^2}} + x_v \\[3ex]
y_p \approx \dfrac{(y_d - y_v)\left(\sqrt{(x_d-x_v)^2+(y_d-y_v)^2+(z_d-z_v)^2}+z_v+\sqrt{(x_d-x_v)^2+(y_d-y_v)^2+z_d^2}\right)}{z_d+\sqrt{(x_d-x_v)^2+(y_d-y_v)^2+z_d^2}} + y_v \\[3ex]
z_p \approx \dfrac{z_d\left(\sqrt{(x_d-x_v)^2+(y_d-y_v)^2+(z_d-z_v)^2}+z_v+\sqrt{(x_d-x_v)^2+(y_d-y_v)^2+z_d^2}\right)}{z_d+\sqrt{(x_d-x_v)^2+(y_d-y_v)^2+z_d^2}}
\end{cases}
\quad \text{(VF.8)}
$$

et

$$
\begin{cases}
x_d \approx \dfrac{1}{2}\dfrac{(x_p-x_v)\left(z_v^2-\left(z_p+\sqrt{(x_p-x_v)^2+(y_p-y_v)^2+z_p^2}-z_v\right)^2\right)}{z_v\,z_p-\left(z_p+\sqrt{(x_p-x_v)^2+(y_p-y_v)^2+z_p^2}-z_v\right)\left(\sqrt{(x_p-x_v)^2+(y_p-y_v)^2+z_p^2}\right)} + x_v \\[3ex]
y_d \approx \dfrac{1}{2}\dfrac{(y_p-y_v)\left(z_v^2-\left(z_p+\sqrt{(x_p-x_v)^2+(y_p-y_v)^2+z_p^2}-z_v\right)^2\right)}{z_v\,z_p-\left(z_p+\sqrt{(x_p-x_v)^2+(y_p-y_v)^2+z_p^2}-z_v\right)\left(\sqrt{(x_p-x_v)^2+(y_p-y_v)^2+z_p^2}\right)} + y_v \\[3ex]
z_d \approx \dfrac{1}{2}\dfrac{z_p\left(z_v^2-\left(z_p+\sqrt{(x_p-x_v)^2+(y_p-y_v)^2+z_p^2}-z_v\right)^2\right)}{z_v\,z_p-\left(z_p+\sqrt{(x_p-x_v)^2+(y_p-y_v)^2+z_p^2}-z_v\right)\left(\sqrt{(x_p-x_v)^2+(y_p-y_v)^2+z_p^2}\right)}
\end{cases}
\quad \text{(VF.9)}
$$

Où (x_v, y_v, z_v) est la position de la source virtuelle, (x_d, y_d, z_d) et (x_p, y_p, z_p) sont la position du diffuseur ponctuel qui est insonifié soit par une DW 3D ou une PW 3D avec une incidence normale.

A partir des équations (VF.8) et (VF.9), l'algorithme générique suivant est donc proposé pour reconstruire une image sectorielle en 3D: i) transmission d'une onde divergente utilisant une sonde matricielle 2D; ii) application aux signaux de réception d'une méthode de reconstruction pour onde plane 3D opérant dans le domaine de Fourier (*i.e.* la méthode de Lu). A partir de l'équation (VF.8), on peut constater que le résultat de cette étape permet de reconstruire l'image ultrasonore souhaitée, mais exprimée dans le système de coordonnées (x_p, y_p, z_p). iii) application de la transformation spatiale donnée par l'équation (VF.9), qui permet la reconstruction de l'image dans le repère cartésien classique.

La capacité de cette approche à reconstruire des images sans distorsion géométrique a été évaluée au travers de simulations numériques. La Figure VF.14 permet d'observer les coupes orthogonales parallèles au plan $x - z$ des images volumétriques reconstruites. Celles-ci ont été obtenues soit à partir de l'extension de la méthode (Figure VF.14a) de Lu proposée, soit à partir de la méthode spatiale DAS de Provost *et al.* (Figure VF.14b) en utilisant 81 ondes divergentes. Les cercles rouges correspondent à la position réelle des diffuseurs. Ces figures permettent de constater que l'extension de la méthode (Figure VF.14a) de Lu en 3D reconstruit les PSF à la bonne position. La transformation spatiale 3D n'introduit donc pas de distorsion géométrique. Enfin, on peut observer que les deux méthodes conduisent à une qualité d'image très similaire.

(a) Extension method of Lu in 3D   (b) Provost's method
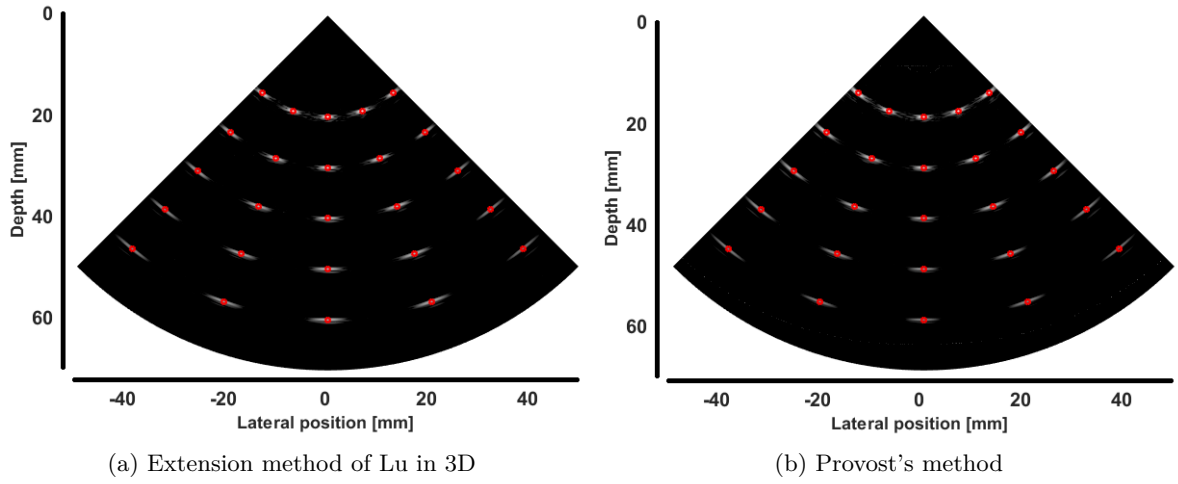
Figure VF.14: Orthogonal slices along $x - z$ direction of the reconstructed point scatterers phantom from (a) the proposed extension of Lu's method and (b) the method of Provost *et al.* using 81 diverging waves. The red circles correspond to the real positions of the point scatterers involved in the simulation.

IV. Conclusions et perspectives

Chapitre 8. Conclusions et perspectives

8.1 Conclusions

L'objectif de ce travail consistait à développer un procédé d'imagerie par ultrasons ultra-rapide en échocardiographie basé sur une insonification par onde divergentes et réalisant une reconstruction dans le domaine de Fourier. Le point de départ était une méthode classique d'imagerie 2D en ondes planes.

Nous avons en premier lieu étudié l'influence du régime de transmission sur la qualité d'image avec des ondes planes en transmission. Nous avons présenté un schéma de transmission dichotomique pour l'acquisition linéaire en analysant mathématiquement la pression générée. Nous avons ensuite montré que ce système de transmission peut améliorer la qualité des images reconstruites pour une cadence constante en utilisant les algorithmes de reconstruction conventionnels. La qualité des images reconstruites a été évaluée en termes de résolution et de contraste au moyen de simulations et acquisitions expérimentales réalisées sur des fantômes.

Nous avons ensuite proposé une nouvelle méthode d'imagerie 2D en ondes plane opérant dans le domaine de Fourier et basée sur le théorème de la coupe centrale. Cet algorithme permet de reconstruire le spectre de l'objet à imager radialement dans le domaine de Fourier. La méthode proposée a été évaluée et comparée avec les méthodes pour ondes planes existantes au moyen des simulations, d'acquisitions expérimentales réalisées sur des fantômes et *in vivo*. Les résultats que nous avons obtenus montrent que l'approche proposée fournit des résultats très proches de ceux fournit par les méthodes classiques en termes de résolution latérale et contraste de l'image.

Nous avons ensuite développé une transformation spatiale explicite permettant d'étendre les méthodes 2D opérant dans le domaine de Fourier d'une acquisition en géométrie linéaire avec des ondes planes à la géométrie sectorielle avec des ondes divergente en transmission. Cette transformation a été obtenue en établissant un isomorphisme en termes de temps de vol lorsque soit une onde divergente soit une onde plane est utilisée en transmission. Les résultats que nous avons obtenus à partir de simulations et d'acquisitions expérimentales *in vivo* montrent que l'application de cette extension à la méthode de Lu permet d'obtenir la même qualité d'image que la méthode spatiale de Papadacci basée sur des ondes divergentes, mais avec une complexité de calcul plus faible.

Finalement, la formulation proposée en 2D pour les méthodes ultra-rapides opérant dans le domaine de Fourier ont été étendues en 3D. Cela a été réalisé en tenant compte de la coordonnée y dans l'équation du temps vol de l'onde plane et de l'onde divergente. En étudiant la pression obtenue lors de la sommation cohérente des ondes divergentes 3D, un schéma de transmission dichotomique a été proposé dans le but d'améliorer la qualité d'image, et ce d'une manière suffisamment rapide pour être peu influencée par l'augmentation du nombre d'ondes divergentes. L'approche proposée donne des résultats compétitifs associés à une complexité de calcul beaucoup plus faible par rapport à la technique de retard et somme (DAS) conventionnelle.

8.2 Perspectives

Dans cette thèse, nous avons développé un formalisme dans le domaine de Fourier pour l'imagerie ultrasonore ultra-rapide utilisant des ondes divergentes en transmission. Le principal avantage de la méthode proposée est sa complexité de calcul plus faible. Celle-

ci pourrait encore être réduite en utilisant une sonde matricielle parcimonieuse au lieu de la l'ensemble des élément de la sonde afin de réduire le volume de données en réception [Roux *et al.* (2015)a, Roux *et al.* (2015)b]. D'autre part, cette méthode pourrait être encore améliorée en utilisant la transformée de Fourier rapide non uniforme (NUFFT) au lieu d'une simple interpolation lors de l'étape de remplissage spectral en 2D [Kruizinga *et al.* (2012)]. Étant donné que les signaux RF sont très peu dense dans le domaine de Fourier, il serait également intéressant d'appliquer une méthode de régularisation parcimonieuses pour l'imagerie 3D par onde plane afin d'améliorer la qualité des images [Carrillo *et al.* (2015)].

Puisque l'énergie transmise par onde divergente 3D diminue avec le cube de la profondeur, le rapport signal sur bruit de l'image diminue de manière significative pour les grandes profondeurs. Ainsi, l'émission d'ondes divergentes multiples comme cela a été proposé en [Tiran *et al.* (2015)] pourrait être exploitée pour améliorer le rapport signal à bruit sans compromettre la fréquence d'imagerie.

La méthode 3D proposée dans ce manuscrit, a été évaluée au moyen de simulations numériques. Des acquisition expérimentales réalisées sur les fantômes et *in vivo* doivent être effectuées pour évaluer les performances de cette méthode. Cependant, lors d'acquisitions réalisées *in vivo*, le mouvement du cœur est susceptible d'entraîner des artefacts de mouvement dans l'étape de sommation cohérente. Des recherches supplémentaires sur l'estimation du mouvement 3D des tissus devraient être réalisées pour compenser le mouvement du cœur avant l'étape de sommation.

Du fait que le schéma de transmission utilisé en vue de la sommation cohérente a également une influence sur l'estimation du mouvement [Denarie *et al.* (2013)b, Poree *et al.* (2016)], il est également important de développer un schéma de transmission 3D efficace. Si des volumes cardiaques 3D de haute qualité peuvent être acquis avec une implémentation matérielle raisonnable, il sera intéressant de mettre en œuvre la méthode sur un scanner ultrasonore commercial en vue d'applications cliniques diagnostiques.

Il serait très intéressant d'estimer les propriétés mécaniques du myocarde à partir des volumes cardiaques obtenus en utilisant la technique proposée, et ainsi d'avoir accès au mouvement et contraintes cardiaques au flux sanguin, etc. D'autres études devront être menées pour évaluer l'impact de notre technique sur l'évaluation de ces paramètres.

Appendix

Appendix 1

A.1   Investigation of defocusing effect

In addition to Figure 6.2 in Chapter 6, we set the following experiment in order to further investigate the potential defocusing effect induced by the proposed spatial transformation.

For a point (x_d, z_d) in the medium, we transmitted a diverging wave from a virtual source positioned at $(0, z_v)$ and received the corresponding backscattered echoes. To compute the beamformed image at location (x_d, z_d) using the conventional delay and sum technique (DAS), one has to compute a set of delays $\{\tau_d(i)\}_{i \in [1,N]}$ using the travel time equation derived for diverging wave (Eq.(6.3)). These delays are then used to select the set of intensities extracted from the received rawdata that will be summed to get the final value. The region corresponding to the selected intensities is displayed in blue in Figure A.1. Using the spatial transform proposed in Chapter 6 (Eq.(6.5)), we then derived the corresponding (x_p, z_p) point from which we computed the set of delays $\{\tau_p(i)\}_{i \in [1,N]}$ using the travel time equation derived for plane wave (Eq.(6.4)). These delays are used to select the set of intensities extracted from the received rawdata that will be summed to get the final value in the case of plane wave imaging. The corresponding region is displayed in red in Figure A.1. In the case of an effective equivalence between the DW and PW imaging techniques thanks to the introduced spatial transformation, the curves in red and blue should perfectly fit. The potential difference between the two curves thus allows a direct investigation of the defocusing effect. From the error map given in Figure 6.2, we can see that the maximum error occurs at the border of the image for a virtual source positioned at $(0, z_v)$. We thus propose in the figure below to investigate the defocusing effect from a set of point scatterers placed at the border of the image (azimuth angle of 40°) and for different depths (from 10 mm to 90 mm each 10 mm). For each experiment, only one point scatterer was used and we displayed the corresponding received rawdata as well as the red and blue curves computed from the protocol described above. The measured difference between the two curves was expressed in terms of wavelength. It is of importance to note that Figure 6.2 corresponds to the maximum of the error between the two curves computed

for each point of the image (*i.e.* the maximum value of the green curves given in the right part of Figure A.1). From these results, it can be seen that the maximum error appears for the points located in the near field (*i.e.* whose depth is lower or equal to 10 mm). For points located around 20 mm, the maximum error is close to $\lambda/8$. Finally, for points whose location is deeper than 20 mm, the maximum error goes below $\lambda/8$. These observations are coherent with the Taylor approximation we made for the delay calculation. Indeed, when the ration x/z is small, *i.e.* at far field, the assumption that $x = x_v$ is valid nearly everywhere in the field of view, making the two imaging systems equivalent. Moreover, since the maximum error related to our model hypothesis is lower than $\lambda/8$ for almost full scan region, it explains the negligible effect of defocusing artifact on the final reconstructed images.
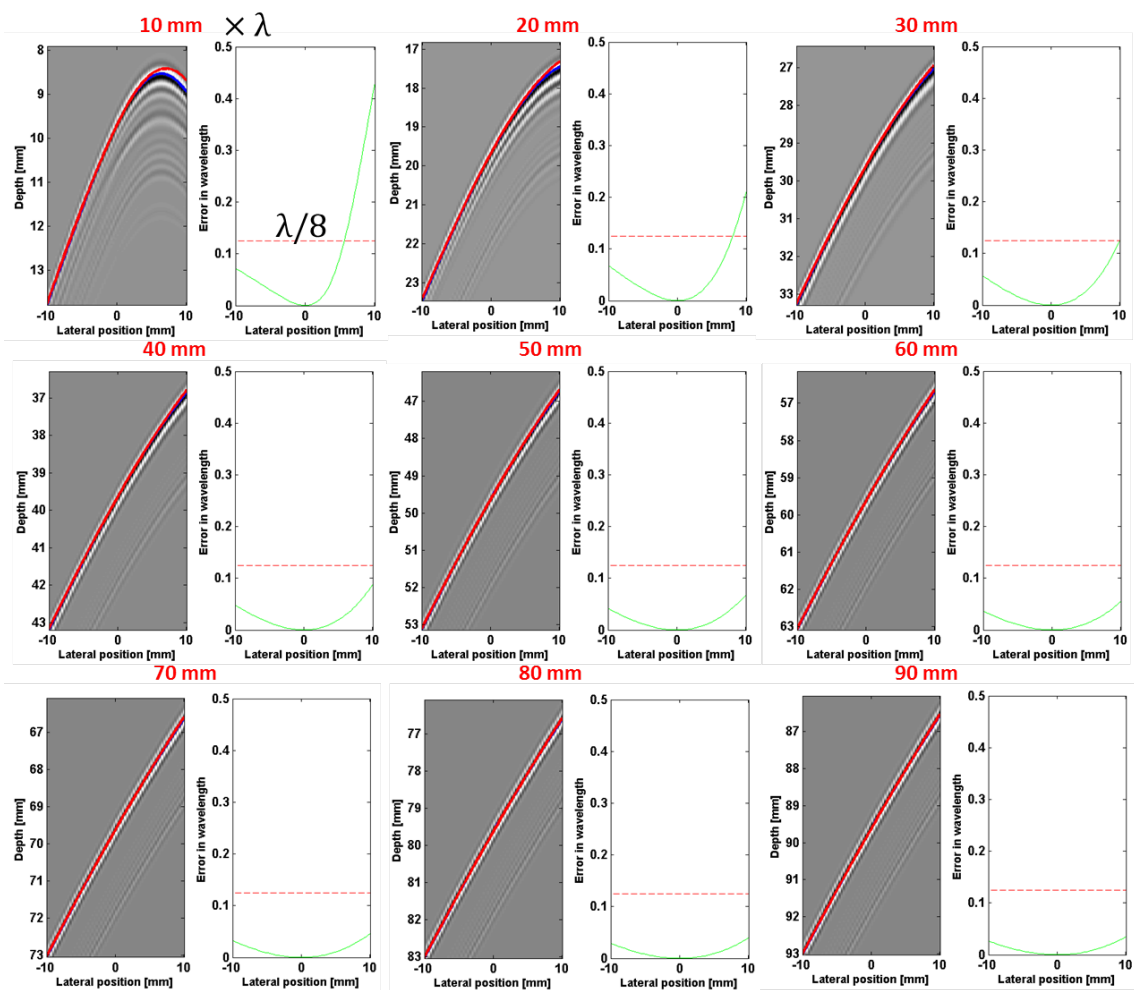
Figure A.1: Error derived in the beamforming process between DW and the equivalent PW imaging for a specific point with azimuth angle of 40° at different depths. For each experiment, the left sub-figure displays the received rawdata as well as the region used to sum the intensities for the method of Papadacci (blue curve computed for point (x_d, z_d)) and for the DAS method applied for plane wave imaging (red curve computed for point (x_p, z_p)). The right sub-figure shows the distance error between the two curves expressed in terms of wavelength. The red dotted line represents the limit of $\lambda/8$.

Publications

Journal article

1. **M. Zhang**, F. Varray, A. Besson, R. E. Carrillo, M. Viallon, J-P Thiran, D. Friboulet, H. Liebgott, O. Bernard, "Extension of Fourier-based techniques for ultrafast imaging in ultrasound with diverging waves", *IEEE Transactions on Ultrasonics, Ferroelectrics, and Frequency Control*, accepted.

2. A. Besson, **M. Zhang**, F. Varray, H. Liebgott, D. Friboulet, Y.Wiaux, J.-P. Thiran, R. E. Carrillo, O. Bernard, "A sparse reconstruction framework for Fourier-based plane wave imaging", *IEEE Transactions on Ultrasonics, Ferroelectrics, and Frequency Control*, accepted.

International conference paper

1. **M. Zhang**, H. Liebgott, F. Varray, D. Friboulet, O. Bernard, "A Fourier-based formalism for 3D ultrafast imaging with diverging waves", *IEEE International Ultrasonics Symposium*, Tours, France, 2016.

2. **M. Zhang**, A. Besson, R. E. Carrillo, F. Varray, M. Viallon, H. Liebgott, J.-P. Thiran, D. Friboulet, and O. Bernard, "Extension of Ultrasound Fourier Slice Imaging Theory to Sectorial Acquisition", *IEEE International Ultrasonics Symposium*, Taipei, Taiwan, pp.1-4, 2015.

3. **M. Zhang**, H. Liebgott, F. Varray, D. Friboulet, and O. Bernard, "Speckle Decorrelation of Motion in Ultrasound Fourier Images", *IEEE International Ultrasonics Symposium*, Chicago, USA, pp. 1203-1206, 2014.

4. O. Bernard, **M. Zhang**, F. Varray, J.-P. Thiran, H. Liebgott, and D. Friboulet, "Ultrasound Fourier Slice Imaging: a Novel Approach for Ultrafast Imaging Technique", *IEEE International Ultrasonics Symposium*, Chicago, USA, pp. 129-132, 2014.

5. A. Besson, R. E. Carrillo, **M. Zhang**, D. Friboulet, O. Bernard, Y.Wiaux, J.-P. Thiran, "Sparse regularization methods in ultrafast ultrasound imaging". *IEEE 24th European Signal Processing Conference (EUSIPCO 2016)*, 2016.

6. R. E. Carrillo, A. Besson, **M. Zhang**, D. Friboulet, Y.Wiaux, J.-P. Thiran, O. Bernard, "A sparse regularization approach for ultrafast ultrasound imaging", *IEEE International Ultrasonics Symposium*, Taipei, Taiwan, pp1-4, 2015.

Miaomiao ZHANG

Bibliography

[Anavekar and Oh (2009)] Anavekar, N. S. and Oh, J. K. (2009). Doppler echocardiography: A contemporary review. *Journal of cardiology*, 54(3):347–358.

[Angelsen (2000)] Angelsen, B. A. (2000). Ultrasound imaging. *Waves, signals and signal processing*, 1.

[Bercoff *et al.* (2011)] Bercoff, J., Montaldo, G., Loupas, T., Savery, D., Mézière, F., Fink, M., and Tanter, M. (2011). Ultrafast compound doppler imaging: providing full blood flow characterization. *IEEE Transactions on Ultrasonics, Ferroelectrics, and Frequency Control*, 58(1):134–147.

[Bernard *et al.* (2014)] Bernard, O., Zhang, M., Varray, F., Gueth, P., Thiran, J., Liebgott, H., and Friboulet, D. (2014). Ultrasound fourier slice imaging: a novel approach for ultrafast imaging technique. In *IEEE International Ultrasonics Symposium (IUS)*, pages 129–132. IEEE.

[Brekke *et al.* (2007)] Brekke, S., Rabben, S. I., Støylen, A., Haugen, A., Haugen, G. U., Steen, E. N., and Torp, H. (2007). Volume stitching in three-dimensional echocardiography: distortion analysis and extension to real time. *Ultrasound in medicine & biology*, 33(5):782–796.

[CIR (2013)] (2013). *Computerized Imaging Reference Systems Inc. [Online]. Available: http://www.cirsinc.com/products/all/80/general-purpose-ultrasound-phantom/*.

[Carrillo *et al.* (2015)] Carrillo, R. E., Besson, A., Zhang, M., Friboulet, D., Wiaux, Y., Thiran, J.-P., and Bernard, O. (2015). A sparse regularization approach for ultrafast ultrasound imaging. In *Ultrasonics Symposium (IUS), 2015 IEEE International*, pages 1–4. Ieee.

[Cheng and Lu (2006)] Cheng, J. and Lu, J. (2006). Extended high-frame rate imaging method with limited-diffraction beams. *IEEE Transactions on Ultrasonics, Ferroelectrics, and Frequency Control*, 53(5):880–899.

[Cikes *et al.* (2014)] Cikes, M., Tong, L., Sutherland, G. R., and D'hooge, J. (2014). Ultrafast cardiac ultrasound imaging: Technical principles, applications, and clinical benefits. *JACC: Cardiovascular Imaging*, 7(8):812–823.

[Dekker *et al.* (1974)] Dekker, D. L., Piziali, R. L., and Dong, E. (1974). A system for ultrasonically imaging the human heart in three dimensions. *Computers and biomedical research*, 7(6):544–553.

[Demi *et al.* (2012)] Demi, L., Verweij, M. D., Koen, W., and Dongen, V. (2012). Parallel transmit beamforming using orthogonal frequency division multiplexing applied to harmonic imaging-a feasibility study. *IEEE transactions on ultrasonics, ferroelectrics, and frequency control*, 59(11).

[Demi *et al.* (2015)] Demi, L., Ramalli, A., Giannini, G., and Mischi, M. (2015). In vitro and in vivo tissue harmonic images obtained with parallel transmit beamforming by means of orthogonal frequency division multiplexing [correspondence]. *IEEE transactions on ultrasonics, ferroelectrics, and frequency control*, 62(1):230–235.

[Denarie *et al.* (2013)a] Denarie, B., Bjastad, T., and Torp, H. (2013a). Multi-line transmission in 3-d with reduced crosstalk artifacts: a proof of concept study. *IEEE transactions on ultrasonics, ferroelectrics, and frequency control*, 60(8):1708–1718.

[Denarie *et al.* (2013)b] Denarie, B., Tangen, T. A., Ekroll, I. K., Rolim, N., Torp, H., Bjastad, T., and Lovstakken, L. (2013b). Coherent plane wave compounding for very high frame rate ultrasonography of rapidly moving targets. *Medical Imaging, IEEE Transactions on*, 32(7):1265–1276.

[Drukarev *et al.* (1993)] Drukarev, A., Konstantinides, K., and Seroussi, G. (1993). Beam transformation techinques for ultrasonic medical imaging. *IEEE transactions on ultrasonics, ferroelectrics, and frequency control*, 40(6):717–726.

[Dubberstein and Von Ramm (2000)] Dubberstein, D. T. and Von Ramm, O. T. (2000). Methods and systems for ultrasound scanning using spatially and spectrally separated transmit ultrasound beams. US Patent 6,159,153.

[Ekroll *et al.* (2014)] Ekroll, I. K., Dahl, T., Torp, H., and LÃÿvstakken, L. (2014). Combined vector velocity and spectral doppler imaging for improved imaging of complex blood flow in the carotid arteries. *Ultrasound in Medicine & Biology*, 40(7):1629–1640.

[Ekroll *et al.* (2015)] Ekroll, I. K., Voormolen, M. M., Standal, O. K. V., Rau, J. M., and Lovstakken, L. (2015). Coherent compounding in doppler imaging. *IEEE Transactions on Ultrasonics, Ferroelectrics, and Frequency Control*, 62(9):1634–1643.

[Gammelmark and Jensen (2014)] Gammelmark, K. L. and Jensen, J. A. (2014). 2-d tissue motion compensation of synthetic transmit aperture images. *IEEE Transactions on Ultrasonics, Ferroelectrics, and Frequency Control*, 61(4):594–610.

[Garcia *et al.* (2013)] Garcia, D., Tarnec, L., Muth, S., Montagnon, E., PorÃľe, J., and Cloutier, G. (2013). Stolt's f-k migration for plane wave ultrasound imaging. *IEEE Transactions on Ultrasonics, Ferroelectrics and Frequency Control*, 60(9):1853–1867.

[Gazdag and Sguazzero (1984)] Gazdag, I. and Sguazzero, P. (1984). Migration of seismic data. *Proceedings of the IEEE*, 72(10):1302–1315.

[Gennisson *et al.* (2010)] Gennisson, J., Deffieux, T., Macé, E., Montaldo, G., Fink, M., and Tanter, M. (2010). Viscoelastic and anisotropic mechanical properties of in vivo muscle tissue assessed by supersonic shear imaging. *Ultrasound in medicine & biology*, 36(5):789–801.

[Hasegawa and Kanai (2011)] Hasegawa, H. and Kanai, H. (2011). High-frame-rate echocardiography using diverging transmit beams and parallel receive beamforming. *Journal of Medical Ultrasonics*, 38(3):129–140.

[Hergum *et al.* (2007)] Hergum, T., Bjastad, T., Kristoffersen, K., and Torp, H. (2007). Parallel beamforming using synthetic transmit beams. *IEEE transactions on ultrasonics, ferroelectrics, and frequency control*, 54(2):271–280.

[Hsieh and (Society) (2009)] Hsieh, J. and (Society), S. (2009). *Computed tomography: principles, design, artifacts, and recent advances.* Bellingham, Wash. SPIE Hoboken, N. J. John Wiley & Sons.

[Hung *et al.* (2007)] Hung, J., Lang, R., Flachskampf, F., Shernan, S. K., McCulloch, M. L., Adams, D. B., Thomas, J., Vannan, M., and Ryan, T. (2007). 3d echocardiography: a review of the current status and future directions. *Journal of the American Society of Echocardiography*, 20(3):213–233.

[Insana and Brown (1993)] Insana, M. F. and Brown, D. G. (1993). Acoustic scattering theory applied to soft biological tissues. *Ultrasonic scattering in biological tissues*, pages 75–124.

[Jackson *et al.* (1991)] Jackson, J. I., Meyer, C. H., Nishimura, D. G., and Macovski, A. (1991). Selection of a convolution function for fourier inversion using gridding [computerised tomography application]. *IEEE transactions on medical imaging*, 10(3):473–478.

[Jensen (1996)] Jensen, J. A. (1996). Field: A program for simulating ultrasound systems. In *10TH NORDICBALTIC CONFERENCE ON BIOMEDICAL IMAGING, VOL. 4, SUPPLEMENT 1, PART 1: 351–353*. Citeseer.

[Jensen *et al.* (2006)a] Jensen, J., Nikolov, S., Gammelmark, K., and Pedersen, M. (2006a). Synthetic aperture ultrasound imaging. *Ultrasonics*, 44:e5–e15.

[Jensen *et al.* (2006)b] Jensen, J. A., Nikolov, S. I., Gammelmark, K. L., and Pedersen, M. H. (2006b). Synthetic aperture ultrasound imaging. *Ultrasonics*, 44:e5–e15.

[Jensen and Svendsen (1992)] Jensen, J. and Svendsen, N. (1992). Calculation of pressure fields from arbitrarily shaped, apodized, and excited ultrasound transducers. *IEEE Transactions on Ultrasonics, Ferroelectrics, and Frequency Control*, 39(2):262–267.

[Kim *et al.* (2002)] Kim, K., Hwang, J., Jeong, J., and Song, T. (2002). An efficient motion estimation and compensation method for ultrasound synthetic aperture imaging. *Ultrasonic imaging*, 24(2):81–99.

[Kruizinga *et al.* (2012)] Kruizinga, P., Mastik, F., de Jong, N., van der Steen, A., and van Soest, G. (2012). Plane-wave ultrasound beamforming using a nonuniform fast fourier transform. *IEEE Transactions on Ultrasonics, Ferroelectrics, and Frequency Control*, 59(12):2684–2691.

[Lang *et al.* (2006)] Lang, R. M., Mor-Avi, V., Sugeng, L., Nieman, P. S., and Sahn, D. J. (2006). Three-dimensional echocardiography: the benefits of the additional dimension. *Journal of the American College of Cardiology*, 48(10):2053–2069.

[Lenge *et al.* (2014)] Lenge, M., Ramalli, A., Boni, E., Liebgott, H., Cachard, C., and Tortoli, P. (2014). High-frame-rate 2-d vector blood flow imaging in the frequency domain. *IEEE Transactions on Ultrasonics, Ferroelectrics, and Frequency Control*, 61(9):1504–1514.

[Lu (1997)] Lu, J. (1997). 2d and 3d high frame rate imaging with limited diffraction beams. *IEEE Transactions on Ultrasonics, Ferroelectrics and Frequency Control*, 44(4):839–856.

[Lu (1998)] Lu, J. (1998). Experimental study of high frame rate imaging with limited diffraction beams. *IEEE Transactions on Ultrasonics, Ferroelectrics, and Frequency Control*, 45(1):84–97.

[Mallart and Fink (1992)] Mallart, R. and Fink, M. (1992). Improved imaging rate through simultaneous transmission of several ultrasound beams. In *San Diego'92*, pages 120–130. International Society for Optics and Photonics.

[Monaghan (2006)] Monaghan, M. J. (2006). Role of real time 3d echocardiography in evaluating the left ventricle. *Heart*, 92(1):131–136.

[Montaldo *et al.* (2009)] Montaldo, G., Tanter, M., Bercoff, J., Benech, N., and Fink, M. (2009). Coherent plane-wave compounding for very high frame rate ultrasonography and transient elastography. *IEEE Transactions on Ultrasonics, Ferroelectrics and Frequency Control*, 56(3):489–506.

[Mor-Avi and Lang (2010)] Mor-Avi, V. and Lang, R. M. (2010). The evolution of three-dimensional echocardiography: How did it happen. In *Textbook of Real-Time Three Dimensional Echocardiography*, pages 1–8. Springer.

[Muller *et al.* (2015)] Muller, M., Ait-Belkacem, D., Hessabi, M., Gennisson, J. L., GrangÃ©, G., Goffinet, F., Lecarpentier, E., Cabrol, D., Tanter, M., and Tsatsaris, V. (2015). Assessment of the cervix in pregnant women using shear wave elastography: A feasibility study. *Ultrasound in Medicine and Biology*, 41(11):2789–2797.

[Ng and Swanevelder (2011)] Ng, A. and Swanevelder, J. (2011). Resolution in ultrasound imaging. *Continuing Education in Anaesthesia, Critical Care & Pain*, 11(5):186–192.

[O'sullivan (1985)] O'sullivan, J. (1985). A fast sinc function gridding algorithm for fourier inversion in computer tomography. *IEEE Transactions on Medical Imaging*, 4(4):200–207.

[Oddershede and Jensen (2007)] Oddershede, N. and Jensen, J. A. (2007). Effects influencing focusing in synthetic aperture vector flow imaging. *IEEE transactions on ultrasonics, ferroelectrics, and frequency control*, 54(9):1811–1825.

[Papadacci *et al.* (2014)] Papadacci, C., Pernot, M., Couade, M., Fink, M., and Tanter, M. (2014). High-contrast ultrafast imaging of the heart. *IEEE Transactions on Ultrasonics, Ferroelectrics and Frequency Control*, 61(2):288–301.

[Pavy (1993)] Pavy, H. G. (1993). *Real-time ultrasonic volumetric imaging with stereoscopic display.*

[Perrin *et al.* (2012)a] Perrin, D., Vasilyev, N., Marx, G., and Pedro, J. (2012a). Temporal enhancement of 3d echocardiography by frame reordering. *JACC: Cardiovascular Imaging*, 5(3):300–304.

[Perrin *et al.* (2012)b] Perrin, D. P., Vasilyev, N. V., Marx, G. R., and Pedro, J. (2012b). Temporal enhancement of 3d echocardiography by frame reordering. *JACC: Cardiovascular Imaging*, 5(3):300–304.

[Poree *et al.* (2016)] Poree, J., Posada, D., Hodzic, A., Tournoux, F., Cloutier, G., and Garcia, D. (2016). High-frame-rate echocardiography using coherent compounding with doppler-based motion-compensation.

[Prieur *et al.* (2013)] Prieur, F., Dénarié, B., Austeng, A., and Torp, H. (2013). Correspondence-multi-line transmission in medical imaging using the second-harmonic signal. *IEEE transactions on ultrasonics, ferroelectrics, and frequency control*, 60(12):2682–2692.

[Provost *et al.* (2011)] Provost, J., Nguyen, V., Legrand, D., Okrasinski, S., Costet, A., Gambhir, A., Garan, H., and Konofagou, E. (2011). Electromechanical wave imaging for arrhythmias. *Physics in medicine and biology*, 56(22):L1.

[Provost *et al.* (2014)] Provost, J., Papadacci, C., Arango, J. E., Imbault, M., Fink, M., Gennisson, J.-L., Tanter, M., and Pernot, M. (2014). 3d ultrafast ultrasound imaging in vivo. *Physics in medicine and biology*, 59(19):L1.

[Provost *et al.* (2015)] Provost, J., Papadacci, C., Demene, C., Gennisson, J. L., Tanter, M., and Pernot, M. (2015). 3-d ultrafast doppler imaging applied to the noninvasive mapping of blood vessels in vivo. *IEEE Transactions on Ultrasonics, Ferroelectrics, and Frequency Control*, 62:1467–1472.

[Rabben (2010)] Rabben, S. I. (2010). Technical principles of transthoracic three-dimensional echocardiography. In *Textbook of Real-Time Three Dimensional Echocardiography*, pages 9–24. Springer.

[Ricci *et al.* (2014)] Ricci, S., Bassi, L., and Tortoli, P. (2014). Real-time vector velocity assessment through multigate doppler and plane waves. *IEEE Transactions on Ultrasonics, Ferroelectrics, and Frequency Control*, 61(2):314–324.

[Roux *et al.* (2015)a] Roux, E., Ramalli, A., Robini, M., Liebgott, H., Cachard, C., and Tortoli, P. (2015a). Spiral array inspired multi-depth cost function for 2d sparse array optimization. In *Ultrasonics Symposium (IUS), 2015 IEEE International*, pages 1–4. IEEE.

[Roux *et al.* (2015)b] Roux, E., Ramalli, A., Tortoli, P., Cachard, C., Robini, M., and Liebgott, H. (2015b). Speed-up of acoustic simulation techniques for 2d sparse array optimization by simulated annealing. In *Ultrasonics Symposium (IUS), 2015 IEEE International*, pages 1–4. IEEE.

[Salles *et al.* (2015)] Salles, S., Chee, A., Garcia, D., Yu, A., Vray, D., and Liebgott, H. (2015). 2-d arterial wall motion imaging using ultrafast ultrasound and transverse oscillations. *IEEE Transactions on Ultrasonics, Ferroelectrics, and Frequency Control*, 62(6):1047–1058.

[Schmerr Jr (2014)] Schmerr Jr, L. W. (2014). *Fundamentals of ultrasonic phased arrays*, volume 215. Springer.

[Shattuck *et al.* (1984)] Shattuck, D. P., Weinshenker, M. D., Smith, S. W., and von Ramm, O. T. (1984). Explososcan: A parallel processing technique for high speed ultrasound imaging with linear phased arrays. *The Journal of the Acoustical Society of America*, 75(4):1273–1282.

[Shiota (2014)] Shiota, T. (2014). Role of modern 3d echocardiography in valvular heart disease. *The Korean journal of internal medicine*, 29(6):685.

[Shirasaka (1989)] Shirasaka, T. (1989). Ultrasonic imaging apparatus. US Patent 4,815,043.

[Skaug *et al.* (2014)] Skaug, T. R., Amundsen, B. H., Hergum, T., Urheim, S., Torp, H., and Haugen, B. O. (2014). Quantification of aortic regurgitation using high-pulse repetition frequency three-dimensional colour doppler. *European Heart Journal-Cardiovascular Imaging*, 15(6):615–622.

[Stark *et al.* (1981)] Stark, H., Woods, J. W., Paul, I., and Hingorani, R. (1981). An investigation of computerized tomography by direct fourier inversion and optimum interpolation. *IEEE Transactions on Biomedical Engineering*, (7):496–505.

[Tanter and Fink (2014)] Tanter, M. and Fink, M. (2014). Ultrafast imaging in biomedical ultrasound. *IEEE Transactions on Ultrasonics, Ferroelectrics, and Frequency Control*, 61(1):102–119.

[Tiran *et al.* (2015)] Tiran, E., Deffieux, T., Correia, M., Maresca, D., Osmanski, B.-F., Sieu, L.-A., Bergel, A., Cohen, I., Pernot, M., and Tanter, M. (2015). Multiplane wave imaging increases signal-to-noise ratio in ultrafast ultrasound imaging. *Physics in medicine and biology*, 60(21):8549.

[Tong *et al.* (2013)a] Tong, L., Gao, H., and D'hooge, J. (2013a). Multi-transmit beam forming for fast cardiac imaging: a simulation study. *IEEE transactions on ultrasonics, ferroelectrics, and frequency control*, 60(8):1719–1731.

[Tong *et al.* (2013)b] Tong, L., Ortega, A., Gao, H., and D'hooge, J. (2013b). Fast three-dimensional ultrasound cardiac imaging using multi-transmit beam forming: A simulation study. In *2013 IEEE International Ultrasonics Symposium (IUS)*, pages 1456–1459. IEEE.

[Tong *et al.* (2014)] Tong, L., Ramalli, A., Jasaityte, R., Tortoli, P., and D'hooge, J. (2014). Multi-transmit beam forming for fast cardiac imaging: Experimental validation and in vivo application. *IEEE transactions on medical imaging*, 33(6):1205–1219.

[Trahey and Nock (1992)] Trahey, G. E. and Nock, L. F. (1992). Synthetic receive aperture imaging with phase correction for motion and for tissue inhomogeneities. ii. effects of and correction for motion. *IEEE transactions on ultrasonics, ferroelectrics, and frequency control*, 39(4):496–501.

[Udesen *et al.* (2008)] Udesen, J., Gran, F., Hansen, K. L., Jensen, J. A., Thomsen, C., and Nielsen, M. B. (2008). High frame-rate blood vector velocity imaging using plane waves: simulations and preliminary experiment. *IEEE Transactions on Ultrasonics, Ferroelectrics, and Frequency Control*, 55(8):1729–1743.

[Von Ramm *et al.* (1991)] Von Ramm, O. T., Smith, S. W., and Pavy, H. G. (1991). High-speed ultrasound volumetric imaging system. ii. parallel processing and image display. *IEEE transactions on ultrasonics, ferroelectrics, and frequency control*, 38(2):109–115.

[Wang and Lu (2007)] Wang, J. and Lu, J.-y. (2007). Motion artifacts of extended high frame rate imaging. *Ultrasonics, Ferroelectrics, and Frequency Control, IEEE Transactions on*, 54(7):1303–1315.

[Wijk and Thijssen (2002)] Wijk, M. V. and Thijssen, J. (2002). Performance testing of medical ultrasound equipment: Fundamental vs. harmonic mode. *Ultrasonics*, 40:585âĂŞ–591.

[Yiu *et al.* (2008)] Yiu, B. Y., Tsang, I. K., and Alfred, C. (2008). A modified synthetic aperture imaging approach with axial motion compensation. In *2008 IEEE Ultrasonics Symposium*, pages 1254–1257. IEEE.

[Zhang *et al.*] Zhang, M., Varray, F., Besson, A., Carrillo, R. E., Viallon, M., Garcia, D., Thiran, J.-P., Friboulet, D., Liebgott, H., and Bernard, O. Extension of fourier-based techniques for ultrafast imaging in ultrasound with diverging waves. *IEEE Transactions on Ultrasonics, Ferroelectrics, and Frequency Control*.

[Zhang *et al.* (2015)] Zhang, M., Besson, A., Carrillo, R. E., Varray, F., Liebgott, H., Thiran, J., Friboulet, D., and Bernard, O. (2015). Extension of ultrasound fourier slice imaging theory to sectorial acquisition. In *IEEE International Ultrasonics Symposium (IUS)*.

[Zhang *et al.* (2016)] Zhang, M., Liebgott, H., Varray, F., Friboulet, D., and Bernard, O. (2016). A fourier-based formalism for 3d ultrafast imaging with diverging waves. In *IEEE International Ultrasonics Symposium (IUS)*.

[von Ramm *et al.* (1984)] von Ramm, O., Weinshenker, M., and Snyder, J. (1984). High speed echocardiography. In *Proceedings of the 5th Congress of the European Federation of Societies for Ultrasound in Medicine*, volume 5, page 41.

FOLIO ADMINISTRATIF

THESE DE L'UNIVERSITE DE LYON OPEREE AU SEIN DE L'INSA LYON

NOM : ZHANG
DATE de SOUTENANCE : 16/12/2016

Prénoms : Miaomiao

TITRE : Fourier-based reconstruction of ultrafast sectorial images in ultrasound

NATURE : Doctorat
Numéro d'ordre :

Ecole doctorale : ELECTRONIQUE, ELECTROTECHNIQUE, AUTOMATIQUE

Spécialité : Traitement du Signal et de l'Image

RESUME : Echocardiography is one of the most widely used modality in real time heart imaging thanks to its noninvasive nature and low cost. By providing dense image volumes in real time, three-dimensional echocardiography can improve the accuracy of the echocardiographic evaluation of cardiac chamber volumes and be used to assess cardiovascular function and anatomy in various clinical settings. However, the real-time property of three-dimensional echocardiography is still limited in terms of frame rate due to the limited speed of sound. To increase the frame rate, plane wave and diverging wave in transmission have been proposed to drastically reduce the number of transmissions to reconstruct one image. In this thesis, starting with the 2D plane wave imaging methods, the reconstruction of 2D/3D echocardiographic sequences in Fourier domain using diverging waves is addressed. The main contributions are described below.

The first contribution of this thesis is to study the influence of the transmission scheme in the context of 2D plane wave imaging. Based on an analytical study, the influence of the transmitted angle sequences and the number of plane waves on the compounded image quality is investigated. A dichotomous transmission scheme is proposed. The efficiency of the different transmission schemes is assessed by evaluating the quality of images reconstructed from the current state-of-the-art plane wave imaging methods. Numerical and experimental results show that the proposed transmission scheme significantly improves the quality of the reconstructed B-mode images at a constant frame rate.

The second contribution concerns the development of an alternative Fourier-based plane wave imaging method (i.e. Ultrasound Fourier Slice Beamforming) by using the concept of steered plane waves both in transmission and in reception. We build a theoretical model to describe the relationship between the echoes and object function based on the Fourier slice theorem. The proposed method is assessed using numerical simulations and experiments, including *in vitro* and *in vivo* experiments. Results revealed that the proposed method produces very competitive image quality compared to the state-of-the-art Fourier-based and spatial-based methods.

The third contribution concerns the extension of Fourier-based imaging methods from linear to sectorial imaging in 2D by studying the difference between plane wave and diverging wave transmission in terms of travel time for a given scatterer in the medium and a given transducer element. We derive an explicit spatial transformation which allows deforming the referential Cartesian space insonified by a diverging wave into a dedicated one where the modified medium can be considered as being excited by a plane wave. The performance of the derived approach is evaluated in terms of resolution and contrast from both simulations and *in vitro* experiments. Comparisons with the current state-of-the-art method illustrate the potential of the derived methods in producing competitive results with lower computational complexity when compared to the conventional delay and sum (DAS) technique.

Finally, the 2D Fourier-based diverging wave imaging methods are extended to 3D by deriving the equivalence between 3D diverging wave and plane wave. Numerical simulations are performed to validate and evaluate the proposed method. Results show that the proposed approach provides competitive scores in terms of image quality compared to the DAS technique, but with a much lower computational complexity.

MOTS-CLÉS : Ultrafast ultrasound imaging, Fourier-based methods, diverging wave

Laboratoire (s) de recherche : Centre de Recherche en Acquisition et Traitement de l'Image pour la Santé (CREATIS), UMR 5220, U1206, INSA-Lyon.

Directeur de thèse: FRIBOULET Denis, Professeur des Universités
BERNARD Olivier, Maître de Conférences

Président de jury : D'HOOGE Jan

Composition du jury : LOVSTAKKEN Lasse (Rapporteur), PERNOT Mathieu (Rapporteur), D'HOOGE Jan (Examinateur), BRIDAL S.Lori (Examinatrice), FRIBOULET Denis (Directeur de thèse), BERNARD Olivier (Co-directeur de thèse).